Faculty of Mathematics and Physics
Charles University, Prague

# A Measurement of the Dijet Cross Section in Two-Photon Collisions with the DELPHI Detector at LEP2

Doctoral Thesis
2003

Jiří Mašík

Prohlašuji, že jsem dizertační práci vypracoval samostatně s použitím uvedené literatury. Souhlasím se zapůjčením dizertační práce.

V Praze, 10. 7. 2003

# A Measurement of the Dijet Cross Section in Two-Photon Collisions with the DELPHI Detector at LEP2

Jiří Mašík

Institute of Physics,
Academy of Sciences of the Czech Republic

Supervisor: Professor Jiří Chýla

## Abstract

The measurement of inclusive cross sections of dijet production in the collisions of two quasireal photons obtained with the DELPHI detector at LEP2 is presented. Data on $d\sigma^{2j}/d\eta$, $d\sigma^{2j}/dE_T$, $d\sigma^{2j}/dx$ and jet profiles for jets with $E_T > 5$ GeV are compared to PYTHIA and HERWIG Monte Carlo event generators. Special attention is paid to the effects of soft particles coming from photon remnants.

# Acknowledgement

First of all I would like to thank Jiří Chýla, my supervisor, for guiding me through the course of my PhD thesis. It was a great education and I really appreciate countless discussions we had, his assistance and devotion to the subject of two-photon physics.

I would like to thank Jan Řídký for his comments on the manuscript and his continuous support. I am very grateful to Rupert Leitner and Václav Vrba who brought me to DELPHI and taught me a lot. I wish to thank my colleagues from Prague, in particular Tomáš Davídek and Jiří Rameš, for their help.

This thesis would have never happened without the impressive work of the DELPHI collaboration and of the accelerator staff who made the running of the experiment successful. I would like to thank the colleagues from the DELPHI $\gamma\gamma$ team, Frederic Kapusta, Valeri Pozdniakov, Wilfrid Da Silva, Igor Tiapkin, Šárka Todorova, Nikolai Zimin, for their help, discussions and comments on my work.

I received excellent support from the ROOT team and also from the open-source community around the world for computing related problems.

This work has been supported in part by the project LN00A006 of the Ministry of Education of the Czech Republic and by grant 202/99/1362 of the Grant Agency of the Czech Republic.

I wish to thank my family and friends.

*Dedicated to my parents.*

# Contents

# Chapter 1

# Introduction

The photon is a gauge boson of the electromagnetic interaction. It is considered to be a fundamental object without the inner structure. It has a point-like coupling to charged leptons and its interaction is described with a great precision by the quantum electrodynamics.

Photon interaction gets complicated due to the fact that the photon fluctuates into $q\overline{q}$ pair which can further interact strongly. If the characteristic time of the fluctuation is much larger than the interaction time the photon behaves approximately as a beam of almost collinear and mutually noninteracting partons. Such interaction of photon is called resolved interaction but for simplicity we sometimes speak of a resolved photon.

The abstraction from the genesis of the photon fluctuation brings the term photon structure into the description of the photon interactions. Parton distribution functions (PDF) of the photon are introduced to describe its hard collisions. The structure of the photon is referred to in the sense of dynamic behaviour in these collisions rather than in the sense of photon constituents.

Parton distribution functions of the photon can be investigated in several types of experiments. Photon structure is studied in deep inelastic e$\gamma$ scattering realized in $e^+e^-$ collisions. Independent measurements come from large-$p_T$ jet production analysis in $\gamma\gamma$ and $\gamma$p scattering. Information on the PDF is also extracted from the heavy-quark production in $\gamma p$ and $\gamma\gamma$ collisions. Our knowledge about the structure of the photon comes from experiments at PETRA and HERA colliders at DESY, TRISTAN at KEK, PEP at SLAC and LEP at CERN.

The subject of this thesis is a study of two-photon processes leading to large-$p_T$ jet production. The advantage of this process over the deep inelastic scattering on the photon comes from the fact that the dijet production is sensitive to the gluon content of the photon. The differential cross sections for the dijet production in collisions of quasi-real photons were measured and analysed using the DELPHI detector at LEP. The properties of the jets in two-photon collisions were studied and their shapes and profiles were investigated as well. Preliminary results of this thesis were reported at the conference Photon 2001 [1].

The thesis is organised as follows. The next chapter is devoted to theoretical aspects of

$\gamma\gamma$ collisions at $e^+e^-$ collider and dijet production in these collisions. An overview of the available experimental results on photon structure is presented in Chapter 3. The description of the DELPHI detector is given in Chapter 4. Monte Carlo event generators and simulation technique are discussed in Chapter 5. The analysis is described in Chapter 6. The main results on the differential cross sections and jet profiles can be found in Chapter 7. The discussion of results is given in Chapter 8. Technical details of the unfolding procedure are addressed in Appendix B.

The system of units $\hbar = c = 1$ is used throughout this text.

# Chapter 2

# Description of $\gamma\gamma$ collisions

In this chapter the elements of the theory of $\gamma\gamma$ collisions at $e^+e^-$ collider are reviewed. The formalism of photon structure functions and parton distribution functions of the photon is presented.

At present the interactions of the photon are studied at $e^+e^-$ and $e^\pm$ p colliders where lepton beams are intense sources of virtual[1] photons. The spectrum of these photons is described by the Equivalent Photon Approximation (EPA) [2]

$$f_{\gamma/e}(z, Q^2) = \frac{\alpha}{2\pi Q^2}\left[\frac{1+(1-z)^2}{z} - \frac{2m_e^2 z}{Q^2}\right] \tag{2.1}$$

where $z$ denotes the fraction of the electron energy carried by the photon and $Q^2$ stands for the photon virtuality.

The integrated form of the photon flux known as Weizsäcker-Williams formula [3, 4] gives the number of virtual photons in some interval of virtualities $(P^2_{min}, P^2_{max})$.

$$f_{\gamma/e}(z, P^2_{min}, P^2_{max}) = \frac{\alpha}{2\pi}\left[\frac{1+(1-z)^2}{z}\ln\frac{P^2_{max}}{P^2_{min}} - 2m_e^2 z(\frac{1}{P^2_{min}} - \frac{1}{P^2_{max}})\right] \tag{2.2}$$

The minimum photon virtuality $P^2_{min}$ is given by $P^2_{min} = m_e^2 z^2/(1-z)$ while the maximum virtuality $P^2_{max} = (1-z)E^2\theta^2_{max}$ is limited by the maximum polar angle $\theta_{max}$ at which electrons are allowed to scatter[2] and the electron beam energy $E$.

The photons frequently interact with each other and these collisions were a dominant process at LEP2 as illustrated by Fig. 2.1 where total $\gamma\gamma$ cross section is compared with other processes. The interaction can be schematically written

[1] Flux of real photons might become available at a future linear $e^+e^-$ collider where a beam of real photons could be prepared by Compton backscattering of laser photons.

[2] For experiments where scattered electrons may escape the detector near the beam pipe the angle $\theta_{max}$ corresponds to the the lower acceptance of electron detectors in polar angle. This yields upper limit on virtuality of photons in so-called anti-tagged photon collisions.

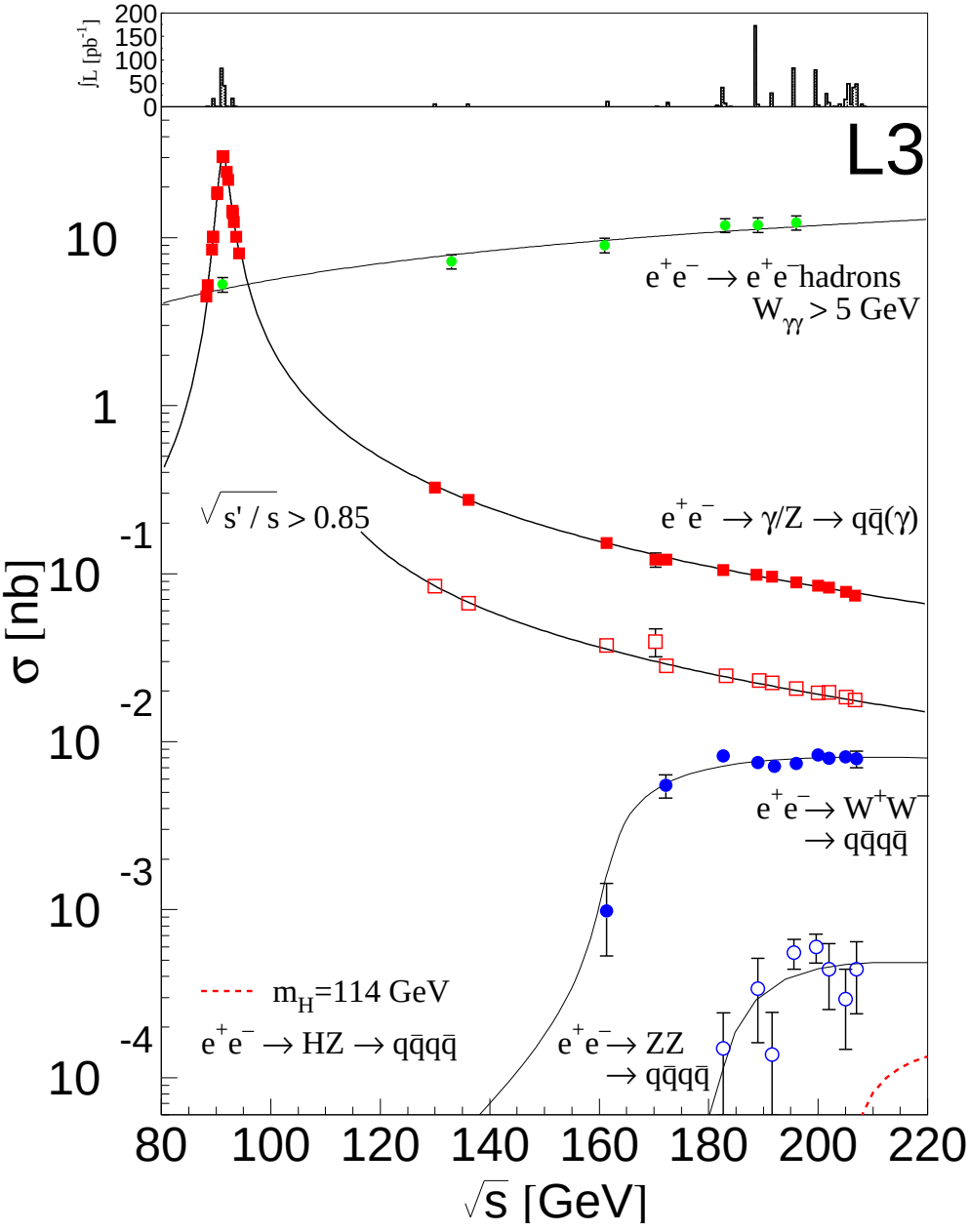


Figure 2.1: Comparison of the cross section for two-photon collisions with other process in the LEP energy range. Cross sections of hadronic final-state channels as a function of $\sqrt{s_{ee}}$ is shown for two-photon interactions with small final-state mass, s-channel $\gamma$/Z interaction, $W^+W^-$ pair production, ZZ production and Higgs production hypothesis ($m_H = 114$ GeV). Taken from M. Kienzle-Focacci's talk at LEP Fest 2000.

$$\mathrm{e^+e^-} \to \mathrm{e^+e^-}\gamma^*\gamma^* \to \mathrm{e^+e^-X} \tag{2.3}$$

and is depicted in Fig. 2.2 where kinematical variables are introduced. X denotes final state of $\gamma\gamma$ collision with an invariant mass $W$ given by $W^2 = (p+q)^2$. Electron and positron radiate photons with virtualities $P^2$ and $Q^2$ given by the difference of lepton four-momenta $p = k - k'$ and $q = l - l'$ respectively.

$$P^2 = -p^2 = -(k-k')^2 > 0 \tag{2.4a}$$
$$Q^2 = -q^2 = -(l-l')^2 > 0 \tag{2.4b}$$

Final state electron and positron are typically scattered by a small angle and escape undetected along the beam pipe. In this case both virtualities $P^2 \sim 0$ and $Q^2 \sim 0$ are small and scattering of two quasi-real photons takes place. When one of the virtualities becomes large, a quasi-real photon is probed by a virtual photon. Such process will be denoted as $\gamma^*\gamma$ scattering. It is the kinematical range of the deep inelastic scattering (DIS). The virtualities of incoming photons are reflected in the experimental signature of the events which are classified as untagged, single-tagged or double-tagged.

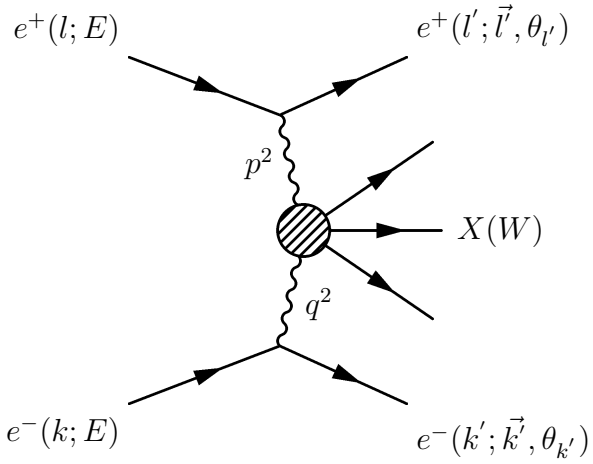


Figure 2.2: Kinematics of two-photon collision.

The basic quantity describing the structure of the photon are quark, antiquark and gluon distribution functions $q_i(x,M), \overline{q}_i(x,M)$ and $g(x,M)$ which depend beside the momentum fraction $x$ also on the factorisation scale $M$. The main difference between hard collisions of hadrons and photons concerns the fact that quark and gluon distribution functions of the photon

$$\Sigma(x,M) \equiv \sum_{i=1}^{n_f} \left(q_i(x,M) + \overline{q}_i(x,M)\right), \tag{2.5}$$

$$q_{\mathrm{NS}}(x,M) \equiv \sum_{i=1}^{n_f} \left(e_i^2 - \langle e^2\rangle\right)\left(q_i(x,M) + \overline{q}_i(x,M)\right) \tag{2.6}$$

satisfy by the system of coupled inhomogeneous evolution equations

$$\frac{\mathrm{d}\Sigma(M)}{\mathrm{d}\ln M^2} = \delta_\Sigma k_q(M) + P_{qq}(M)\otimes\Sigma(M) + P_{qg}(M)\otimes g(M), \quad (2.7)$$

$$\frac{\mathrm{d}g(M)}{\mathrm{d}\ln M^2} = k_g(M) + P_{gq}(M)\otimes\Sigma(M) + P_{gg}(M)\otimes g(M), \quad (2.8)$$

$$\frac{\mathrm{d}q_{\mathrm{NS}}(M)}{\mathrm{d}\ln M^2} = \delta_{\mathrm{NS}} k_q(M) + P_{\mathrm{NS}}(M)\otimes q_{\mathrm{NS}}(M), \quad (2.9)$$

where $\delta_{\mathrm{NS}} \equiv 6n_f\left(\langle e^4\rangle - \langle e^2\rangle^2\right)$ and $\delta_\Sigma = 6n_f\langle e^2\rangle$. The splitting functions admit expansion in powers of $\alpha_s(M)$

$$k_q(x,M) = \frac{\alpha}{2\pi}\left[k_q^{(0)}(x) + \frac{\alpha_s(M)}{2\pi}k_q^{(1)}(x) + \left(\frac{\alpha_s(M)}{2\pi}\right)^2 k_q^{(2)}(x) + \cdots\right], \quad (2.10)$$

$$k_g(x,M) = \frac{\alpha}{2\pi}\left[\frac{\alpha_s(M)}{2\pi}k_g^{(1)}(x) + \left(\frac{\alpha_s(M)}{2\pi}\right)^2 k_g^{(2)}(x) + \cdots\right], \quad (2.11)$$

$$P_{ij}(x,M) = \frac{\alpha_s(M)}{2\pi}P_{ij}^{(0)}(x) + \left(\frac{\alpha_s(M)}{2\pi}\right)^2 P_{ij}^{(1)}(x) + \cdots. \quad (2.12)$$

where the lowest order inhomogeneous splitting function $k_q^{(0)}(x) = (x^2 + (1-x)^2)$ as well as the homogeneous splitting functions $P_{ij}^{(0)}(x)$ are *unique*, whereas all higher order splitting functions $k_q^{(j)}, k_g^{(j)}, P_{kl}^{(j)}, j \geq 1$ depend on the choice of the factorisation scheme (FS). The equations (2.7-2.9) can be recast into evolution equations for $q_i(x,M), \overline{q}_i(x,M)$ and $g(x,M)$ with inhomogeneous splitting functions $k_{q_i}^{(0)} = 3e_i^2 k_q^{(0)}$.

The presence of the inhomogeneous terms on the r.h.s. of (2.7-2.9) implies that their general solutions can be written as a sum of a particular solution of the full inhomogeneous equations and a general solution of the corresponding homogeneous ones, called *hadron-like* (or VMD) part. A subset of the former resulting from the resummation of contributions of multiple parton emissions off the primary QED vertex $\gamma \to q\overline{q}$ and vanishing at $M = M_0$, are called *point-like* (or anomalous) solutions. The separation of PDF of the photon into their point-like and hadron-like parts is thus inherently ambiguous. For instance, the two widely used sets of PDF of the photon, SaS 1D and SaS 2D (see 2.1) differ primarily by the choice of $M_0$: $M_0 = 0.6$ GeV for SaS 1D, whereas $M_0 = 2$ GeV for SaS 2D. As a result, SaS 2D has much bigger hadron-like part than SaS 1D.

In the case of a hard collision of two quasi-real photons the blob in Fig. 2.2 can be calculated in perturbative QCD. Hard collisions of two photons in $e^+e^-$ collisions have in general three classes of contributions: direct, single-resolved and double-resolved. Examples of relevant diagrams are depicted in Fig. 2.3. The direct process (Fig. 2.3a) is an interaction in which two photons couple directly to $q\overline{q}$ pair with large-$p_T$ or a heavy $Q\overline{Q}$ pair. In the single-resolved process (Fig. 2.3b) the large-$p_T$ pair of partons comes from the collision of one

of the photons with a parton from the other one. The double-resolved process (Fig. 2.3c) is an interaction of partons from both photons. In the leading order of QCD the direct interaction leads just to two jets in the final state. In the single-resolved and double-resolved contributions one or two additional spectator jets may be seen. Their origin is in the remnant of the photon.

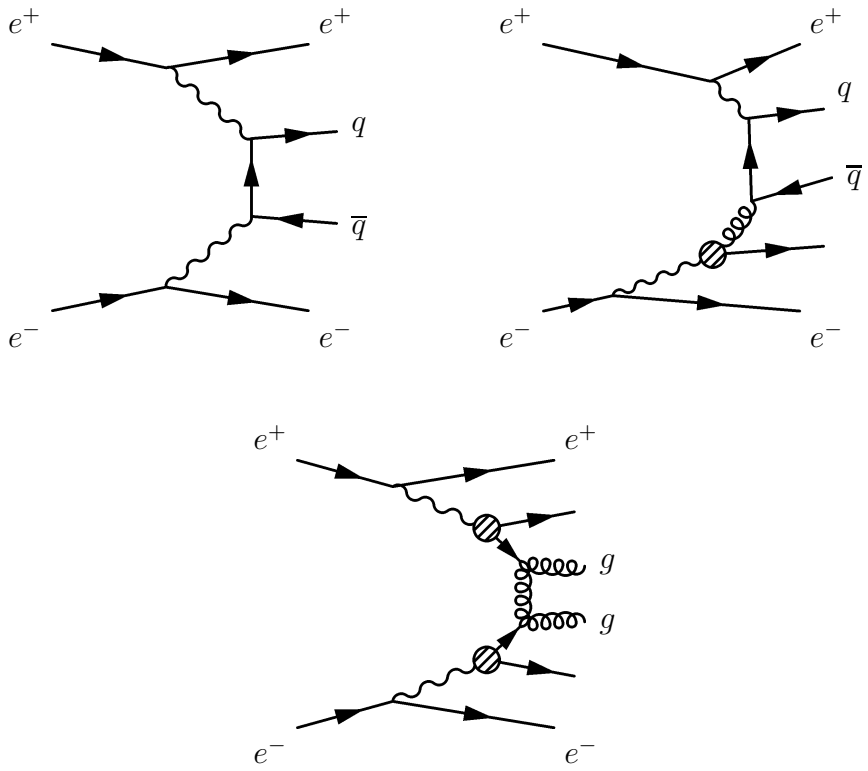


Figure 2.3: Direct process (a) and examples of single-resolved (b) and double-resolved (c) processes. Blobs denote PDF of the resolved photon.

In leading order (LO) QCD the cross section for dijet production in double-resolved $\gamma\gamma$ interaction can be written as

$$\frac{d\sigma}{dy_1 dy_2 dx_1 dx_2 d\cos\theta^\star dQ^2 dP^2} \propto \frac{1}{s}\frac{f_{\gamma/e}(y_1,Q^2)}{y_1}\frac{f_{\gamma/e}(y_2,P^2)}{y_2} \times \sum_{i,j}\frac{f_{i/\gamma}(x_1,{p_T}^2,Q^2)}{x_1}\frac{f_{j/\gamma}(x_2,{p_T}^2,P^2)}{x_2}|M_{ij}(\cos\theta^\star)|^2 \tag{2.13}$$

where $f_{\gamma/e}(y,Q^2)$ is given by (2.1), $s$ is the $e^+e^-$ CMS[3] energy squared and $M_{ij}(\cos\theta^\star)$

[3]centre-of-mass

denotes the matrix element[4] for the two-parton scattering depending on the angle $\theta^\star$ between incoming and outgoing partons in the centre-of-mass system of the parton subprocess. The function $f_{i/\gamma}(x_1, M^2, Q^2)$ stands for the distribution function of partons $i$ with the momentum fraction $x_1$ in the photon of virtuality $Q^2$ probed at the scale $M^2$. In single resolved process one of the PDFs $f_{i/\gamma}$ is replaced by the $\delta$-function $\delta(1-x)$. Both PDFs are replaced by the combination $\delta(1-x_1)\delta(1-x_2)$ in the direct process.

Assuming the binary process as in Fig. 2.3 and massless partons, the fractions $x_1$ and $x_2$ can be calculated as follows

$$x_1 = \frac{E_{T_1} e^{-\eta_1} + E_{T_2} e^{-\eta_2}}{2E_{\gamma_1}} \tag{2.14a}$$

$$x_2 = \frac{E_{T_1} e^{\eta_1} + E_{T_2} e^{\eta_2}}{2E_{\gamma_2}} \tag{2.14b}$$

where $E_{T1}$ and $E_{T2}$ are the transverse energies of the outgoing partons, $\eta_1$ and $\eta_2$ are their pseudorapidities defined as $\eta = -\ln\tan\theta/2$, $E_{\gamma_1}$ and $E_{\gamma_2}$ are the photon energies. For direct process both $x_1$ and $x_2$ are equal 1, for single resolved process one of $x_1$ and $x_2$ is equal 1 and the other is less than 1 and both fractions are less than 1 for double resolved process.

In practice the fractions $x_1$, $x_2$ are usually calculated using the formula

$$x_{1,2} = \frac{\sum_{jet=1}^{2}(E_{jet} \pm p_{z\,jet})}{\sum_{h=1}^{n}(E_h \pm p_{zh})} \tag{2.15}$$

which is better suited for experimental conditions in anti-tagged collisions. In this case, however, the obtained fractions are just approximations of true $x_1$, $x_2$. Full reconstruction of the event kinematics needed by formula (2.14) is possible only in double-tag events.

The differential cross section in formula (2.13) depends on the gluon distribution function in the photon $g(x)$ and on the quark distribution functions of the photon $q_i(x)$. As it is difficult to extract separately distribution functions of gluons and all quark flavours from the data, it is common to use the concept of the so-called effective parton distribution function introduced in [5]

$$f^{eff}(x, {E_T}^2, P^2) = \sum_i (q_i(x, {E_T}^2, P^2) + \overline{q}_i(x, {E_T}^2, P^2)) + \frac{9}{4} g(x, {E_T}^2, P^2) \tag{2.16}$$

The matrix elements for the most important contributions of parton-parton scattering have similar dependence on the $\theta$, the differential cross section (2.13) can be then approximated as follows

$$\frac{d\sigma}{dy_1 dy_2 dx_1 dx_2 d\cos\theta^\star dQ^2 dP^2} \propto \frac{1}{s} \frac{f_{\gamma/e}(y_1, Q^2)}{y_1} \frac{f_{\gamma/e}(y_2, P^2)}{y_2} \times \frac{f^{eff}(x_1, {E_T}^2, Q^2)}{x_1} \frac{f^{eff}(x_2, {E_T}^2, P^2)}{x_2} |M_{eff}(\cos\theta^\star)|^2 \tag{2.17}$$

[4]The proportionality factor depends just on the normalisation of the wave function. The invariant amplitudes for binary parton processes are given in Table 2 later in this chapter.

The matrix elements $M_{eff}(\cos\theta^\star)$ is the same as the matrix element for the process $q_\alpha q_\beta \to q_\alpha q_\beta$ for quarks of distinct flavour $\alpha \neq \beta$ as given in Table 2.

| *Process* | $\frac{\langle \mid M \mid^2 \rangle}{g^4}$ |
|---|---|
| $q_\alpha q_\beta \to q_\alpha q_\beta$ | $\frac{2}{9}\left[\frac{2(s^2+u^2)}{t^2} + \left(\frac{2(t^2+s^2)}{u^2} - \frac{1}{3}\frac{4s^2}{ut}\right)\delta_{\alpha\beta}\right]$ |
| $q_\alpha \overline{q}_\beta \to q_\alpha \overline{q}_\beta$ | $\frac{2}{9}\left[\frac{2(s^2+u^2)}{t^2} + \left(\frac{2(t^2+u^2)}{s^2} - \frac{1}{3}\frac{4u^2}{st}\right)\delta_{\alpha\beta}\right]$ |
| $qg \to qg$ | $\left[\left(1 - \frac{us}{t^2}\right) - \frac{4}{9}\left(\frac{s}{u} + \frac{u}{s}\right) - 1\right]$ |
| $gg \to q\overline{q}$ | $\frac{1}{6}\left[\frac{u}{t} + \frac{t}{u}\right] - \frac{3}{4}\left[1 - \frac{ut}{s^2}\right] + \frac{3}{8}$ |
| $q\overline{q} \to gg$ | $\frac{64}{9} M(gg \to q\overline{q})$ |
| $gg \to gg$ | $\frac{8}{9}\left[-\frac{33}{4} - 4\left(\frac{us}{t^2} + \frac{ut}{s^2} + \frac{st}{u^2}\right)\right] - \frac{9}{16}\left[45 - \left(\frac{s^2}{ut} + \frac{t^2}{us} + \frac{u^2}{ts}\right)\right]$ |

Table 2.1: The squares of the invariant amplitudes for binary parton processes averaged over spin and colour. The amplitudes are expressed in terms of Mandelstam variables $s$, $t$, $u$.

## 2.1 Parameterisations of the PDF of the photon

There are several parameterisations of the photon PDF on the market. They differ in various theoretical motivations and also practical details - the set of experimental data used as an input, the choice of the input distribution and the scale $Q_0^2$ at which it is taken. In the following three most common parameterisations are briefly discussed.

- GRV (Glück, Reya and Vogt [6])

  GRV parametrisations are available in LO and in NLO versions. The starting distribution at the input scales $Q_0^2 = 0.25$ GeV$^2$ (LO version) and $Q_0^2 = 0.30$ GeV$^2$ (NLO version) are derived from the PDF of the pion.

- SaS (Sjöstrand and Schuler [7, 8])

  There are two sets, SaS 1D and SaS 2D, at different input scales $Q_0^2 = 0.36$ GeV$^2$ and $Q_0^2 = 4$ GeV$^2$ respectively. The shape is very similar for 1D and 2D but they are composed of different portions of VMD and perturbative parts.

- GRS ((Glück, Reya and Schienbein [9]) These parametrisations are an update of GRV with more recent data. They take into account the virtuality of the photon $P^2$. The input scale is $Q_0^2 = 0.5$ GeV$^2$

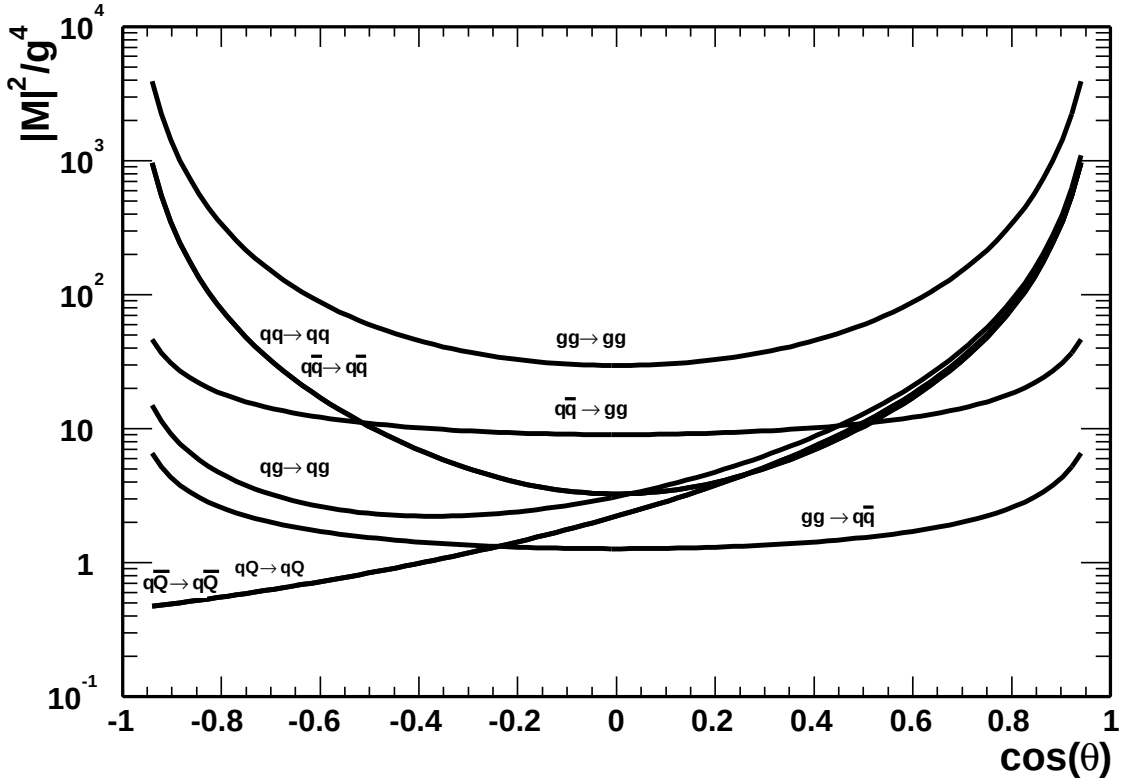


Figure 2.4: The invariant amplitudes for parton-parton scattering averaged over spin and colour (Table 2) plotted as a function of $\cos(\theta)$. In order of decreasing values at $\cos\theta = -0.8$ the amplitudes of $gg \to gg$, $qq \to qq$ (identical to $q\overline{q} \to q\overline{q}$), $q\overline{q} \to gg$, $qg \to qg$, $gg \to q\overline{q}$, $q\overline{Q} \to q\overline{Q}$ (identical to $qQ \to qQ$) are shown. For brevity the symbols $q_\alpha q_\beta$ were replaced by $qq$ in case of the same quark flavours and $qQ$ when quark flavours are different.

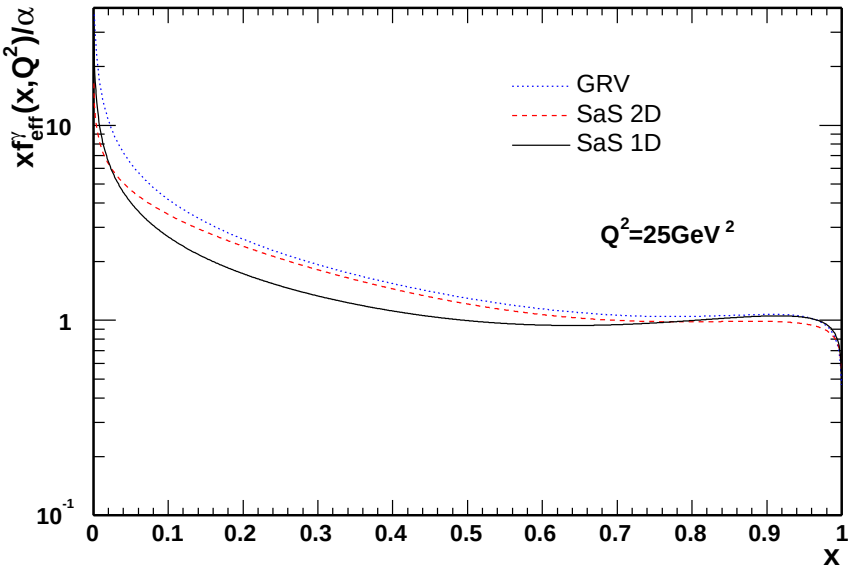


Figure 2.5: Comparison of the three parameterisations GRV-LO (dotted), SaS 1D (solid) and SaS 2D (dashed). The effective PDF is calculated at the scale $Q^2 = 25$ GeV$^2$.

As illustration of their differences the corresponding effective PDF are shown in Fig. 2.5. The differences in the predictions for the distributions of $x_{1,2}$ and $E_{T1,2}$ calculated with HERWIG[5] are shown in Fig. 2.6.

## 2.2 Jets

Partons produced in the hard subprocess are not directly observable. According to QCD they have to undergo hadronization. In this process the set of coloured objects, quarks and gluons, is converted into colourless hadrons. In hard collisions the hadronization results in bunches of collimated particles flying mostly in the direction of the primary hard partons. The information on partons produced in the hard subprocess can thus be obtained from the clusters of secondary particles which follow the direction of the primary parton. These groups of particles are called jets.

To move from this qualitative picture of the final state to a more quantitative description one needs a definition how to construct jets. Such definitions should have a close correspondence to the parton-level final state and the algorithm should be well suited for comparison with theoretical calculations. There are two main categories of the jet algorithms - the cone and the cluster algorithms.

[5]Monte Carlo event generators are introduced later in Chapter 5.

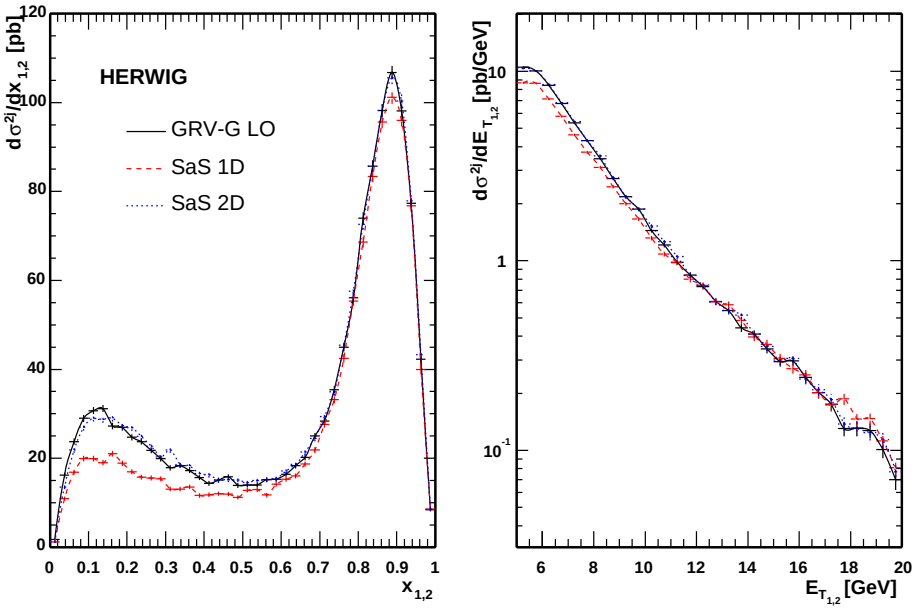


Figure 2.6: Hadron level plots of $d\sigma^{2j}/dx_{1,2}$ (left) and $d\sigma^{2j}/dE_{T\,1,2}$ for dijet events $E_{T_{1,2}} > 5$ GeV and $|\eta_{1,2}| < 1.5$ generated with HERWIG with three different parameterisations of the photon PDF. Within HERWIG which does not treat separately VMD part and perturbative part of the SaS sets the effect of the SaS 2D is very similar to GRV-LO.

Cone jet algorithms are based on geometrical consideration that particles belonging to one jet should be close to each other in the angular coordinates.

The cone algorithm proceeds in the following steps:

1. Particles above certain $p_T$ limit are taken as jet seeds. The jet pseudorapidities $\eta^{jet}$ and azimuth angle $\phi^{jet}$ are calculated.

2. All particles satisfying
$$R = \sqrt{(\Delta\eta)^2 + (\Delta\phi)^2} < R_{cone} \tag{2.18}$$
where $\Delta\eta = \eta^{jet} - \eta^i$ and $\Delta\phi = \phi^{jet} - \phi^i$ are assigned to the respective jets. $R_{cone}$ is a parameter of the algorithm.

3. Jet axes and energies are updated by the recombination scheme
$$E_T^{jet} = \sum_i E_T^i \tag{2.19a}$$
$$\eta^{jet} = \sum_i E_T^i \eta^i / E_T^{jet} \tag{2.19b}$$
$$\phi^{jet} = \sum_i E_T^i \phi^i / E_T^{jet} \tag{2.19c}$$
where the sum runs over all particles assigned to a given jet.

4. Steps 2 and 3 are repeated until a stable configuration of jets is reached.

5. If two jets overlap with more than certain fraction OVLIM of the energy of the higher $E_T$ jet, all particles belonging to the more energetic jet are assigned to this jet and the remaining are discarded. If the fraction of energy in the overlap region is smaller the particles in the overlap region are assigned to the closer of the two jets.

The actual implementation of the cone algorithm which was used in the analysis was PXCONE [10]. Its parameters are further described in Chapter 6.

## 2.3 Beam remnants

So far only hard interactions which occur in the system of the two photons have been discussed.

In the double resolved photon contribution to $\gamma\gamma$ collisions the beam remnants from the photons typically carry small transverse but large longitudinal energy. They would therefore fly mostly into the beam tube and would thus be unobserved. There are two ways how to modify this picture.

In HERWIG the soft underlying event option allows the so-called beam clusters to collide producing many soft clusters. This results, after their decay, in redistribution of the

original large longitudinal energy of particles from beam clusters into large number of soft particles populating mostly the central region. These particles are indistinguishable from those belonging to jets and may therefore influence their properties.

The mechanism of the soft collision of beam clusters does not rely on perturbative QCD but simply parameterises the longitudinal distribution of soft clusters in order to reproduce the one-particle inclusive distributions as measured by the UA5 experiment at the SPS collider at CERN.

In PYTHIA the soft underlying collision is modelled by multi-parton interaction.

The amount of energy which originates from the soft collision can best be studied in the plots of jet profiles and energy flow outside the jets. Jet profiles and energy flows are introduced in Chapter 6. The implementation of the soft underlying event in the Monte Carlo event generators is discussed in Chapter 5.

# Chapter 3

# Current status of measurements of the photon structure

The available data on photon structure as well as the corresponding theoretical framework have recently been discussed in two comprehensive review articles [11, 12]. The former contains also a fairly detailed analysis of existing parametrisations of PDF of the photon. Most of these parameterisations are extracted from data on the photon structure functions $F_2^\gamma(x, Q^2)$ measured in deep inelastic scattering of electrons on the quasi-real photons at electron-positron colliders. However, as the quantity and precision of these data are still insufficient for reasonably unambiguous extraction of these PDF, additional theoretical assumptions are usually employed as well.

In Fig. 3.1 we show some of the data on $F_2^\gamma$ and in Fig. 3.2 the corresponding parton distribution functions extracted by several groups using basically the same data, which included the following experiments at $e^+e^-$ colliders

- PLUTO, JADE, CELLO and TASSO at PETRA in DESY [13],
- AMY, TOPAZ at TRISTAN in KEK [14],

| model | # of ind. par. | # of data points | | | |
|---|---|---|---|---|---|
| | | 205 | | 182 - no TPC | |
| | | $\chi^2$ | $\chi^2/_{\rm DOF}$ | $\chi^2$ | $\chi^2/_{\rm DOF}$ |
| SaS1D | 6 | 657 | 3.30 | 611 | 3.47 |
| GRS LO | 0 | 499 | 2.43 | 366 | 2.01 |
| CJKL | 3 | 406 | 2.01 | 323 | 1.80 |

Table 3.1: Comparison of $\chi^2$ values obtained for three different fits to $F_2^\gamma(x, Q^2)$. Taken from [15].

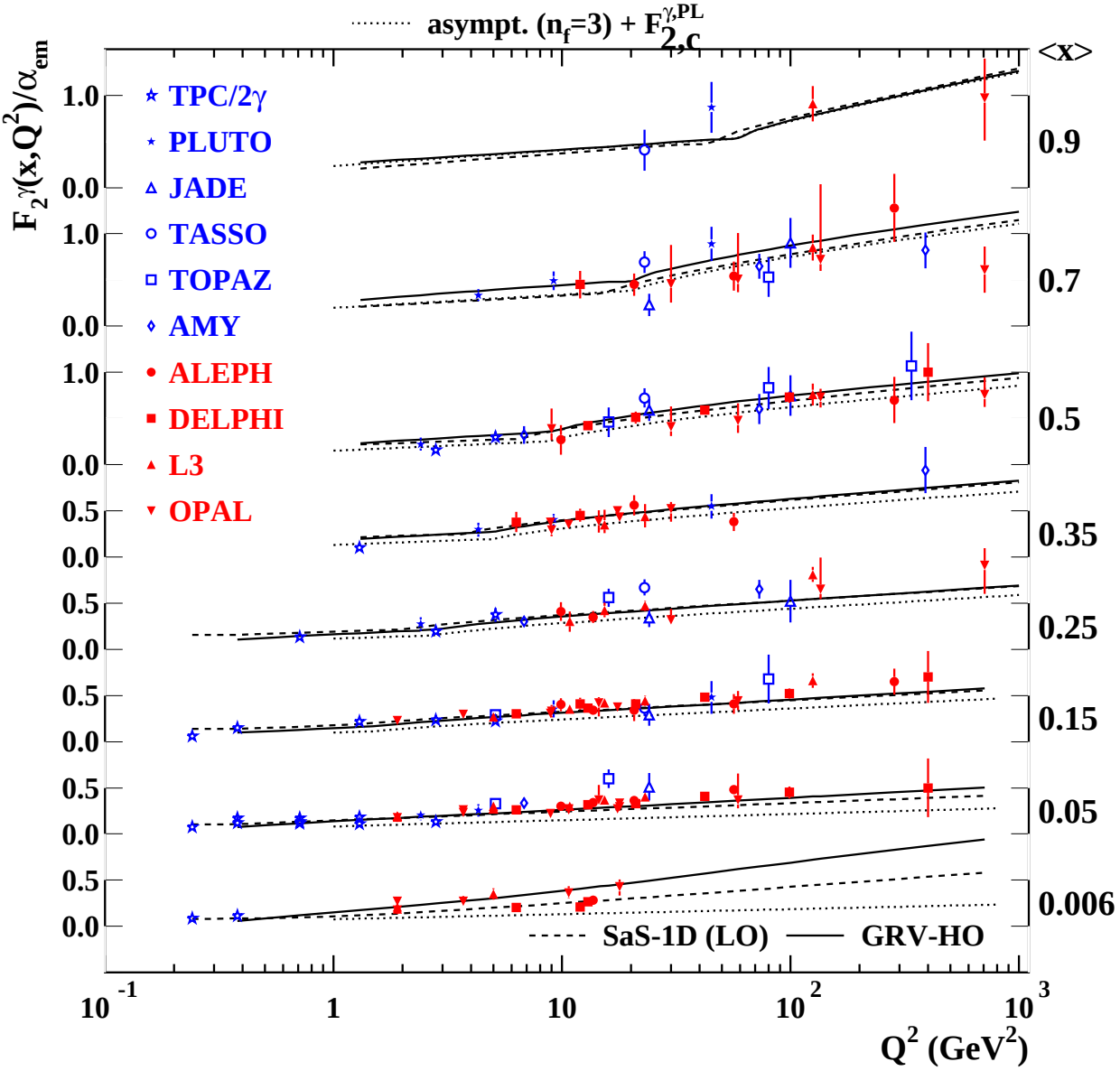


Figure 3.1: The compilation of measurements of the photon structure function $F_2^\gamma/\alpha$. Taken from [16].

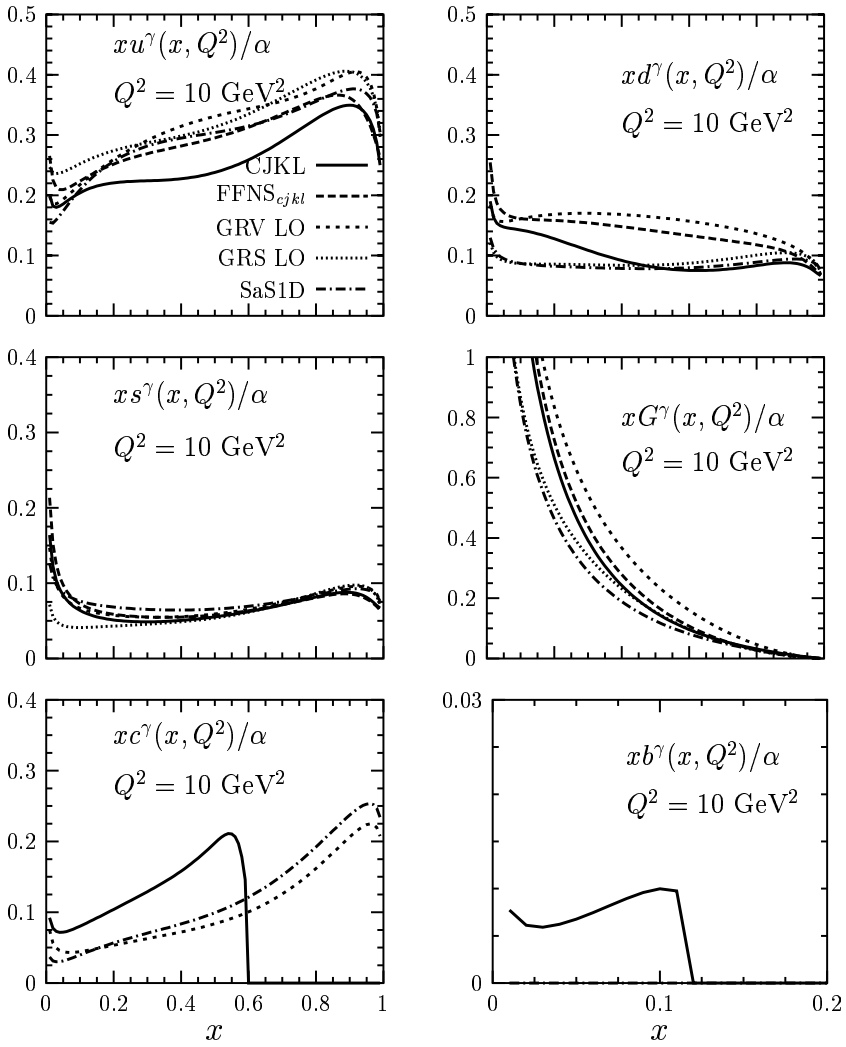


Figure 3.2: Parton distribution functions of the photon for $Q^2 = 10$ GeV$^2$ as extracted by five different parameterisations. Taken from [15].

- TPC/2$\gamma$ at PEP in SLAC [17],
- ALEPH, DELPHI, L3, OPAL at LEP at CERN [18].

The quality of the corresponding fits is summarised in Table 3.1. Note large differences between the forms of both the quark and gluon distribution functions and the fact very few data exist below $x \simeq 0.1$.

This stands in sharp contrast with our knowledge of structure of nucleons. To illustrate this difference we show in Fig. 3.3 and in Fig. 3.4 the summary of the results on the proton structure function $F_2^p(x, Q^2)$ as measured in deep inelastic scattering of electrons or muons on the nucleons in older CERN [19] and recent HERA [20] experiments. In Table 3.2 the quality of the global fit made by the MRST group [21] of these and other data [1] and in Fig. 3.5 quarks and gluon distribution functions obtained from global analysis of current data by three main groups are plotted and compared to the result of one older global fit. Note that the three recent parametrisations are quite close to each other for $x$ down to $x \simeq 10^{-4}$ and that the high quality of the fit, which yields $\chi^2/\mathrm{DOF} \simeq 1$. In both cases, the number of free parameters in the fits is around 20.

Beside the measurement of $F_2^\gamma(x, Q^2)$ the structure of the photon has been investigated in four other types of experiments:

- jet production in $\gamma p$ collisions at HERA [22],
- jet production in $\gamma\gamma$ collisions at LEP [23, 24],
- heavy quark production $\gamma p$ collisions at HERA [25],
- heavy quark production $\gamma\gamma$ collisions at LEP [26].

So far the parametrisations of the structure of the photon have been based entirely on the data from the deep inelastic scattering. An important feature of the PDF is its universality, i.e. the same PDF should describe different processes. As an illustration of this universality we show in Fig. 3.6 the comparison of dijet cross-section $d\sigma^{2j}/dE_T$ as measured by OPAL at LEP 2 with PYTHIA using the PDF SaS 1D. If there are sufficient data from other processes than DIS they should be used in global fits of the PDF.

[1] These analyses include data on the production of Drell-Yan large mass dilepton pairs, $W^\pm$ and $Z$, jets and direct photons.

| Data set | No. of data pts | MRST | MRST 0.117 | MRST 0.121 | MRST J |
|---|---|---|---|---|---|
| H1 $ep$ | 400 | 382 | 386 | 378 | 377 |
| ZEUS $ep$ | 272 | 254 | 255 | 258 | 253 |
| BCDMS $\mu p$ | 167 | 193 | 182 | 208 | 183 |
| BCDMS $\mu d$ | 155 | 218 | 211 | 226 | 219 |
| NMC $\mu p$ | 126 | 134 | 143 | 127 | 135 |
| NMC $\mu d$ | 126 | 100 | 108 | 95 | 100 |
| SLAC $ep$ | 53 | 66 | 71 | 63 | 67 |
| SLAC $ed$ | 54 | 56 | 67 | 47 | 58 |
| E665 $\mu p$ | 53 | 51 | 50 | 52 | 51 |
| E665 $\mu d$ | 53 | 61 | 61 | 61 | 61 |
| CCFR $F_2^{\nu N}$ | 74 | 85 | 88 | 82 | 89 |
| CCFR $F_3^{\nu N}$ | 105 | 107 | 103 | 112 | 110 |
| NMC $n/p$ | 156 | 155 | 155 | 153 | 161 |
| E605 DY | 136 | 232 | 229 | 247 | 273 |
| Tevatron Jets | 113 | 170 | 168 | 167 | 118 |
| Total | 2097 | 2328 | 2346 | 2345 | 2337 |

Table 3.2: Quality of the fit for MRST2001 partons to different data sets. The first MRST column shows the $\chi^2$ values of the optimum fit with $\alpha_S(M_Z^2) = 0.119$. Also shown are the values for parton sets obtained from fits with $\alpha_S(M_Z^2) = 0.117$ and 0.121, as well as those for parton set J which has structure in the high $x$ gluon.

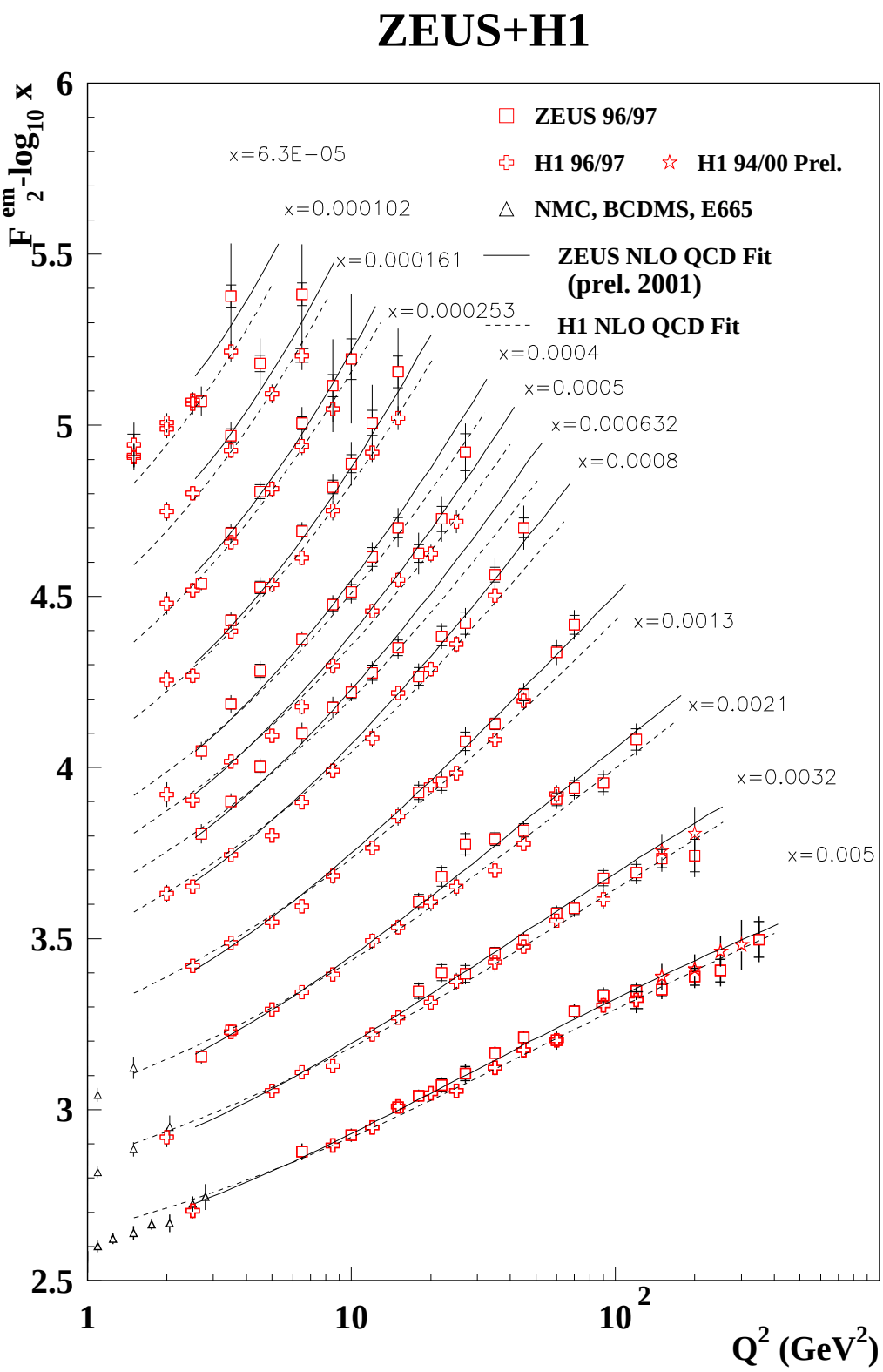


Figure 3.3: The summary of the data on the proton structure function $F_2$, low-x region. Taken from [16].

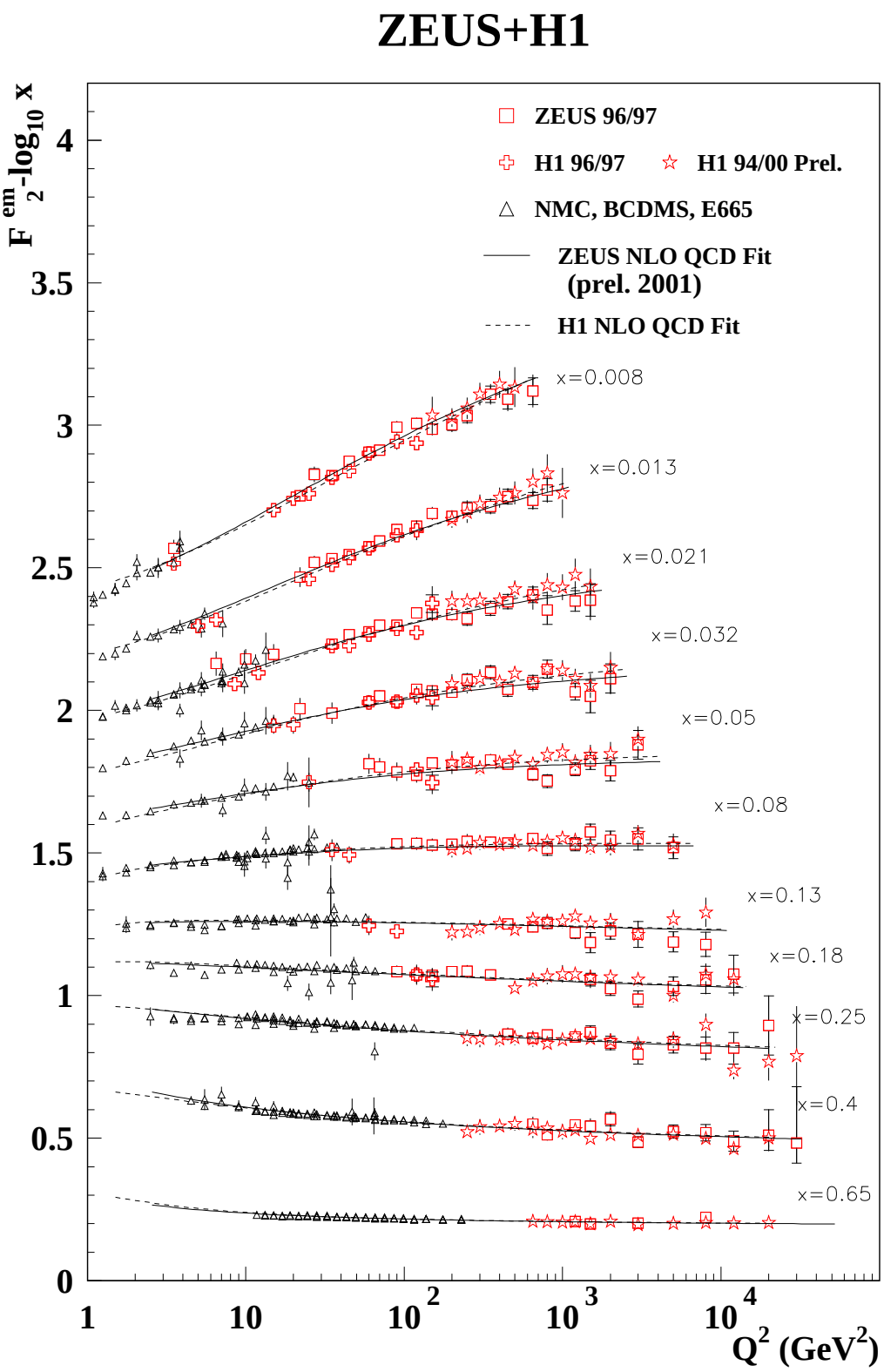


Figure 3.4: The summary of the data on the proton structure function $F_2$, high-x region. Taken from [16].

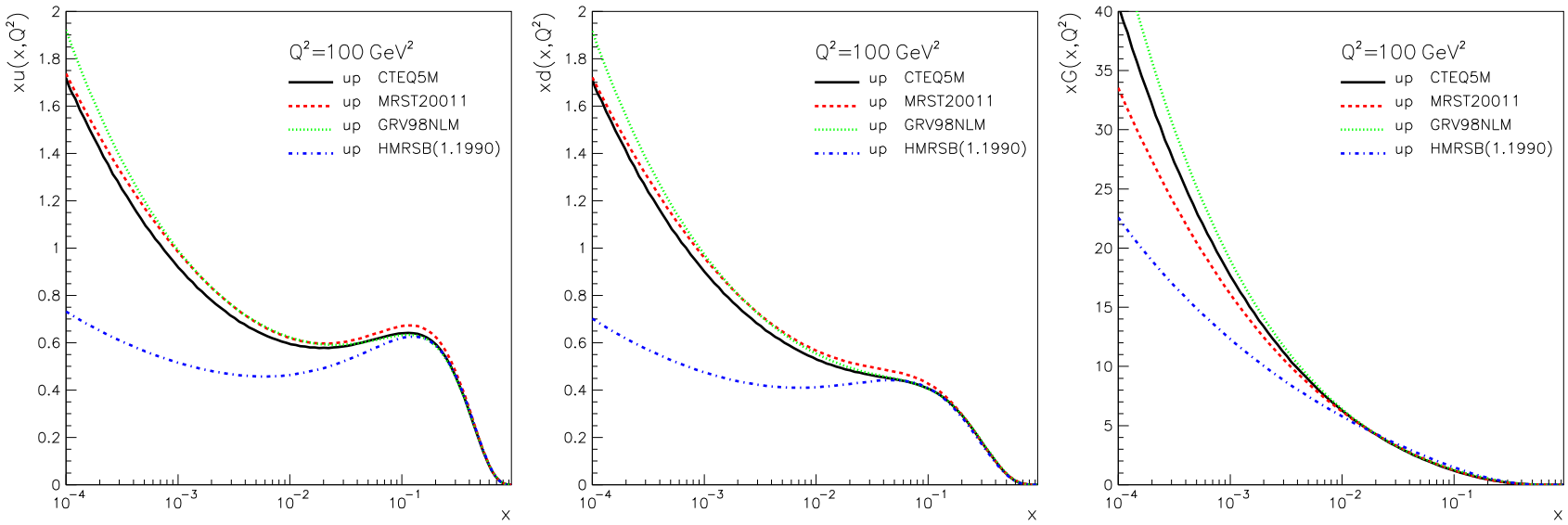


Figure 3.5: Parton distribution functions in the proton as extracted by four different parameterisations, taken from the CERN PDFLIB library of distribution functions. The first three are the recent ones obtained by CTEQ, MRS and GRV groups, the last one (dash-dotted curves) corresponds to a MRS parametrisation more than a decade old.

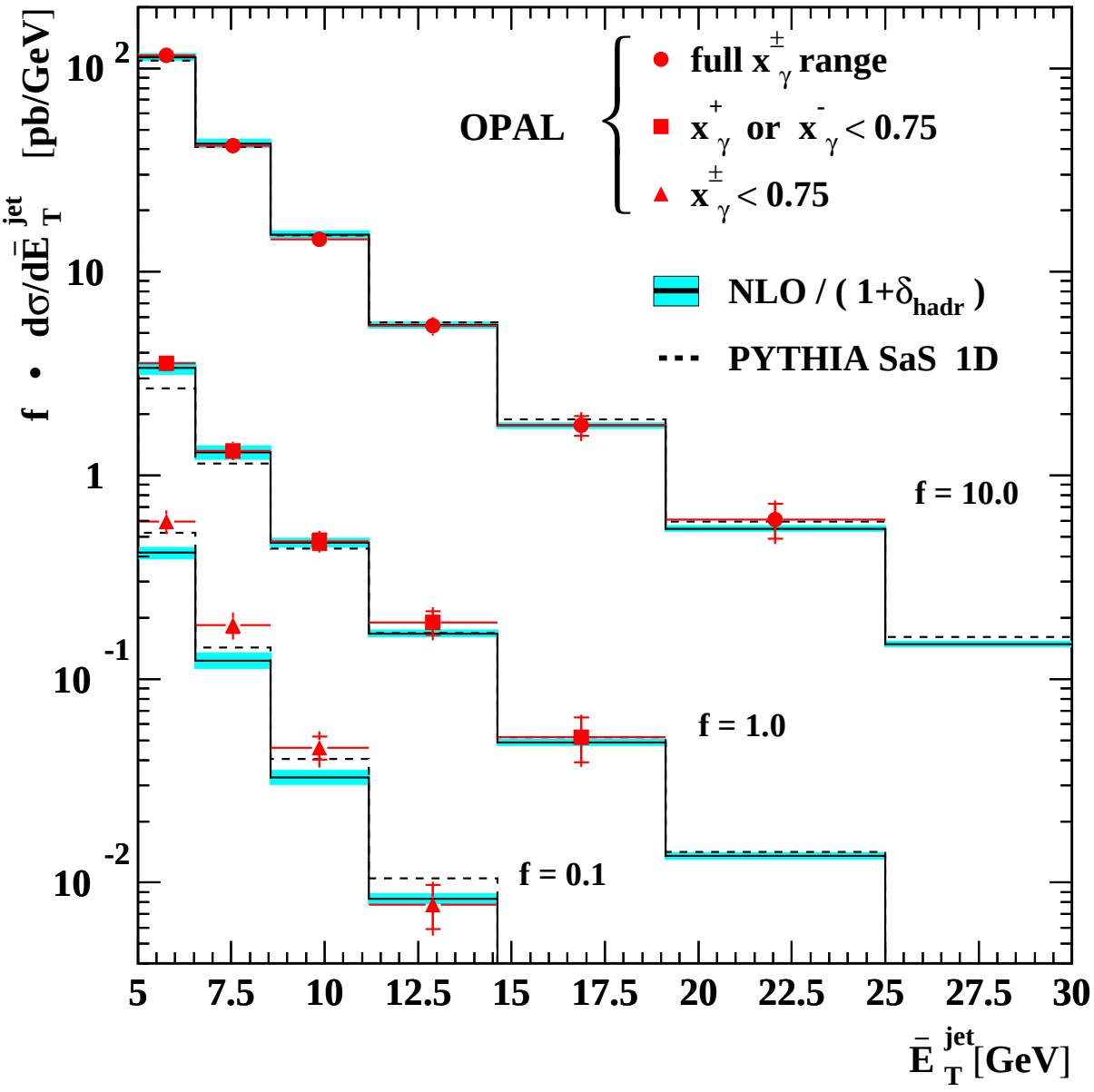


Figure 3.6: The dijet cross-section as a function of the mean transverse energy of the jets as measured by the OPAL collaboration [24]. Three lines multiplied by the indicated factors are the cross sections for the full x range (circles), $x^+$ or $x^- < 0.75$ (squares) and $x^\pm < 0.75$ (triangles), $x^+$, $x^-$ corresponds to our $x_1$, $x_2$. Results are compared with the NLO calculation and with LO event generator PYTHIA using the SaS 1D.

# Chapter 4

# The DELPHI detector at LEP

## 4.1 LEP

The **L**arge **E**lectron **P**ositron collider (LEP) had been the largest electron-positron collider in the world. The collider ring had 27 km circumference and its tunnel was excavated about 100 m below the surface. It was built at CERN near Geneva and commissioned in 1989. During the first phase from 1989 to 1995 LEP was colliding electrons and positrons at energies around the $Z^0$ mass. Four LEP experiments ALEPH, DELPHI, L3 and OPAL collected each about 150 $pb^{-1}$ in this period of time which was equivalent of approximately 4 millions of hadronic Z decays per experiment. The high statistics allowed precise tests of the electroweak interaction and the Standard Model. Measurements performed at LEP1 have provided accurate values of the properties of the Z boson and other parameters of the Standard Model.

LEP was upgraded in 1995 to reach centre-of-mass energies for pair production of intermediate bosons $W^+$ and $W^-$. The existing radio-frequency cavities made of copper were supplemented by superconducting cavities of Niobium to achieve higher beam energies. The machine luminosity was increased by operation in so called bunch train mode when several bunches arrived at the interaction point during beam-crossing time[1].

The information about the integrated luminosities collected by DELPHI during high-energy runs is given in Table 4.1. At the end of LEP operation centre-of-mass energies of 208.8 GeV, far beyond its upgrade goal, were achieved. The collider was shut down in November 2000.

LEP experiments have provided many important results concerning the Standard Model.

- The mass of the intermediate boson Z was measured with high accuracy of $m_Z = 91.1874 \pm 0.0021$GeV together with the width of Z and its line shape. From the Z width and branching ratios of Z the number of light neutrino families $N_\nu = 2.9841 \pm 0.0083$

[1]Standard LEP operation was with 4 bunches of electrons against 4 bunches of positrons with beam crossing time every 22$\mu$s.

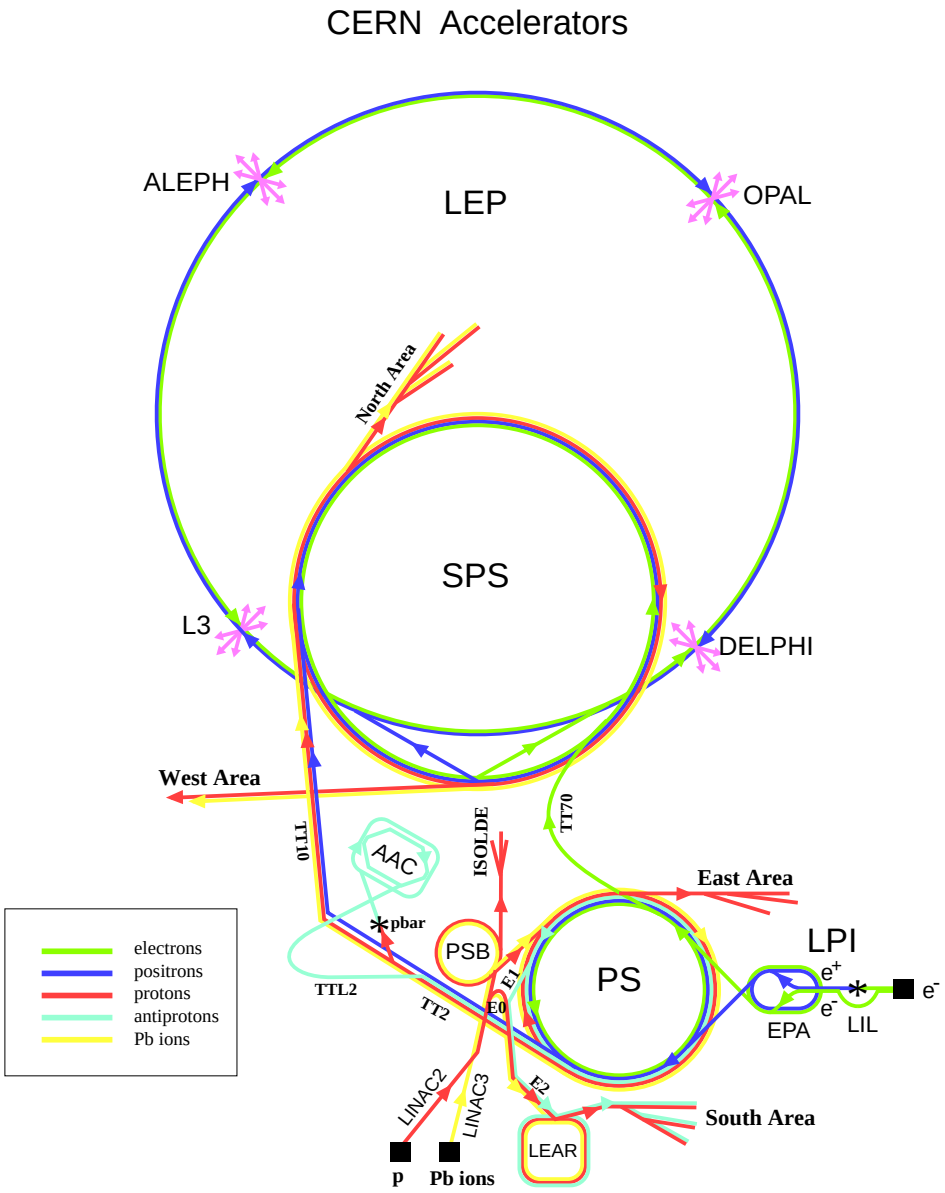


Figure 4.1: Schematic view of the LEP and the acceleration complex at CERN. In the last step electrons and positrons with energy 22 GeV from SPS were injected into LEP.

was determined. Forward-backward asymmetries $A_{FB}^f$ at the Z peak, the effective vector and axial-vector coupling constants $g_V^f$ and $g_A^f$ and the branching ratios of Z to b and c quarks ($R_b^0$ and $R_c^0$) were measured.

- The mass of the W boson was obtained from direct measurement with a precision of $m_{\mathrm{W}} = 80.450 \pm 0.026(\mathrm{stat.}) \pm 0.030(\mathrm{syst.})$. Couplings of the three gauge bosons were studied directly for the first time.

- Throughout the LEP running the energy range accessible by the collider was scanned for Higgs boson and new physics beyond the Standard Model. Lower limit on the on the Higgs mass was given $m_H > 114.1$ GeV [27].

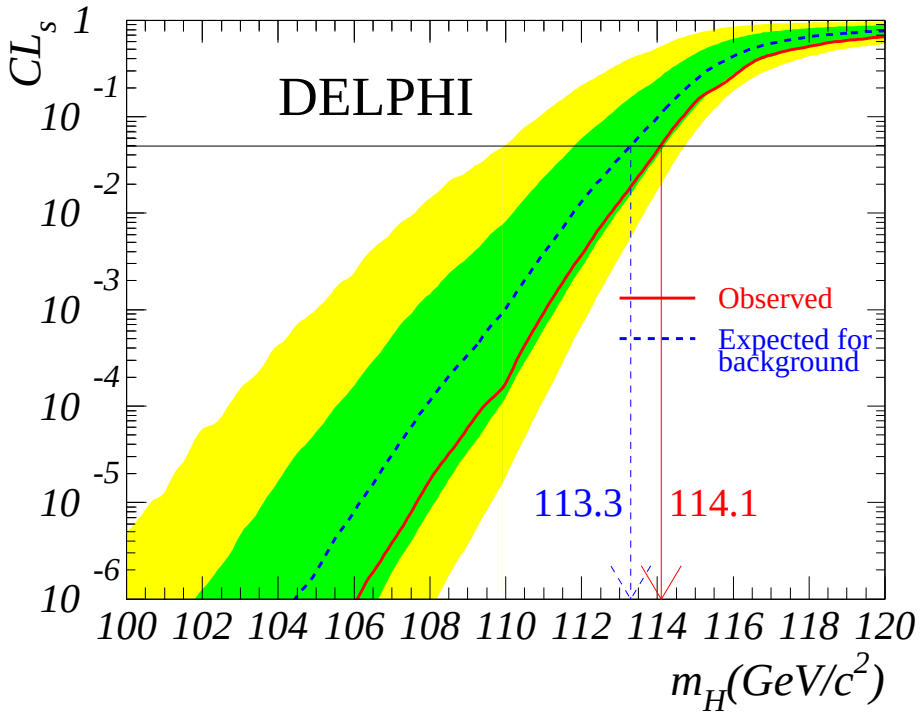


Figure 4.2: DELPHI limit on the Standard Model Higgs mass. 95% confidence level lower limit on the Higgs mass is shown by red arrow. Full (dashed) curve is the observed (expected) median confidence from experiments with only background channels. Bands represent hypotheses of only background processes at 68.3% (and 95%) confidence level.

- LEP experiments performed also a number of QCD studies. Strong interaction constant $\alpha_S(m_Z)$ was measured from jet rates and other event shape variables. Combined fit gives $\alpha_S(m_Z) = 0.1195 \pm 0.0047$ in which the error is governed by theoretical uncertainties.

- LEP experiments were equipped with precise vertex detectors which started a new era in B-physics. Lifetimes of B-mesons were measured with substantially higher precision and oscillations of $B - B^{\circ}$ were studied.

Table 4.1: Integrated luminosity for high energy runs as collected by DELPHI

| Year | 1995 | | 1996 | | 1997 | 1998 | 1999 | | | |
|---|---|---|---|---|---|---|---|---|---|---|
| $E_{cm}$ [GeV] | 130 | 136 | 161 | 172 | 183 | 189 | 192 | 196 | 200 | 202 |
| Lumi [$pb^{-1}$] | 2.9 | 3.0 | 9.6 | 10.2 | 54.1 | 157.7 | 25.8 | 77.4 | 83.8 | 36.9 |
| Year | 2000[2] | | | | | | | | | |
| $E_{cm}$ [GeV] | 205 | 207 | | | | | | | | |
| Lumi [$pb^{-1}$] | ∼80 | ∼140 | | | | | | | | |

## 4.2 The DELPHI detector

The DELPHI (**De**tector with **L**epton, **P**hoton, **H**adron **I**dentification) detector was one of the four detectors at LEP. It operated successfully since 1989 until 2000. Details on the design and operation of the DELPHI detector can be found in [28, 29], in the following mainly the parts relevant for this analysis are discussed.

The general layout of the detector is shown in Figure 4.3. The detector was designed to cover full solid angle. It consisted of a barrel part and two endcaps. The barrel surrounded the beam pipe where at the centre of the detector electrons collided with positrons. Charged particles were subject to an uniform electromagnetic field of 1.23T parallel to the beam pipe. The field was produced by a superconducting solenoid. The coordinate system adopted in DELPHI had z axis defined by the direction of electron beam, x axis pointing to the LEP centre and y pointing upwards. If not specified $\theta$ ($\phi$) denote polar (azimuthal) angle respectively.

Information from different subsystems of the detector was combined to build complete picture of the event. Several tracking detectors provided track measurement for charged particles. From the track curvature in the magnetic field of the superconducting magnet the track momentum and charge of the particle were reconstructed. Measurements of ionisation loss along the trajectory aided particle identification. Energy measurement for both charged and neutral particles was provided by calorimetry. Electrons and photons were absorbed by electromagnetic calorimeters while hadrons were absorbed by the hadron calorimeter located farther from the interaction point. Particle identification for charged particles was improved by detectors of Čerenkov radiation. High energy muons were identified by reaching the outmost layers of the detector (muon chambers) and by narrow track in the highly-granular hadron calorimeter. Acceptance gaps in the electromagnetic calorimetry were covered by

[2]The luminosity was delivered at various energies near 205 and 207 GeV in 2000.

scintillation counters around dead spaces in the barrel electromagnetic calorimeter and installation of the photon taggers at 40° in polar angle where the barrel and forward calorimeters did not overlap.

The description of the DELPHI detector is organised as follows. Tracking detectors are described first in order of appearance from the interaction point to the outer layers. Then the description of the calorimetry is given followed by Čerenkov detectors and other specialised devices.

### 4.2.1 Tracking detectors

#### Microvertex detector

The Microvertex Detector (VD) surrounded the beam pipe in three layers at radii 6.3, 9.0 and 10.9 cm. Detector layers were made of double-sided silicon strip detectors arranged in 24 sectors with overlaps between adjacent modules. The outer and closer layer provided both $R\phi$ and $z$ coordinates while the middle one measured only in $R\phi$ direction.

#### Very forward tracker

The VD detector was extended in the forward region by so-called Very Forward Tracker (VFT) consisting of pixel and ministrip detectors. After the upgrade it covered region down to 10° in polar angle. Sketch of the combined vertex detector is given in Figure 4.4.

#### Inner detector

The Inner detector was located between radii 12 and 23 cm providing fast tracking information which was also used for trigger. It consisted of inner drift jet chamber surrounded by five layers of cylindrical MWPC (so-called straw tubes). Polar angle coverage of the device was down to 15°.

#### Time Projection Chamber

Time Projection Chamber (TPC) was the central device for particle tracking. It filled the barrel region between radii 40 and 110 cm and length of 2x130 cm in z in both endcaps. The readout was organised into six azimuthal sectors on each end plate with 16 circular pad rows and 192 sense wires in total. Apart from its crucial role in particle tracking the information on $dE/dx$ obtained in TPC was used for particle identification. The layout of the TPC operation is shown in Figure 4.5.

#### Outer detector

The Outer detector (OD) was installed between the barrel RICH and the electromagnetic calorimeter (HPC). It consisted of 5 layers of drift tubes operated in limited streamer mode.

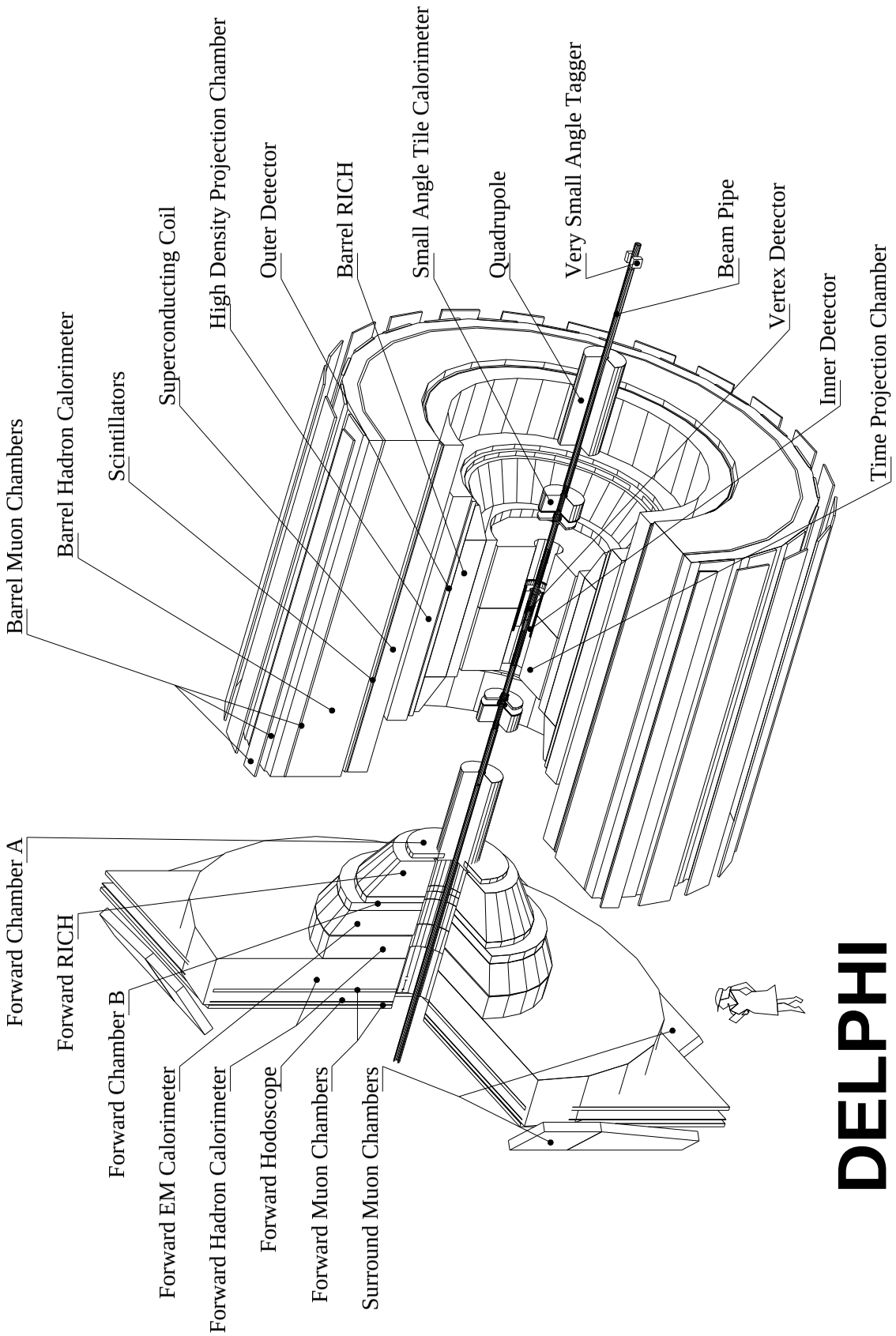


Figure 4.3: General layout of the DELPHI detector

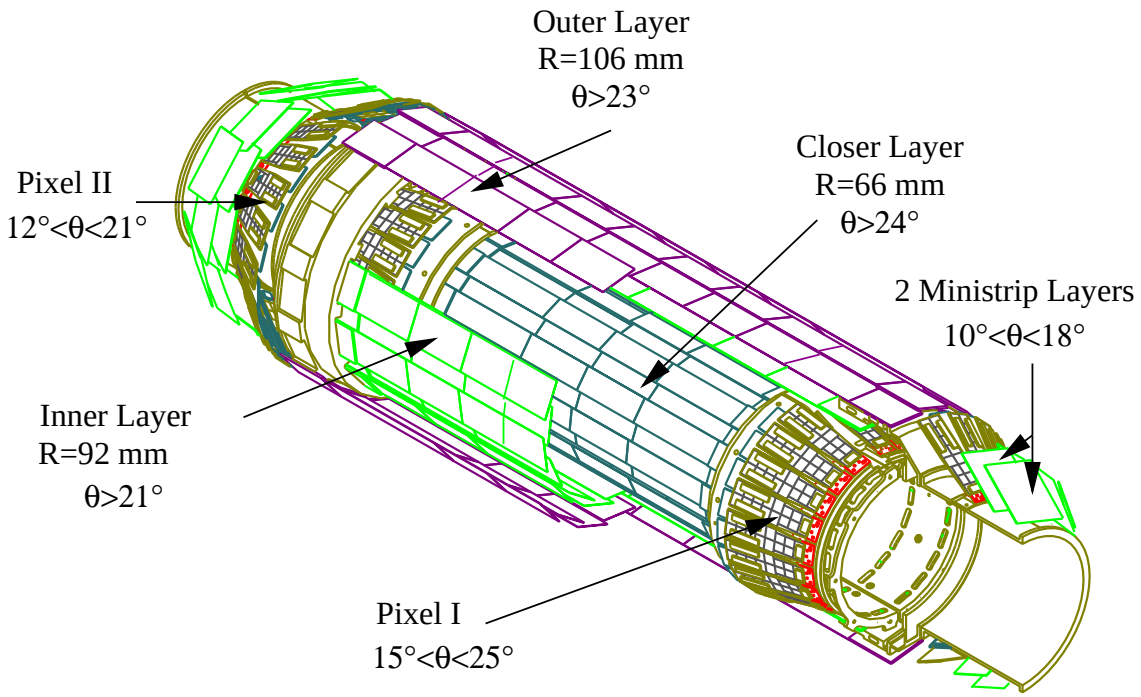


Figure 4.4: A sketch of the combined silicon tracker. The cylindrical part are the three layers of VD. Four crowns of detectors at the ends of VD are two layers of pixel and two layers of ministrip detectors of VFT.

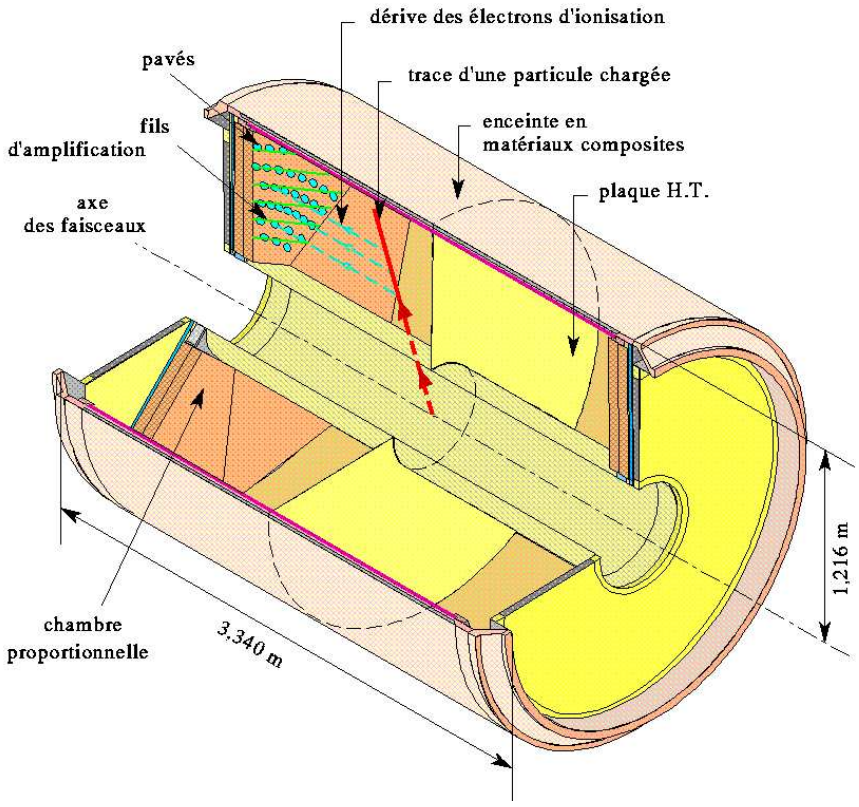


Figure 4.5: Design of the TPC and its operation principle. Charged particles ionise the gas along the track. The chamber is filled with Ar:$CH_4$ mixture (80:20). The free charge is drifting along the drift field towards the end plates where it is detected by multiwire proportional chambers (MWPC). The MWPC provide xy coordinates of the track segments. The z coordinate is reconstructed from the drift time.

It occupated space between 197 and 206 cm in z. The coverage in polar angle was down to 39°. The detector was used to aid track reconstruction for tracks with large momenta for which TPC dimensions were not sufficient.

#### Forward Chamber A

Forward chambers FCA were drift chambers covering angles between 11 and 32° at 160 cm in $|z|$. Each chamber was made up of two 2 planes of drift tubes positioned near end plates of TPC.

#### Forward Chamber B

Another two layers of drift chambers were located between the forward RICH detector and forward electromagnetic calorimeter FEMC at $z = 275$cm in both endcaps. The acceptance of FCB ranged from 10 to 25° in polar angle.

#### Muon chambers

Muon chambers were tracking detectors installed behind the hadronic calorimeter. Muons with energy above 3 GeV were capable to reach the muon systems. There was a barrel part (MUB) and two forward parts (MUF). A gap between MUB and MUF was covered by Surrounding Muon Chambers (SMC).

The acceptance and the resolution of tracking detectors is summarised in Table 4.2.

### 4.2.2 Calorimeters

#### High Density Projection Chamber

The High-density Projection Chamber (HPC) was a lead electromagnetic calorimeter occupying space between 208 and 260 cm down to 40° in polar angle. 18 radiation lengths $X_0$ of lead wires were arranged in 6 radial layers with gas volume inbetween them. Electric field along the layer served as a drift field. Shower coordinate in z was measured from the drift time to the read-out pads. Readout granularity was 1° in $\phi$ and 4 mm in the drift coordinate z.

#### Forward Electromagnetic Calorimeter

Forward Electromagnetic Calorimeter (FEMC) was the largest electromagnetic calorimeter in the endcaps. It was installed behind the FCB. It was a Čerenkov light counter assembled from blocks of lead glass. The signal is read-out by a phototriode. Each block was a truncated pyramid with dimensions $5 \times 5$ cm$^2$ ($5.6 \times 5.6$ cm$^2$) and length of 40 cm.

Table 4.2: Tracking detectors at DELPHI [28]

| Detector | Acceptance | | | No.points along track | Resolution per point [mm] |
|---|---|---|---|---|---|
| | $R$[cm] | $z$[cm] | $\theta$[°] | | |
| VD | 9/11 | 12 | 37-143 | 3 | $R\phi$:0.007,z:0.009 |
| VFT | | | 10-25 | 4 | $x$,$y$ 0.1 |
| ID:jet | 11.8-22.3 | 40 | 17-163 | 24 | $R\phi$:0.09 |
| ID:straws | 23-28 | $\leq 50$ | 30-150 | 5 | $z$:$\leq 1$ |
| TPC | 35-111 | $\leq 134$ | 20-160 | 16<br>192 | $R\phi$:0.23<br>$z$:0.9 |
| OD | 198-206 | $\leq 232$ | 43-137 | 5*$R\phi$<br>3*$z$ | $R\phi$:0.11<br>$z$:44 |
| MUB | $\sim 445$<br>$\sim 485$ | $\leq 185$ | 52-138 | 2 (+2) | $R\phi$:1.5<br>$z$:10 |
| FCA | 30-103 | 155-165 | 11-33 | $2 * (x, u, v)$ | $x$,$u$,$v$:0.3 |
| FCB | 53-195 | 267-283 | 11-35 | $4 * (x, u, v)$ | $x$,$u$,$v$:0.25 |
| MUF | 70-460 | 463<br>500 | 9-43 | $(2 + 2) * (x, y)$ | $x$,$y$:1.0 |

**Small Angle Tile Calorimeter**

The Small Angle Tile Calorimeter (STIC) was an electromagnetic sampling calorimeter composed of lead plates interspaced with scintillator layers. The scintillation light from 47 scintillator layers was collected by optical fibres. Detector covered angular region of 29-188 mrad and was used for anti-tagging scattered electron beams in this thesis.

**Hadron calorimeter**

Hadron calorimeter HCAL consisted of a barrel part ($43° < \theta < 137°$) and two endcaps ($11° < \theta < 49°$). It was a sampling gas detector consisting (in the barrel part) of 21 layers of iron plates of the total radiation length $6\lambda$ interspaced with layers of limited streamer tubes. The plastic tubes were coated with graphite and were filled with $Ar/CO_2$/i-butane mixture. The detector signal was read out from pads arranged in towers and also directly from the sensitive tubes (so called cathode read-out) providing higher granularity in azimuthal angle. Apart from the energy measurement the calorimeter could be used for muon identification.

The overview of properties of calorimeters is given in Table 4.3.

### 4.2.3 Čerenkov detectors

Innovative part of DELPHI design was the employment of the Ring Imaging Čerenkov detectors for particle identification over almost full solid angle. For charged particles with

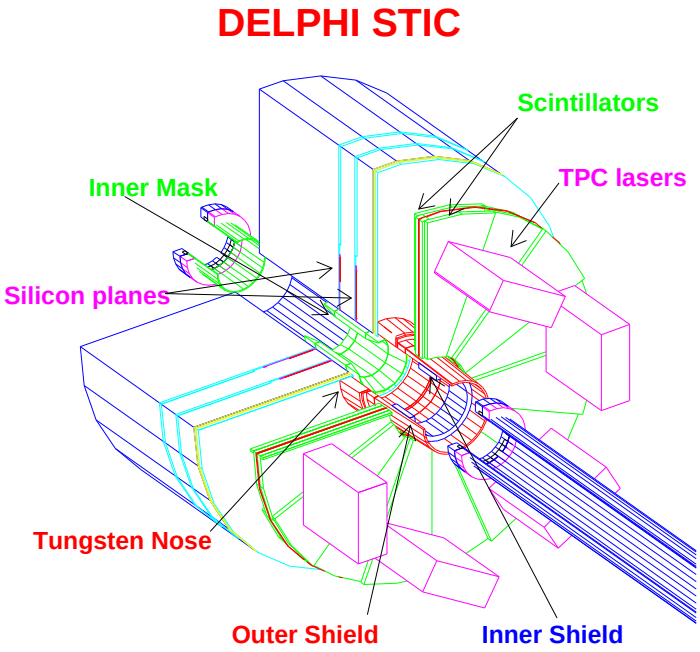


Figure 4.6: Sketch of the STIC components.

Table 4.3: Calorimeters at DELPHI [28]

| Detector | Acceptance | | | Depth | Resolution |
|---|---|---|---|---|---|
| | $R$[cm] | $z$[cm] | $\theta$[°] | | $\sigma_E/E$ [%] |
| HPC | 208-260 | $\leq 254$ | 43-137 | $18X_o$ | $23/\sqrt{E}+1.1$ |
| FEMC | 46-240 | 284-340 | 10-36.5 | $20X_o$ | 4% at 45.6 GeV |
| VSAT | 6-9 | 770 | 5-7mrad | $24X_o$ | 5% at 45.6 GeV |
| HCAL | B: 320-479<br>FW:65-460 | $\leq 380$<br>340-489 | 10-170 | $6\lambda$ | $112/\sqrt{E}+0.21$ |

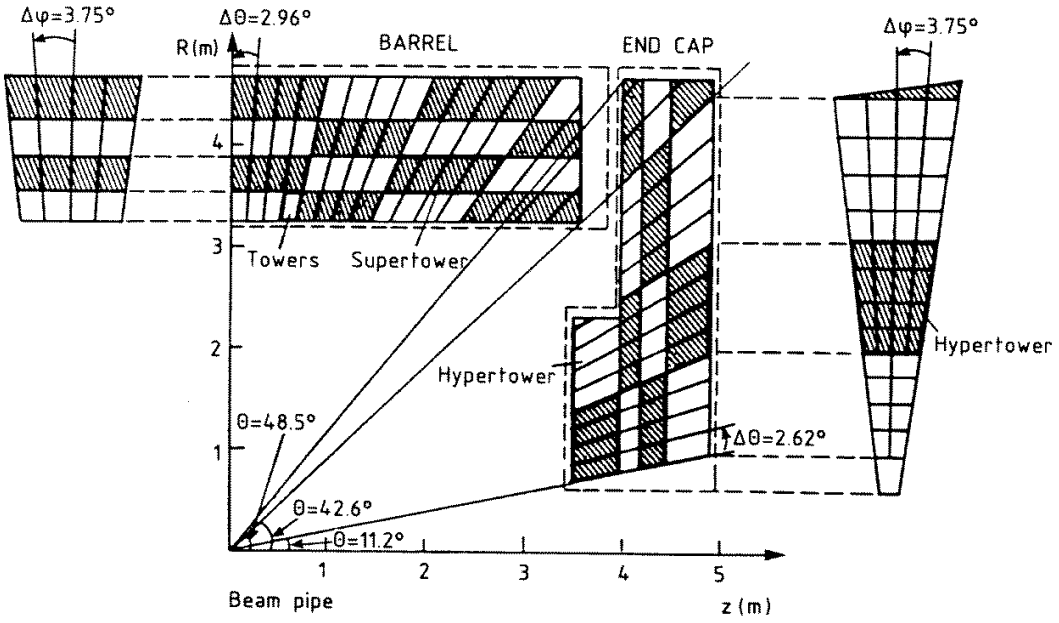


Figure 4.7: The projective geometry of the HCAL.

measured momentum RICH provides an estimate of their mass. Čerenkov detectors were installed both in the barrel and in endcaps. Combined liquid and gaseous radiators separate particles over wider range of velocities.

The Barrel RICH covered $\theta$ region between 42° to 138°. It consisted of two vessels separated by a layer of quartz plates with drift tubes and MWPC on side. The inner volume was filled with liquid radiator $C_6F_{14}$ (refractive index $n = 1.2718$). The outer gas volume of $C_5F_{12}$ ($n = 1.00194$) was equipped with mirrors to reflect Čerenkov photons onto drift tubes. Čerenkov light was detected by time-projection chamber photo-detectors with TMAE for photon conversion. Threshold momenta for emitting Čerenkov light were 0.17 GeV (pions), 0.7 GeV (kaons), 1.2 GeV (protons) in the liquid radiator and 2.3 GeV (pions), 8.2 GeV (kaons) and 16.0 GeV (protons) in the gas radiator.

The Forward RICH was located between $15° < \theta < 35°$ in polar angle ($145° < \theta < 165°$ respectively) and in the distance $1.7m < |z| < 2.7m$. It housed also liquid and gas volumes. The operation was complicated by the presence of magnetic field orthogonal to the electric drift field.

### 4.2.4 Luminosity monitor

**Very Small Angle Tagger**

The primary purpose of the VSAT was to be a precise luminosity monitor. It was a combined calorimeter and tracker system located behind beam quadrupoles giving access to smaller virtualities of the scattered beam. The detector made of tungsten plates interspaced with silicon strip detectors is in two opposite quadrants covering only one half of the possible acceptance in angular region of $\pm 45°$ in azimuth and polar angles between 5 to 7 mrad.

### 4.2.5 Data acquisition

Amount of recorded events was reduced by the trigger system. DELPHI had four levels of the trigger denoted L1-L4. Levels L1 and L2 were synchronous with the beam crossing time. L1 was based on the information from fast tracking detectors ID, OD, FCA and FCB, barrel muon chambers, FEMC, STIC and scintillators TOF and HOF. Its decision time was $3.9\mu s$. For the second-level trigger more thorough information from the L1 detectors was available together with the signals from TPC and HPC. L2 decision occurred $39\mu s$ after BCO. Trigger levels T3 and T4 were software filters. The reduction was from the BCO at the frequency 90kHz in the setup of 8x8 equidistant bunches of electrons and positrons to about 1Hz after the L3. L4 was used to tag some background events.

Positive trigger output resulted in complete event read-out and its archivation on tape. So called raw data were later processed by DELPHI analysis software DELANA.

### 4.2.6 Luminosity measurement

Bhabha scattering was used to determine luminosity corresponding to the collected data. It is both theoretically well understood and the process provides enough statistics to be a reference process for a precise luminosity measurement. VSAT and STIC were used in luminosity analysis. The error of the luminosity measurement was about 0.1%.

# Chapter 5

# Monte Carlo simulation

This chapter deals with the description of Monte Carlo event generators used for the simulation of the physical processes. Leading-order event generators HERWIG and PYTHIA are introduced and their features important for the dijet production in $\gamma\gamma$ collisions are shortly reviewed. Simulation of the response of the DELPHI detector and the event reconstruction program are also discussed.

## 5.1 Event generators

### 5.1.1 HERWIG

HERWIG is a general purpose Monte Carlo event generator for hard collisions with emphasis on parton shower development [30]. It implements binary hard scattering processes in two-photon collisions which makes the most important contribution to the dijet production. The direct, single-resolved and double resolved interactions are simulated as separate processes. User of the program is responsible for proper mixing of events from different processes. Version 5.9 of HERWIG was used in this analysis.

HERWIG generates a $\gamma\gamma$ event in a sequence of steps:

- First the hard scattering of partons (in resolved channels) or photons (in direct channel) is generated according to the formula 2.13. In this step the partons are taken on mass-shell.
- Then the parton showers are added to both the initial and final state partons, taking correctly into account the kinematics of parton branching.
- After ending the parton showering gluons are forcibly split into quark-antiquark pairs.
- Resulting set of quarks and antiquarks are combined to colourless clusters using the concept of colour connection.

- These clusters are allowed to decay using basically the phase space arguments. If some cluster is too heavy it is first split into two lighter clusters. There are parameters governing this non-perturbative cluster splitting which we left to their default values.

HERWIG uses a limited set of internal PDFs but can also be linked to PDFLIB [31].

HERWIG has an option to accompany double-resolved photon interaction with soft underlying event as discussed in 2.3. Its generation is controlled by two parameters called PRSOF and ENSOF. PRSOF determines the fraction of events to be accompanied with soft underlying event while ENSOF represents which fraction of the remnants energy should be used in the interaction. The value of PRSOF was adjusted in a way described in section 6.2.1. For clarity of meaning the value of PRSOF is denoted by SUE in the plots. The second parameter ENSOF was fixed to its default value of 1.

### 5.1.2 PYTHIA

PYTHIA 6.143 is another multi purpose event generator. Its detailed description is given in [32]. Similarly to HERWIG it provides a Monte-Carlo model for high-$p_T$ jet production in $\gamma\gamma$ collisions. PYTHIA automatically generates mixture of possible interaction types with correct weights. Apart from the hard 2-2 parton scattering also soft scattering processes are generated.

Processes involving photons are divided into two classes

- Direct photon - photon interacts as a whole through its electromagnetic interaction.
- Resolved photon - photon interacts through its coupling to a $q\overline{q}$ pair. Two kinds of events are distinguished
  - Vector meson dominance (VMD) events

    The photon fluctuates into a vector meson and it is further treated as a hadronic process. The model includes elastic and diffractive scattering, low-$p_T$ and high-$p_T$ jet production.
  - Generalised vector meson dominance (GVMD, also called anomalous) events

    If the virtuality of the $q\overline{q}$ pair is sufficiently large, the process is perturbatively calculable and both the initial parton distribution and the evolution of the parton shower can be determined. High-$p_T$ events are produced in anomalous process.

As far as the simulation of large-$p_T$ jets is concerned PYTHIA uses basically the same framework, outlined in Chapter 2, as HERWIG. PYTHIA uses internal implementation of the SaS sets of the PDF as it distinguishes between the hadronic (VMD) and point-like (anomalous) part. This subdivision is not available to a user of PDFLIB library.

PYTHIA uses a different hadronization model than HERWIG. Fragmentation is done within the Lund string model. The string fragmentation incorporates the idea that the force

between two colour charges is linearly increasing with their distance. If the partons are sufficiently distant the string may break into $q\overline{q}$ pairs and two new strings appear. This proceeds iteratively until the energy in the rest frame of the short strings is close to masses of known hadrons.

Multiple parton interaction is used as default with $p_T^{mi} = 1.4$ GeV. It defines a $p_T$ cutoff for generation of additional binary processes.

### 5.1.3 Comparison of Monte Carlo event generators

In this section the description of the Monte Carlo event generators is complemented by several plots comparing them on the hadron level. The distributions of the invariant mass $W$, fractions of photon momenta $x_{1,2}$, absolute values of jet pseudorapidities $|\eta_{1,2}|$ and of the $E_{T_1}$ of the leading jet are shown for dijet events in Fig. 5.1. PYTHIA SaS 1D and HERWIG SUE=0.2 predict about the same cross section, PYTHIA SaS 2D distributions has 10% more events. In agreement with Fig. 2.6, where the same PDFs were used in HERWIG, the PYTHIA SaS 1D sample yields the smallest slope of $d\sigma/dE_{T_1}$ while HERWIG SUE=0.2 with GRV predicts the largest. Similar behaviour can be found also in the distribution of $x_{1,2}$ - the sample with SaS 1D generates less events for small $x$ (where resolved photon dominates) than GRV and SaS 2D and more events with $x$ close to 1. PYTHIA SaS 1D sample has more events with $W < 30$ GeV than PYTHIA SaS 2D and HERWIG SUE=0.2 whose distributions have longer tail. The distributions of $|\eta_{1,2}|$ are similar for all three samples.

## 5.2 Simulation of the DELPHI detector

In order to compare measured data with the prediction of Monte Carlo models the behaviour of the detector has to be accounted for. Monte Carlo events generated by PYTHIA and HERWIG were further processed by two programs - DELSIM which is the full simulation of the DELPHI detector and DELANA which is the event analysis program of the DELPHI collaboration.

#### DELSIM

DELSIM [33] simulates response of the DELPHI detector to a generated physics process. Its output is a collection of signals in the form of so called Raw Data which is the same as in DELPHI data taking. Thus the simulated events can be further analysed with the DELPHI event reconstruction program DELANA to interpret the recorded interaction in terms of particle tracks, showers and even identified particles. DELSIM can either invoke one of the built-in event generators for the generation of the physics process or it can process output of external event generators. The latter option was used. DELSIM simulates passage of particles through DELPHI. The detailed knowledge of DELPHI geometry, magnetic field

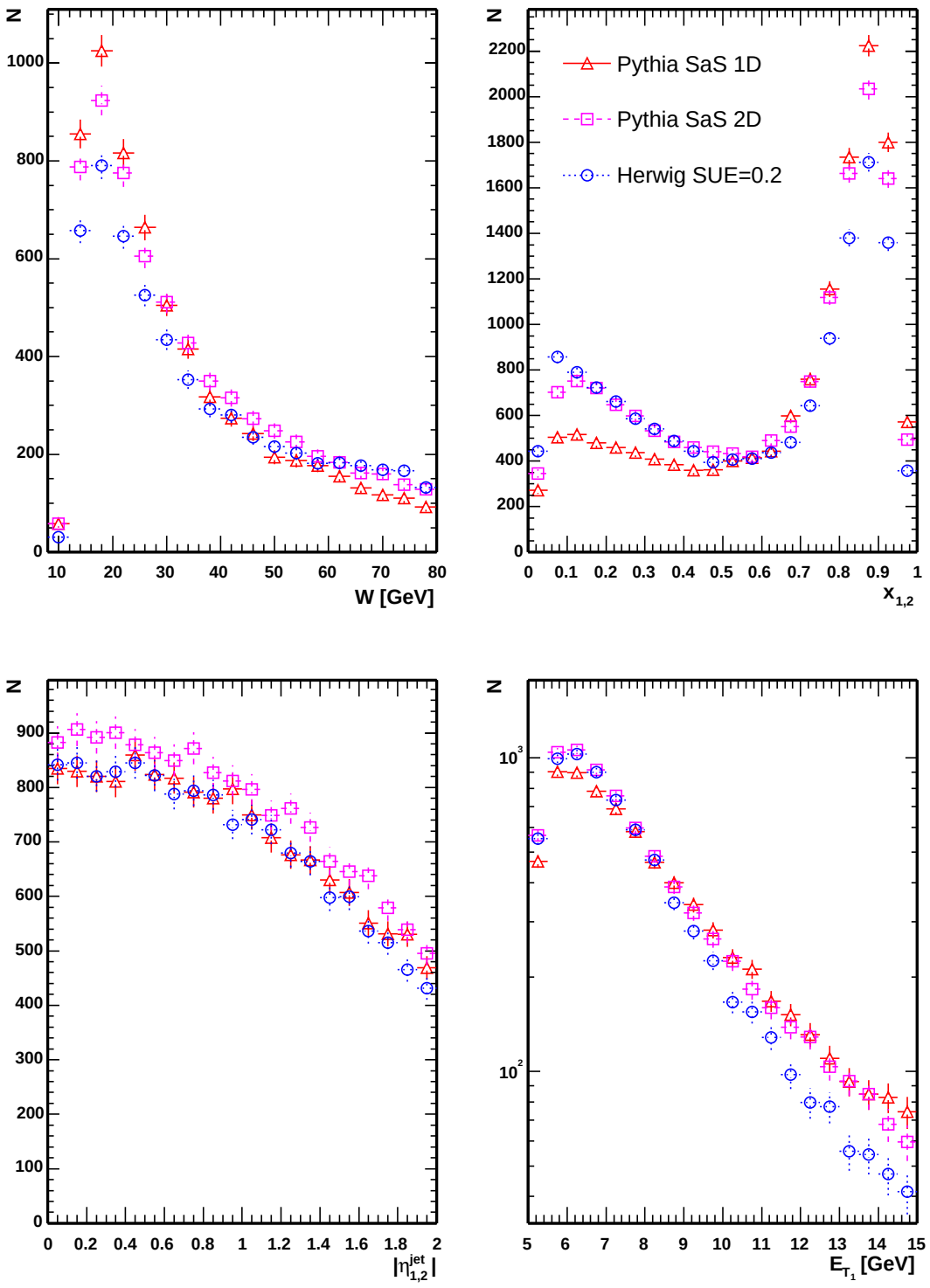


Figure 5.1: The distributions at the hadron-level of the invariant mass of the hadronic system $W$ (a), fractions of the photon momenta $x_{1,2}$ (b), absolute value of jet pseudorapidities $|\eta^{1,2}|$ (c) and $E_{T_1}$ of the leading jet (d). Events with $E_{T_{1,2}} > 5$ GeV and $|\eta_{1,2}| < 2$ are shown for PYTHIA with SaS 1D (solid line), SaS 2D PDF (dashed) and HERWIG SUE=0.2.

and materials in the detector is taken into account. The following processes are included in the simulation of passage of particles through matter - multiple scattering, energy loss along the trajectory, pair conversion, bremsstrahlung, annihilation of positrons, delta rays, photoelectric effect, interactions with nuclei, decays of unstable particles. At the end of event simulation the detector signals are stored in the Raw data format.

**DELANA**

DELANA [34] is the official event reconstruction program. It proceeds in the following steps:

- Track elements within single subdetectors are searched.
- Track hypothesis is done within a subdetector not considering other subdetectors.
- An extrapolation of tracks from one detector (mainly from the TPC) to others is carried out. New fit of the track parameters is done and track hypothesis is correlated with calorimeter showers.
- Tracks are used to fit the position of vertex.
- Identification of particles is done with the help of RICH detectors, $dE/dx$, calorimeter and muon chambers signals.

## 5.3 Details on Monte Carlo samples

Monte Carlo samples generated by HERWIG and PYTHIA were processed by the detector simulation program DELSIM [33] for simulation of the detector response. As the detector simulation is a CPU intensive task, an attempt has been made to reduce the number of simulated events and skip those which would hardly pass the selection criteria for analysis as listed in Section 6.1.

The following three Monte Carlo samples were employed in the analysis.

1. HERWIG 5.9 GRV

   This sample is a dedicated sample for the purpose of this analysis. It was simulated in Prague with the standard simulation tools. A special care was taken to keep all the simulation history including the information on the hard parton process. For this reason some studies were possible only with this sample as the complete simulation history was not retained for PYTHIA samples introduced below. The list of most important HERWIG parameters[1] set in this work

[1]The rest of the parameters were left to their default values

- PDF: GRV G LO[2]
- The centre-of-mass energy of the colliding electrons and positrons was set to $\sqrt{s_{ee}} = 196$ GeV. This slightly differs from the luminosity-weighted average for the data collected in 1999. The sample was prepared before 1999 when the beam energies were unknown.
- $p_{\perp}^{min} = 3$ GeV (corresponding to the HERWIG parameter PTMIN) minimum $p_T$ of outgoing partons in the hard scattering. It is discussed below.
- The spectrum of generated photon virtualities was limited to $Q^2 < 10$ GeV$^2$ by setting Q2WWMX=10. Above 10 GeV$^2$ the scattered electron beam should be well detected with the electromagnetic calorimeters. Events with smaller photon virtualities may remain untagged. $Q^2$ distribution of the selected Monte Carlo events is shown in Fig. 6.3.
- Standard version of the generator implements $\alpha_s$ evaluation in NLO. This is appropriate for example for the simulation of deep inelastic scattering. For the purpose of this study the generator code was modified to calculate $\alpha_s$ in LO.

Concerning the parameter $p_{\perp}^{min}$ it should be chosen small with respect to the $E_T$ of the jets in order to generate complete sample of two jet events. On the other hand too small values of $p_{\perp}^{min}$ are outside of the region where perturbative QCD is applicable. The distribution of $p_T$ of outgoing partons is shown in Fig. 5.2. Three test Monte Carlo samples were generated with $p_{\perp}^{min} = 3$ GeV and SUE=20% and $p_{\perp}^{min} = 2$ GeV (SUE=20% and with no SUE component). $p_T$ of the partons is shown for events with two or more jets. There is about 20% more events contributing to two-jet cross section in the $p_{\perp}^{min} = 2$ GeV SUE=20% sample compared with the $p_{\perp}^{min} = 3$ GeV SUE=20% sample which was chosen for this thesis. It reflects the fact that HERWIG employs hard process cross sections which diverge for $p_{\perp}^{min} \to 0$ and can not thus be used for studies of the total cross section.[3] The question of choosing an optimal value of the $p_{\perp}^{min}$ cut is discussed in [35].

Out of the generated sample only the events satisfying:

- sum of the $p_T$ of the final state particles on the hadron level $\sum p_T > 8$ GeV
- there is at least one jet found on the hadron level $n_{jets} \geq 1$

were processed with the detector simulation. The probability that genuine dijet events will not satisfy these conditions is very small as documented in Fig. 5.3 obtained with a smaller sample of unbiased simulation.

The sample corresponds to 1000 pb$^{-1}$.

[2]This PDF is denoted as GRV G LO 3-5-3 set in the PDFLIB.
[3]PYTHIA cross section is regularised for low $p_T$.

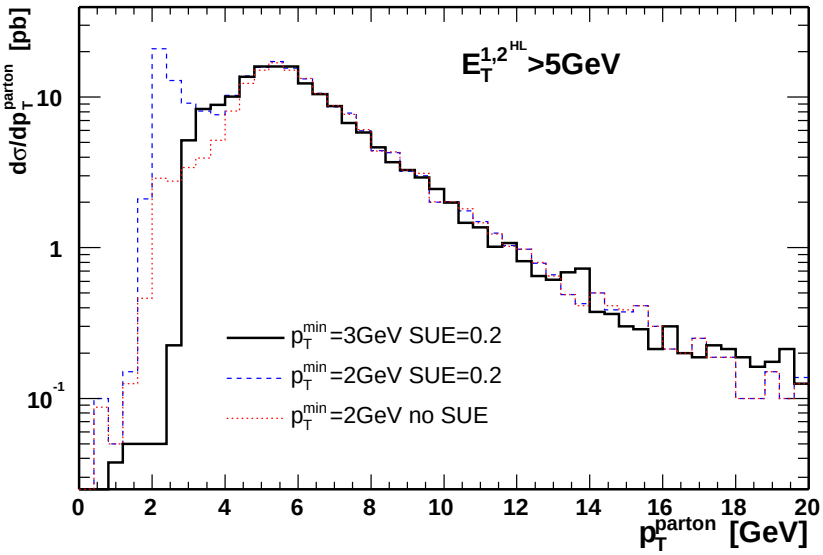


Figure 5.2: Distribution of the parton $p_T$ in the $\gamma\gamma$ CMS for events with 2 or more jets found on the hadron level. The contribution of events with $p_\perp^{min} < 3$ GeV to dijet events with $E_T^{HL} > 5$ GeV is not negligible for sample with simulation of soft underlying event (dashed line) and it is about 20%.

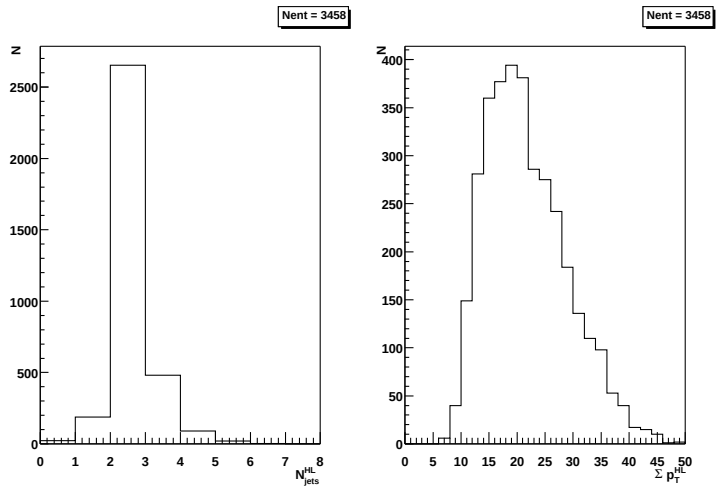


Figure 5.3: The distributions of the hadron-level variables $n_{jets}$ and $\sum p_T$ for MC events which are seen as dijet events on the detector level. It was studied on a smaller unbiased sample of events.

2. PYTHIA 6.143 SaS 1D

   This sample is a general purpose simulation sample used within DELPHI collaboration. The PDF set of the photon is SaS 1D. All PYTHIA parameters were left to its default values. The event selection is quite loose

   - $E_T^{vis} > 3$ GeV and at least 3 charged tracks with momentum $p > 0.1$ GeV
   - or one particle (tagged electron) with $E > 0.4\ E_{beam}$

   The sample has an equivalent luminosity of 550 $\text{pb}^{-1}$.

3. PYTHIA 6.143 SaS 2D

   This sample was generated as an official Monte Carlo sample at CERN mainly upon the request of this study. The PDF set of the photon is SaS 2D. Apart from the PDF choice the parameters of PYTHIA are set to the default values. The selection of events is dedicated for jet physics in $\gamma\gamma$. It was generated at CMS energy 199.5 GeV with the following cuts

   - invariant mass of the $\gamma\gamma$ final state $W_{\gamma\gamma} > 6$ GeV
   - at least one jet $E_T > 3$ GeV found by PXCONE jet algorithm.

   This sample was produced for this analysis to have a comparison between two PDFs within the same generator. The sample has an equivalent luminosity of 1000$\text{pb}^{-1}$.

# Chapter 6

# Analysis

The present analysis was done on the 1999 data. The total integrated luminosity of 219.4 $\text{pb}^{-1}$ was collected at four different beam energies. Most data were recorded at 196 GeV and 200 GeV (about 80 $\text{pb}^{-1}$ each) with additional 25 $\text{pb}^{-1}$ (35 $\text{pb}^{-1}$) at 192 GeV (202 GeV). For the list of DELPHI runs satisfying requirements on the quality of the detector operation the partial luminosities were summed.

Data recorded at the four beam energies listed above were analysed together for the purpose of this study. The systematic error originating from neglecting the energy dependence of dijet cross section is small as shown in Fig. 6.1 where the dijet cross section is plotted as a function of $e^+e^-$ CMS energy. The cross section for dijet production varies by about 2% from the luminosity-weighted average of the beam energies (198 GeV) to the end-points at 192 GeV and 202 GeV.

## 6.1 Event selection

The following criteria were applied for event selection.

- At least 5 tracks were required in the region of polar angle $25^\circ < \theta < 155^\circ$. The requirements on the track quality were
  - $p_T > 100$ MeV
  - track length at least 30 cm
  - impact parameters less than 4 cm (10 cm) in $R\phi$ ($z$) respectively
  - a measurement error $\Delta p/p < 1$

  These are common requirements on the track quality for QCD studies at DELPHI. The request for 5 or more tracks reduces background of lepton-pair production in two photon collisions (in particular $\gamma\gamma \to \tau^+\tau^-$).

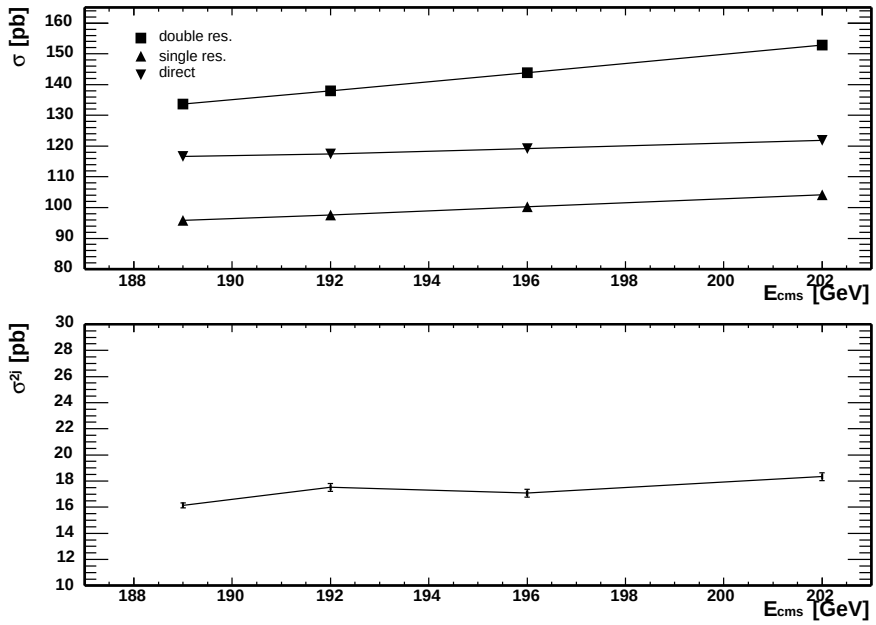


Figure 6.1: The $\gamma\gamma$ cross section as a function of the energy available in the $e^+e^-$ centre-of-mass system. In the upper plot three curves are shown for the cross section of double-resolved, single-resolved and direct process with $p_\perp^{min} = 3$ GeV. The lower plot shows the cross section for the dijet production with $E_{T_{1,2}} > 5$ GeV and $|\eta_{1,2}| < 1.5$.

- For calorimeter clusters thresholds were set to 0.3 GeV in HPC and STIC, 0.4 GeV in FEMC and 1.5 GeV in HCAL.
- In order to suppress the background from pair production of $W^+W^-$, ZZ or in s-channel interaction with $Z/\gamma$, the total $p_T$ in the event was demanded to satisfy $\sum p_T < 30$ GeV.
- Missing $p_T$ was required to be less than 5 GeV as interactions of almost real photons were expected to be well balanced in $p_T$.
- Photon virtuality was constrained by anti-tagging condition on scattered electron (positron). Events with high energy track or cluster ($E > 30$ GeV) were rejected.
- The number of reconstructed jets was required $n_j \geq 2$. The jet search program PXCONE was used with the following parameters
  - $R_{cone}$=1.
  - OVLIM=0.75
  - minimum jet transverse energy $E_T > 4$ GeV.
- Both jets had to be reconstructed in the central region[1] of the detector $|\eta_1| < 2$ and $|\eta_2| < 2$ and have $E_T < 15$ GeV.

The expected amount of background events in the selected data sample is illustrated by Fig. 6.2. The contamination by background processes is small (2%), except for very large $E_T$, and its distribution is flat.

Efficiency of the trigger for the channel under study was estimated using compiled data[2] on trigger efficiency for a single track in different angular and momentum ranges [36]. For each track in the event the efficiency of the trigger in the particular angular and momentum range was looked up and a random number was generated by uniform distribution between 0 and 1. If the random number was lower then the tabulated trigger efficiency for at least one track in the event the event was considered as accepted. The trigger efficiency for this analysis is given by the ratio of accepted events to the total number of events which is equal to 99.1%. The efficiency close to 100% is in accord with the expectation that hadronic events with multiple tracks are well triggered by DELPHI. The trigger inefficiency is thus small and negligible source of error in this analysis.

The distribution of the virtualities of interacting photons in data is inferred from the Monte Carlo simulations as it cannot be measured due to the anti-tagging condition. Photon virtualities $Q^2$ are shown for PYTHIA SaS 1D and HERWIG in Fig. 6.3. Mean virtuality of the photon in selected Monte Carlo events was found to be $< Q^2 >= 0.3$ GeV$^2$ with median of $3 \times 10^{-4}$ GeV$^2$.

[1] In certain parts of the analysis stricter cuts on $|\eta|$ of the jets were adopted. This is properly noted in the text.

[2] The parametrisation of the single track efficiencies was provided by Valeri Pozdniakov.

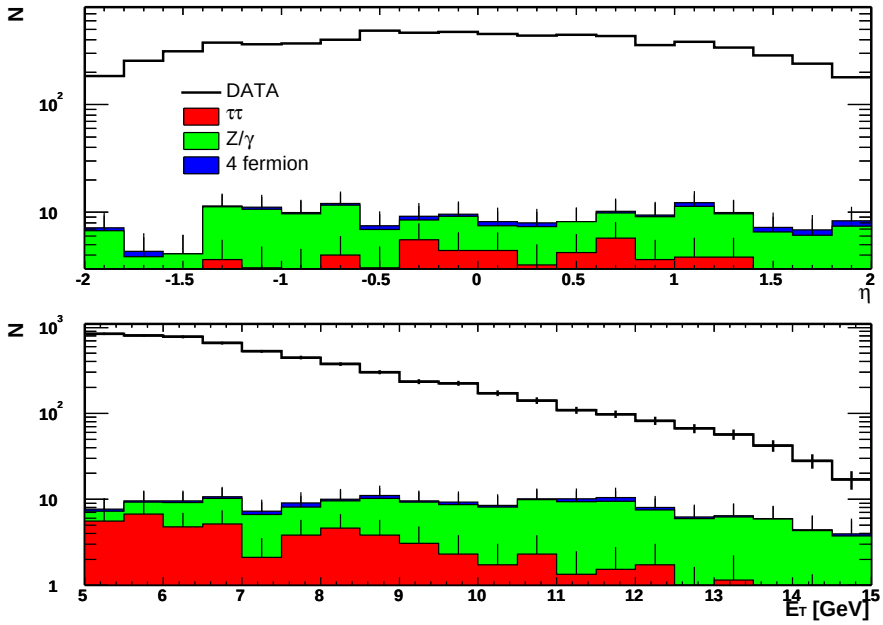


Figure 6.2: The data distributions of $E_T$ and $\eta$ are presented together with the cumulative contributions of background processes in the selected sample of events. The background from $\gamma\gamma \to \tau\tau$, s-channel interaction via Z/$\gamma$ and 4-fermion production ($e^+e^- \to W^+W^-$, $e^+e^- \to ZZ$) is shown.

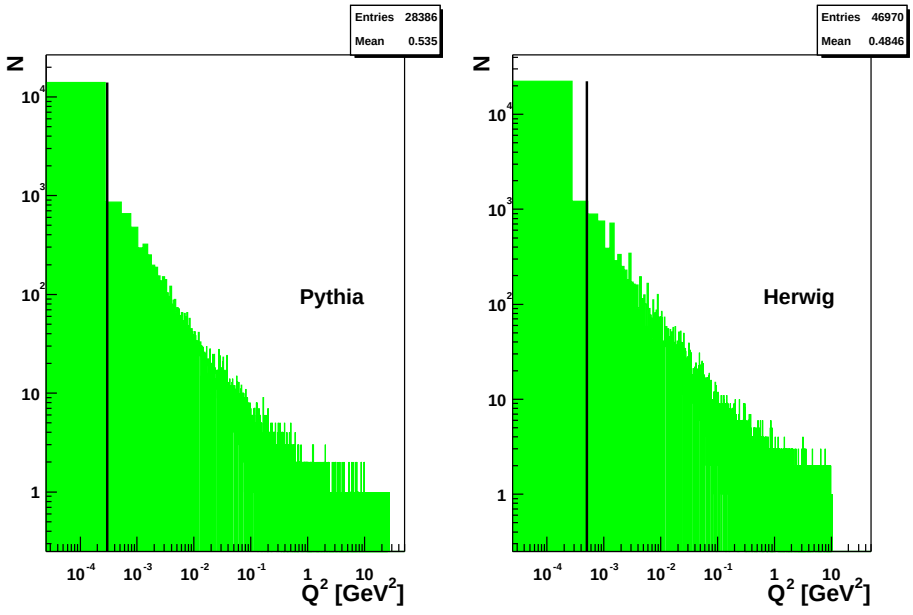


Figure 6.3: Photon virtuality in Monte Carlo samples for selected events.

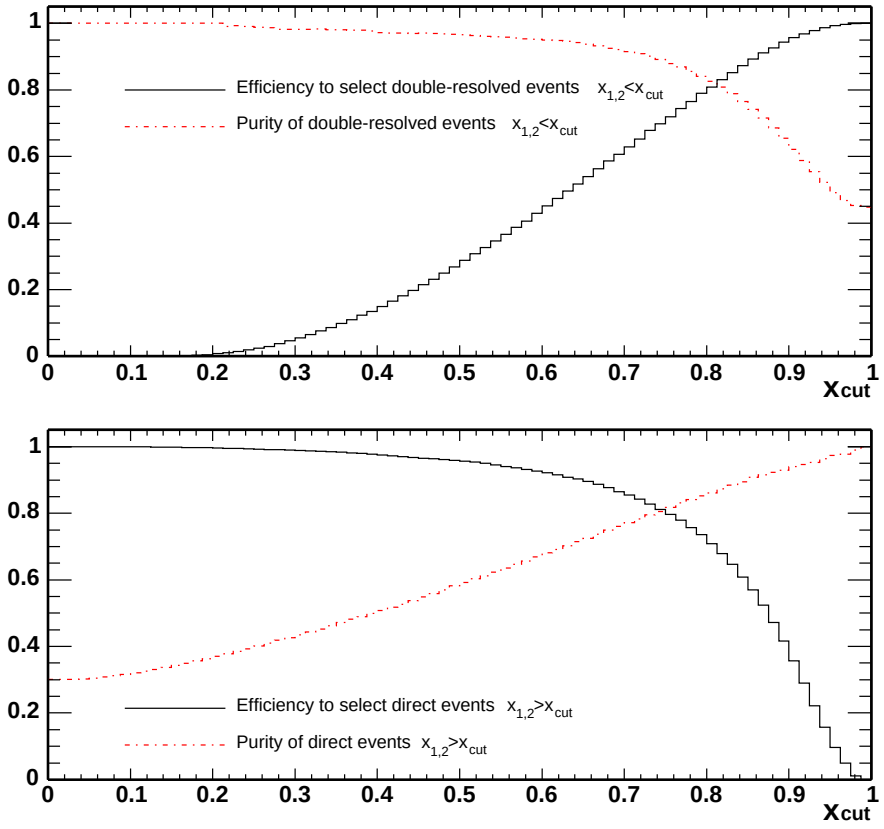


Figure 6.4: Purity and efficiency of the separation of direct (double-resolved) events by means of cuts $x_1 > x_{cut}$ and $x_2 > x_{cut}$ ($x_1 < x_{cut}$ and $x_2 < x_{cut}$) respectively, calculated with HERWIG SUE=0.2.

In the following we shall need separately the individual contributions of double-resolved, single-resolved and direct interactions. In an experiment this is usually done by imposing cuts on energy fractions (2.15) calculated at the detector level. The plots in Fig. 6.4 quantify the efficiency and purity of these cuts to select double-resolved and direct contribution. As a single cut variable $x_{cut}$ is not efficient to select single-resolved events thus it is not shown in this plot. Based on this plot we have decided to define operationally the double-resolved contribution by means of cuts

$$x_1 < 0.7, \; x_2 < 0.7 \tag{6.1}$$

and direct process by

$$x_1 > 0.8, \; x_2 > 0.8 \tag{6.2}$$

As an illustration of their relative importance, the direct, single-resolved and double-resolved contributions to dijet cross section as a function of $E_T$ are shown in Fig. 6.5. We

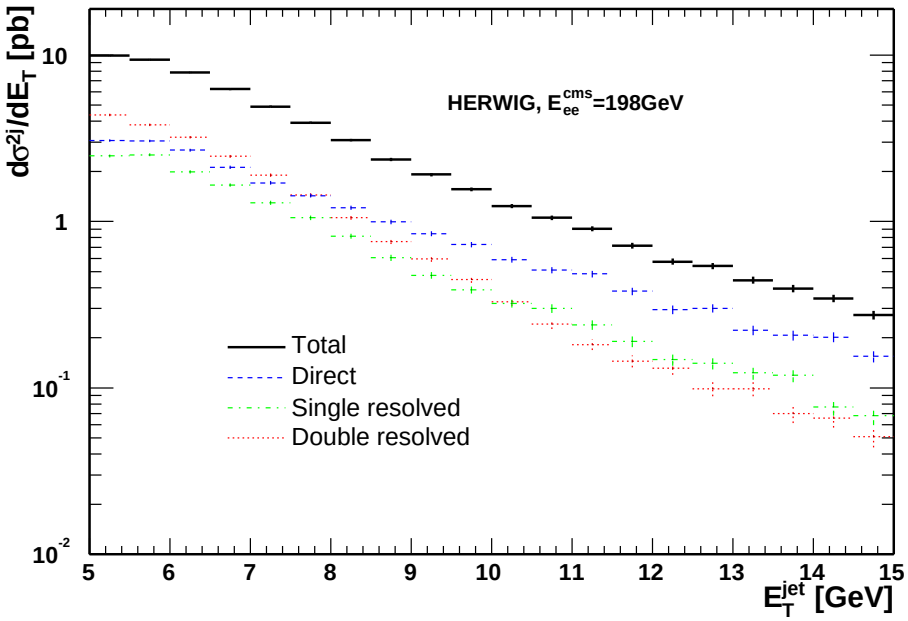


Figure 6.5: Dijet cross section at $E_{ee}^{CMS} = 198$ GeV on the generator level. The total cross section (solid) as predicted by HERWIG is shown together with contributions of direct (dashed), single resolved (dash-dotted) and double resolved (dotted).

see that the direct photon contribution dominates at large $E_T$, whereas the double-resolved photon dominates at small $E_T$, but drops fast in relevance with increasing $E_T$.

## 6.2 Comparison of Monte Carlo generators with data

In this section the data on the detector level will be compared with Monte Carlo event generators PYTHIA and HERWIG using samples defined in section 5.3.

Soft particles accompanying the hard two-photon collisions are studied first. The intention is to tune Monte Carlo generators using the transverse energy activity outside the jets.

As it is important to check that the event generators which are later used for the determination of the differential cross sections have reasonable description of data, also the various characteristics of jets and of the dijet final state are compared with HERWIG and PYTHIA predictions.

### 6.2.1 Soft particles in hard $\gamma\gamma$ collisions

An important part of the comparison between Monte Carlo generators and data is the description of the transverse energy flow in an event because the reconstruction of jets is influenced by soft physics phenomena. Photon remnants in the double-resolved process can interact and particles from their interaction populate the central region of the detector. These particles cannot be distinguished from the products of the hard scattering and systematically increase $E_T$ of the jets. They also modify the correlation between jets reconstructed in the event and partons produced in the hard subprocess. Monte Carlo generators describe these additional soft particles by means of multiple parton interaction (PYTHIA) and soft underlying event (HERWIG), shortly described in section 2.3. Both models and their parameters used in the event generation are described in Chapter 5. Monte Carlo samples denoted PYTHIA SaS 1D, PYTHIA SaS 2D, HERWIG SUE=0, HERWIG SUE=0.2 and HERWIG SUE=0.3 were compared with data.

Transverse activity in the events was investigated in jet profiles and in mean transverse energy flow outside the jets.

#### Jet profiles

Jet profiles are calculated from 2-dimensional distributions of transverse energy flow in the area surrounding the jet axis. For each of the two leading jets in the event the transverse energy flow as a function of the distance $\Delta\phi$ and $\Delta\eta$ from the jet axis is determined. These values are summed for all events in the sample and normalised to the number of jets. Finally the mean values of transverse energy flow in the bands of $|\Delta\eta| < 1$ (or $|\Delta\phi| < \pi/2|$) are projected onto the $\phi$ (or $\eta$) axis. The errors are calculated by accumulating errors on the $E_T$ measurement of tracks.

The jet profiles are shown separately for events with $x_{1,2} < 0.7$ (Fig. 6.6) and $x_{1,2} > 0.8$ (Fig. 6.7). The effect of the soft underlying event is visible on so-called jet pedestals around $|\Delta\phi| = 1$. The shape of the jet profiles in the domain of direct process (Fig. 6.7) is well described by all Monte Carlo samples defined above while in the domain of double-resolved process the deficiency of HERWIG SUE=0 is obvious. This absence of the simulation of soft underlying event results in lower jet pedestals than in data and other Monte Carlo samples. The difference in the jet pedestals seen in the plot is equivalent to about 1 GeV shift in the transverse energy of the jet.

For two-photon events the opposite jet is seen in the $\Delta\phi$ distribution at $\Delta\phi = \pi$.

#### Energy flow outside the jet area

Another quantity characterising the activity outside the jets is the transverse energy flow. The transverse energy flow is defined as a sum of $E_T$ in the area $R > 1.2$ from the jet axes. Only tracks and clusters within $|\eta| < 1.5$ are taken into account. The sketch how the energy flow is calculated is shown in Fig. 6.8. Mean energy flow in bins of maximum ($x_{max}$) and

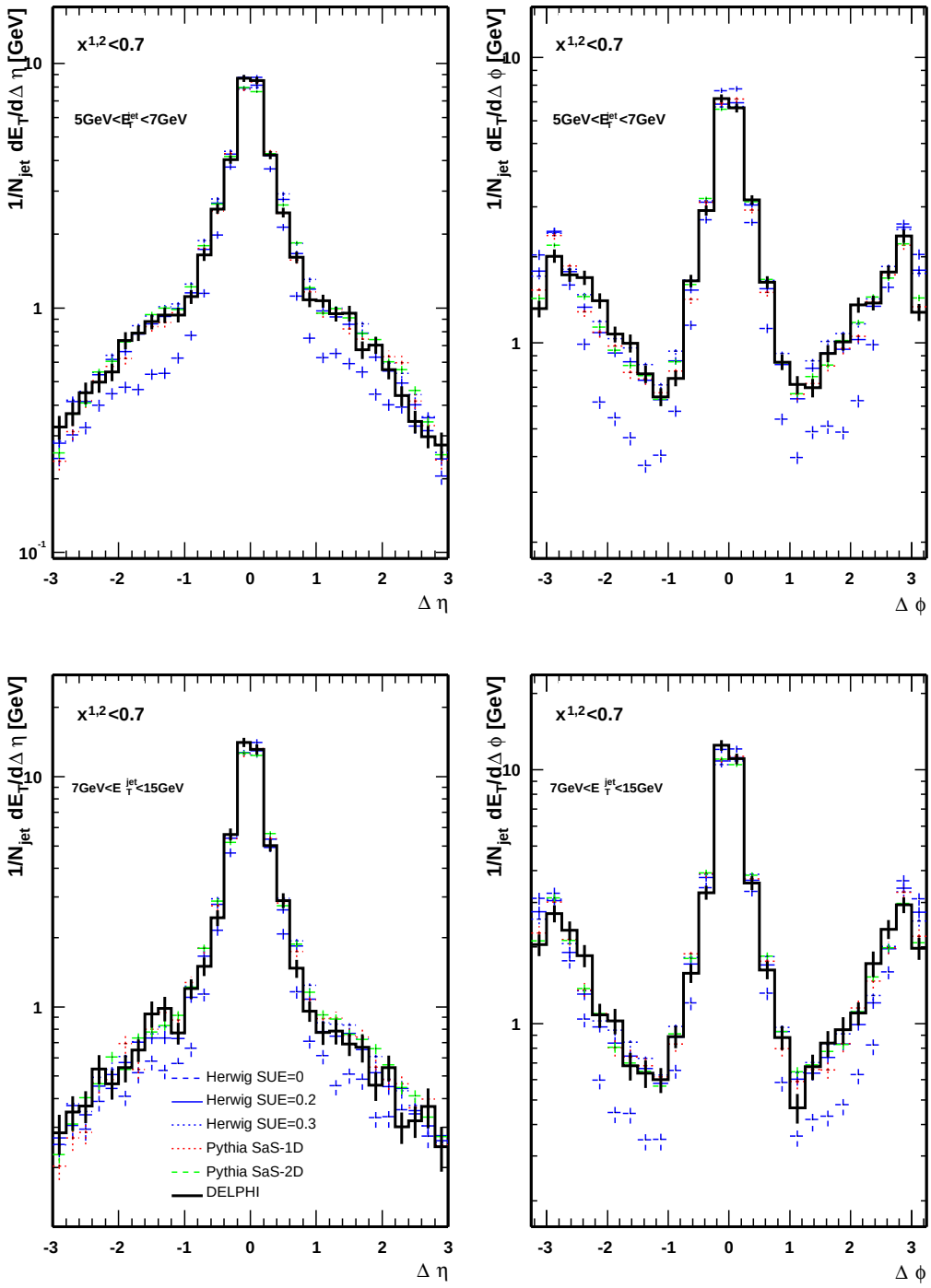


Figure 6.6: Jet profiles for events with $x_{1,2} < 0.7$. Most events in this region of $x$ are expected from double-resolved interaction. Data (solid) are plotted together with Monte Carlo generators PYTHIA (SaS 1D and SaS 2D) and HERWIG with different values of SUE. Jets in the central area of $|\eta| < 1$ and with $5 < E_T < 7$ (upper plots) and with $7 < E_T < 15$ (bottom plots) were analysed. The errors are track measurement errors.

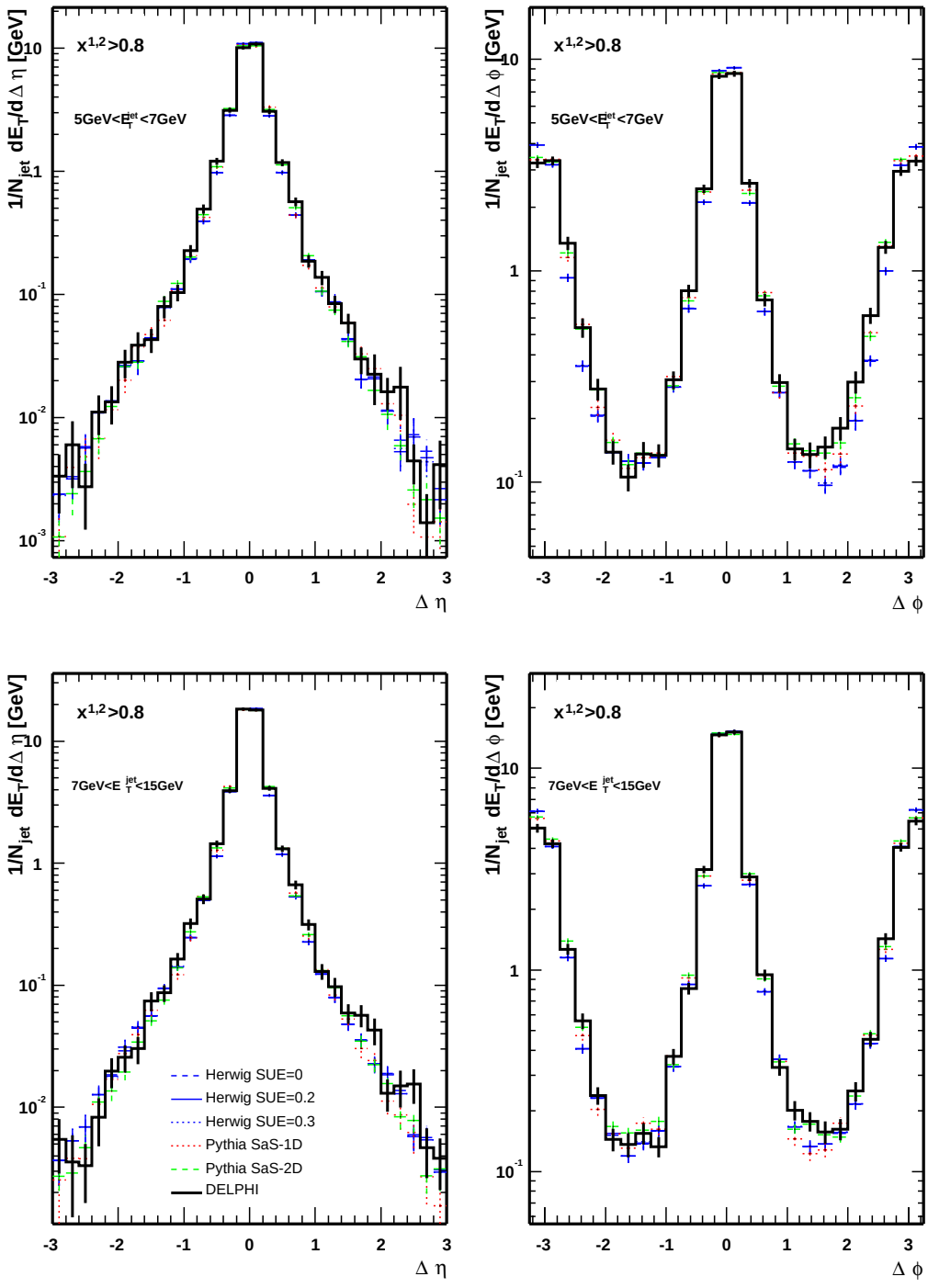


Figure 6.7: The same as in Fig. 6.6 but for $x_{1,2} > 0.8$.

minimum ($x_{min}$) values of $x$ reconstructed in the event is shown in Fig. 6.9. Lower values of $x_{max}$ imply that the event is likely a double-resolved interaction, similarly high values $x_{min}$ select direct events.

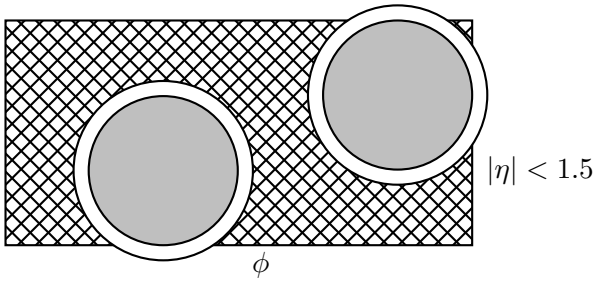


Figure 6.8: Energy flow outside the jets area. Transverse energy flow is calculated in the crosshatched area for $|\eta| < 1.5$ and $|\phi| < \pi$. Jets are shown as shadow circles surrounded by white area R $< 1.2$.

To summarise the observations on the transverse energy flow outside the jets:

- HERWIG with SUE=0.2 is closer to the data than the sample without SUE. Without the inclusion of SUE jet profiles are reproduced only for jets coming from the direct interaction. The simulation of SUE refines the description of jet profiles in particular for jets of double-resolved processes. On the basis of Fig. 6.6-6.9 the parameter SUE=0.2 was fixed for further studies. This sample will be denoted HERWIG GRV to conform the notation of PYTHIA samples.

- PYTHIA provides a very good model of the soft interaction accompanying the two-photon collision. Its default for multiple parton interaction is sufficient to describe the jet profiles and the energy flow outside of jets. The choice of the PDF of the photon (SaS 1D and SaS 2D) does not make a difference in these plots.

### 6.2.2 Event properties

Figures 6.10-6.13 show uncorrected distributions of the invariant mass $W$, the fractions of photon momenta $x_{1,2}$, the absolute value of jet pseudorapidities $|\eta_{1,2}|$ and the $E_T$ of the leading jet. The selection of events is done according to section 6.1. The distributions of these variables on the detector level are compared with normalised Monte Carlo predictions of PYTHIA and HERWIG. The distributions of Monte Carlo were multiplied by number 1.1 (PYTHIA SaS 1D), 0.9 (PYTHIA SaS 2D) and 1.4 (HERWIG SUE=0.2) so that their integral is the same as that of the data to focus on the differences between Monte Carlo and data in the shapes of the distributions. The discrepancy between the total number of events in some Monte Carlo sample and data is not important for further analysis as it has no effect on the normalisation of the unfolded result.

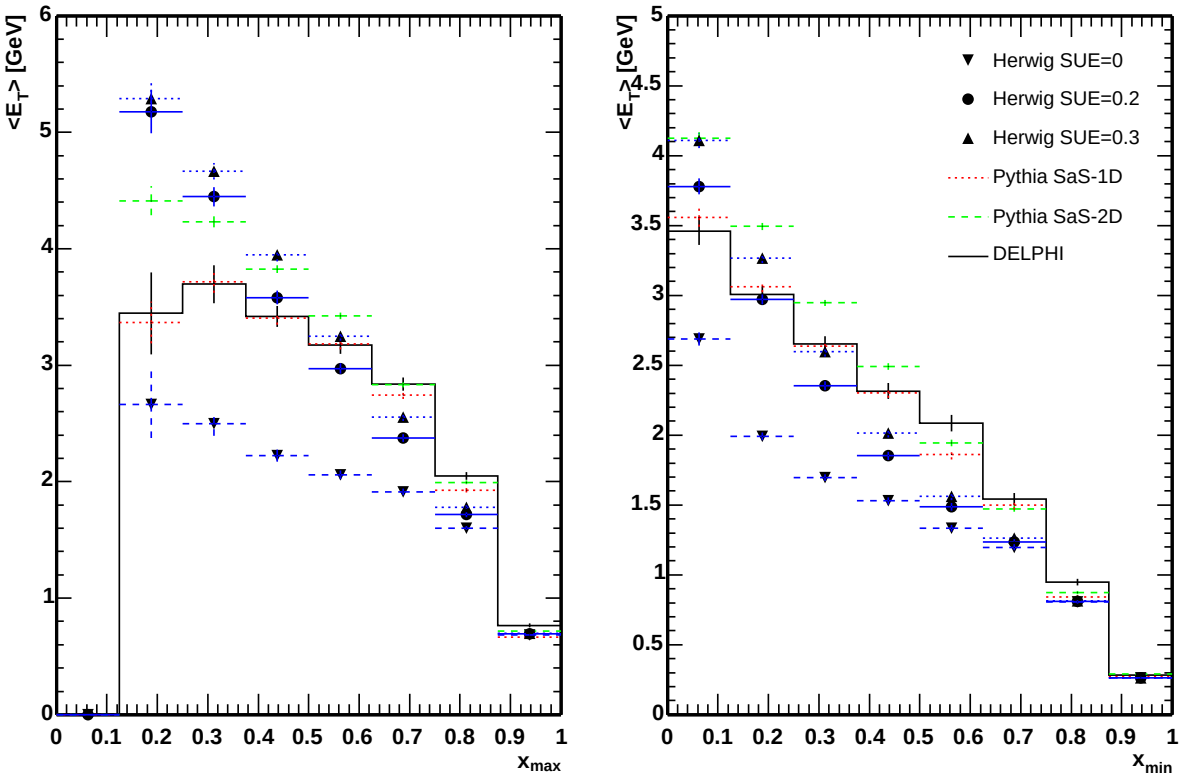


Figure 6.9: Mean transverse energy flow outside of jets on the detector level as a function of maximum (left plot) and minimum (right plot) $x$ reconstructed in the event. $< E_T >$ is a mean value of the total $E_T$ of tracks and clusters with $\Delta R > 1.2$ from the two leading jet axes and with $|\eta| < 1.5$. Only statistical errors are shown. The drop in the first bin of the left plot is due to limited statistics.

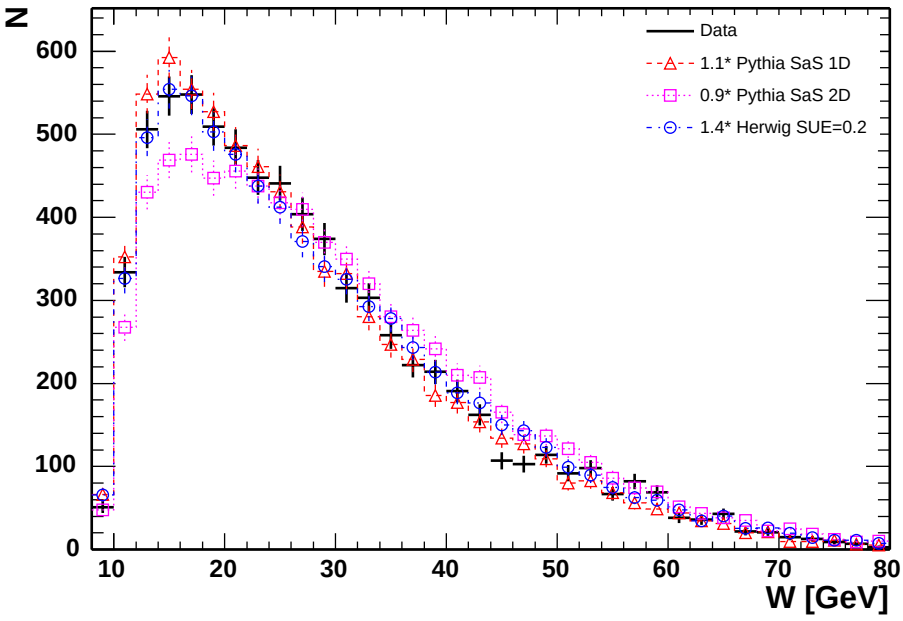


Figure 6.10: The visible invariant mass $W$ on the detector level for events with two or more jets with $E_T > 4$ GeV and $|\eta_{1,2} < 2|$. The error bars are statistical errors.

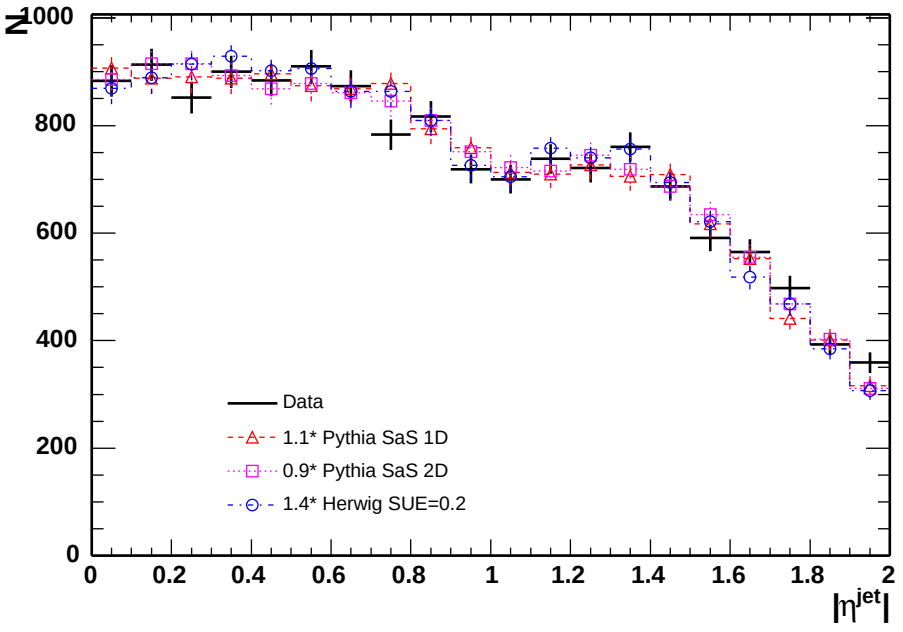


Figure 6.11: The uncorrected distribution of $dN/d|\eta_{1,2}|$. The statistical errors are shown.

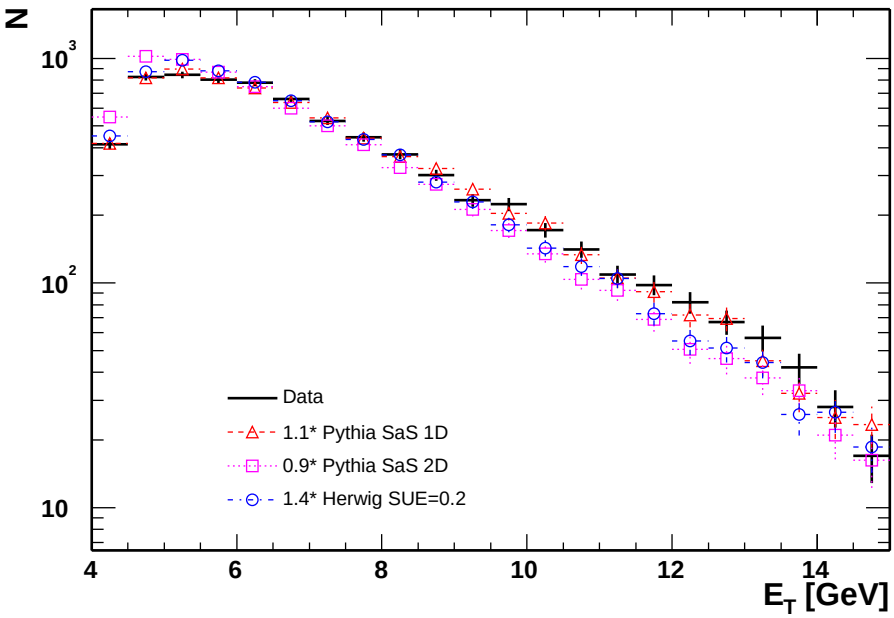


Figure 6.12: The uncorrected $dN/E_T$ of the leading jet. The error bars are statistical errors.

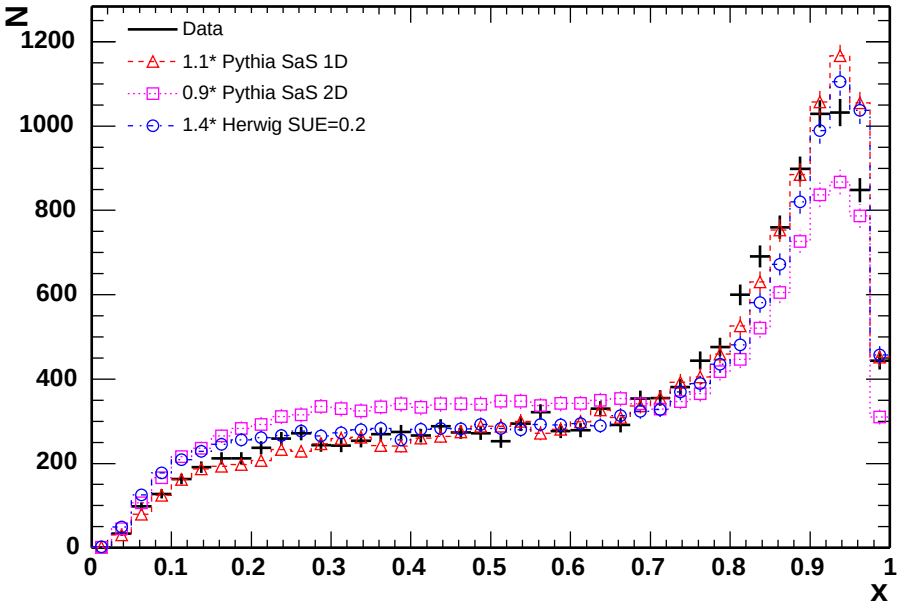


Figure 6.13: $dN/dx_{1,2}$ on the detector level. The statistical errors are shown.

In Fig. 6.14 the distribution of the multiplicity of charged particles for all selected events and separately for regions of $x$ where most events are expected from double-resolved process ($x_{1,2} < 0.7$), direct process ($x_{1,2} > 0.8$) and rest of events ($x_1 < 0.7$ and $x_2 > 0.8$ or $x_1 > 0.7$ and $x_2 < 0.8$) is presented.

Normalised samples of PYTHIA SaS 1D and HERWIG SUE=0.2 reproduce the shape of the $W$ distribution while PYTHIA SaS 2D has a lack of events for $W < 25$ GeV. All generators agree with data for jet pseudorapidities. The data distribution of $E_T$ is reproduced by PYTHIA SaS 1D, the slope is larger for PYTHIA SaS 2D and HERWIG SUE=0.2. PYTHIA SaS 2D generates more events in the region of $x_{1,2} < 0.7$ than are found in data. PYTHIA SaS 1D and HERWIG SUE=0.2 follow the data better.

Summarising the above comparisons we conclude that the best description of data is achieved with PYTHIA SaS 1D. HERWIG SUE=0.2 is close to the shape observed in data for distribution of $x_{1,2}$ and of charged multiplicity in the domains where double-resolved interactions are rare. Both HERWIG SUE=0.2 and PYTHIA SaS 2D have steeper distribution of the $E_T$ of the leading jet than the data. Significant departures from the data are observed with PYTHIA SaS 2D which has shortcomings in prediction of the distribution of the invariant mass, the fractions $x_{1,2}$ and the charged multiplicities. The exception is the distribution of $|\eta_{1,2}|$ where all Monte Carlo samples follow the data well.

### Jet shapes

Jet shapes quantify the internal structure of jets, i.e. how much of the jet transverse energy is contained within a cone of a smaller radius $r$ around the jet axis. They are usually described by the quantity

$$\psi(r) = \frac{1}{N_{jet}} \sum_{jet=1}^{N_{jet}} \frac{E_T(r)}{E_T(r = R)} \tag{6.3}$$

presented in Fig. 6.15 and 6.16. The jet shapes are compared in two intervals of $E_T$ of the jets (Fig. 6.15) and also separately for jets which are predominantly from double-resolved or direct interactions (Fig. 6.16). Beside the HERWIG SUE=0.2 sample also the samples without SUE and with SUE=0.3 are shown to demonstrate the effect of SUE on the shape of the jets. Jet shapes were studied in detail at HERA [37] and recently also at TEVATRON [39], this measurement is one of the first in two-photon collisions [24, 38].

Jet shapes were investigated in two regions of jet transverse energies $5 < E_{T_{1,2}} < 7$ GeV and $7 < E_{T_{1,2}} < 15$ GeV and also separately for jets which were predominantly double-resolved and direct. Measured jet shapes are shown together with all Monte Carlo samples including HERWIG samples without SUE and with SUE=0.3 to see the effect of SUE on jet shapes. As expected jets are narrower for higher $E_T$ (Fig. 6.15) than for lower $E_T$. PYTHIA (both SaS 1D and SaS 2D) reproduces jet shapes better than HERWIG. HERWIG SUE=0 yields the highest and HERWIG SUE=0.3 the lowest $\psi(r)$, which out of the HERWIG samples is the closest to the data. However better agreement between data and HERWIG

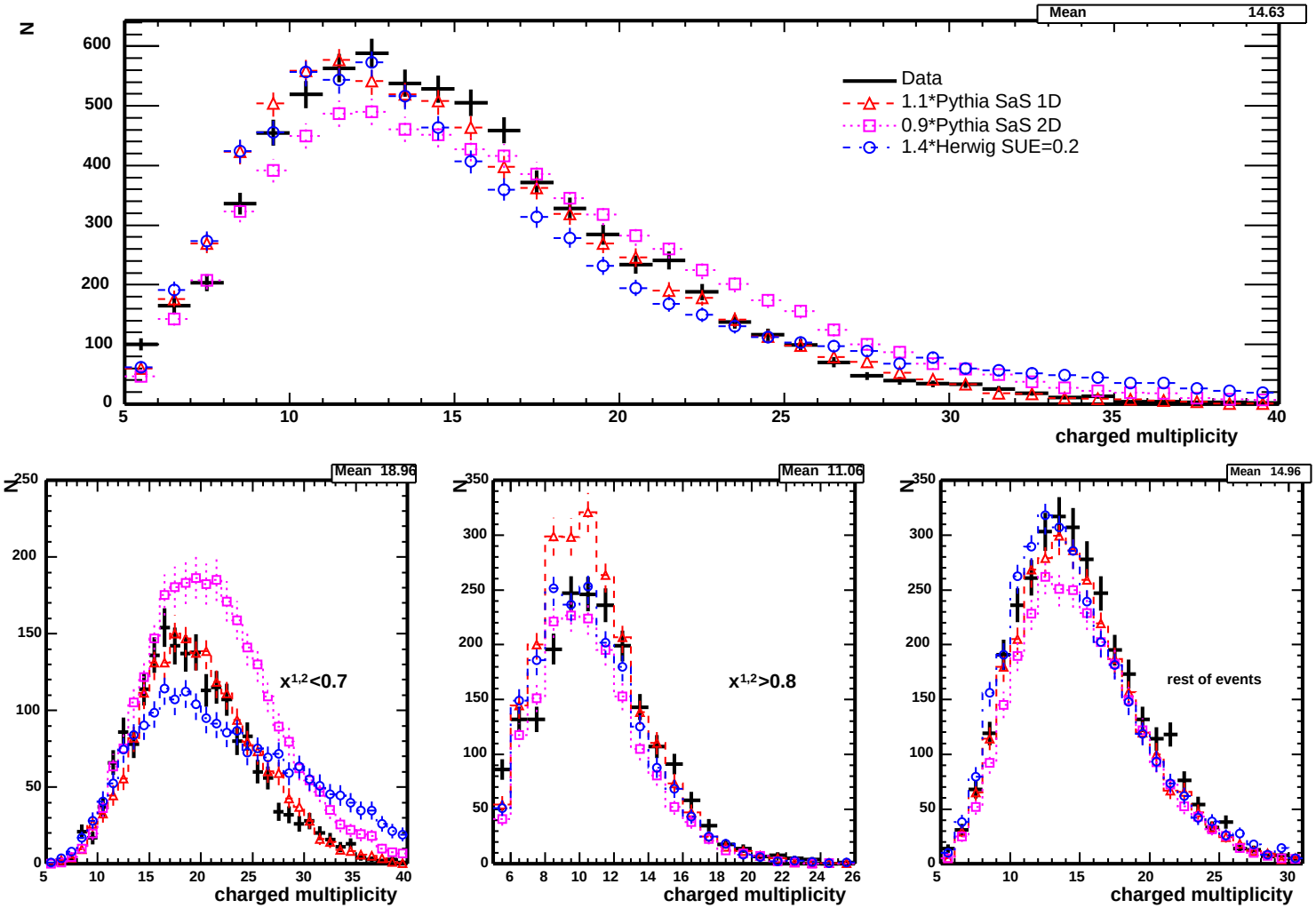


Figure 6.14: The distribution of the charged multiplicity on the detector level for all selected events (upper plot) and in regions $x_{1,2} < 0.7$ (left) $x_{1,2} > 0.8$ (middle) and the rest of the events in the last plot. The errors shown are statistical errors. Monte Carlo samples are not normalised to the data on plot-by-plot basis but the same multiplication factors as in the upper plot are also used for the plots in different regions of $x_{1,2}$.

SUE=0.3 in this plot is rather a coincidence as shown in Fig. 6.16 where $\psi(r)$ is plotted separately for $x_{1,2} < 0.7$ and $x_{1,2} > 0.8$. Different HERWIG samples as well as both PYTHIA samples are indistinguishable for $x_{1,2} > 0.8$, where PYTHIA reproduces the data whereas HERWIG is above the data. In the domain of $x_{1,2} < 0.7$ (where double-resolved events dominate) PYTHIA is close to the data (especially the sample with SaS 1D) while HERWIG jets are above (SUE=0) or below (SUE=0.3) the data. HERWIG SUE=0.2 is closest to the data in this region.

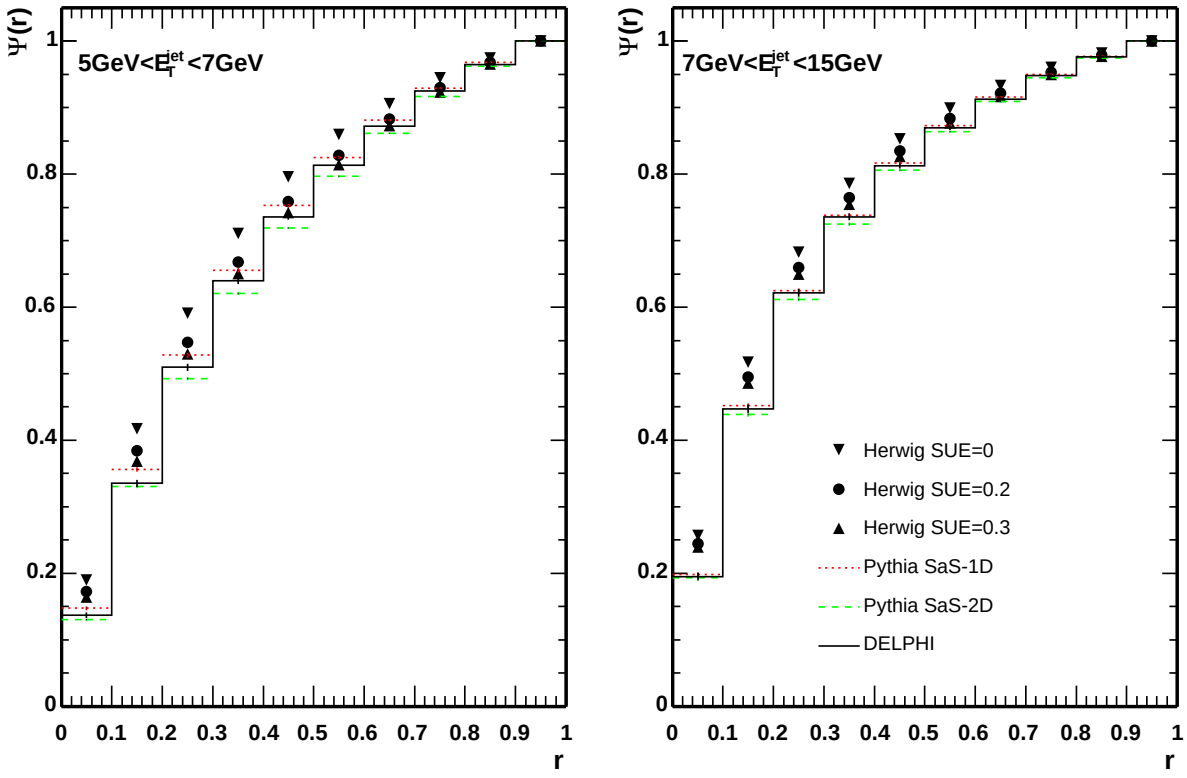


Figure 6.15: Uncorrected jet shapes. Comparison of jet shapes for data jets (solid) with Monte Carlo models PYTHIA and HERWIG for dijet events with $5 < E_{T_{1,2}} < 7$ GeV (left) and $7 < E_{T_{1,2}} < 15$ GeV (right). Statistical errors are shown.

## 6.3 Extraction of differential cross sections

The aim of this thesis is to present differential cross sections for dijet production corrected for detector effects. In this section the procedure is described in detail.

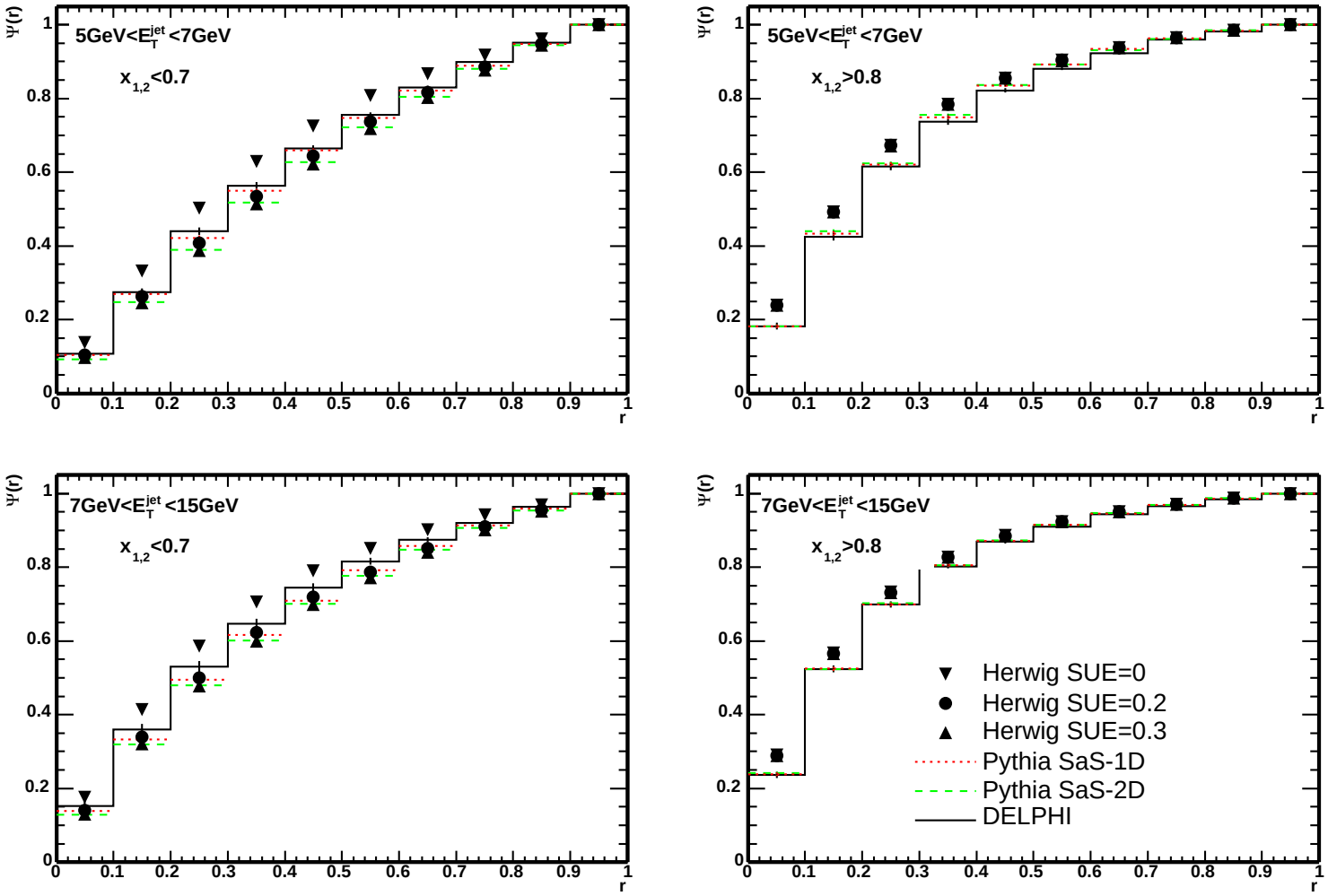


Figure 6.16: Uncorrected jet shapes. Jets shapes of data and of Monte Carlo are compared for events which are predominantly double-resolved (left) or direct (right) interaction. Upper plots are for low energy jets $5 < E_{T_{1,2}} < 7$ GeV while the bottom plots are jet shapes for $7 < E_{T_{1,2}} < 15$ GeV. Results of HERWIG (PYTHIA) samples cannot be distinguished for $x_{1,2} > 0.8$.

### 6.3.1 The unfolding procedure

Due to the effects of smearing, efficiency and final acceptance of the detector measured distributions are in general different from the true ones. The unfolding procedure attempts to find an underlying distribution of the physical quantities on the hadron level which would be observed in the detector as a distribution consistent with the data.

From the mathematical point of view it is a deconvolution problem. A true distribution $f(x)$ is sought for which a measured distribution $g(y)$ is known. The function $g(y)$ is a sum of $f(x)$ convoluted with a detector response function $A(x)$ and additional background $b(y)$.

$$g(y) = \int_x A(x)f(x) + b(y) \tag{6.4}$$

In the following the discussion of possible solutions of the deconvolution will be restricted to a discrete case

$$y_i = \sum A_{ij}x_j + b_i \tag{6.5}$$

Several methods were developed to cope with this problem.

- A naive approach is to find a solution by vector algebra. If the binning is equal for x and y one can try to evaluate

  $$x = A^{-1}(y - b) \tag{6.6}$$

  This approach yields rarely good results for two reasons. As the matrix elements are subject to statistical fluctuations there is no guarantee that A is a positively definite matrix. And even if the inverse of A exists one is likely to obtain a wildly oscillating solution of $x$.

- Bin-to-bin correction - applicable only if migration between bins is small and if Monte Carlo describes data well. For each bin of the distribution the ratio between its content on the hadron level and on the detector level is calculated. The measured distribution is multiplied by these factors.

- Regularised unfolding methods were developed to overcome difficulties of solving Eq. (6.6) straightforwardly. The classical tool used in many analyses of the structure functions is the RUN [40, 41] program by V. Blobel. The regularization is based on an assumption that the solution should have minimum curvature.

- Bayesian unfolding [42] is an iterative application of Bayes' theorem during which from the conditional probabilities for a given cause to produce an effect a new set of the probabilities that an effect has its origin in a particular cause is obtained. It works for multidimensional problems, the binning (and the domains of variables) may be different on the detector level and on the hadron level, it can correct for large migration between bins and last but not least the background is naturally incorporated into the procedure.

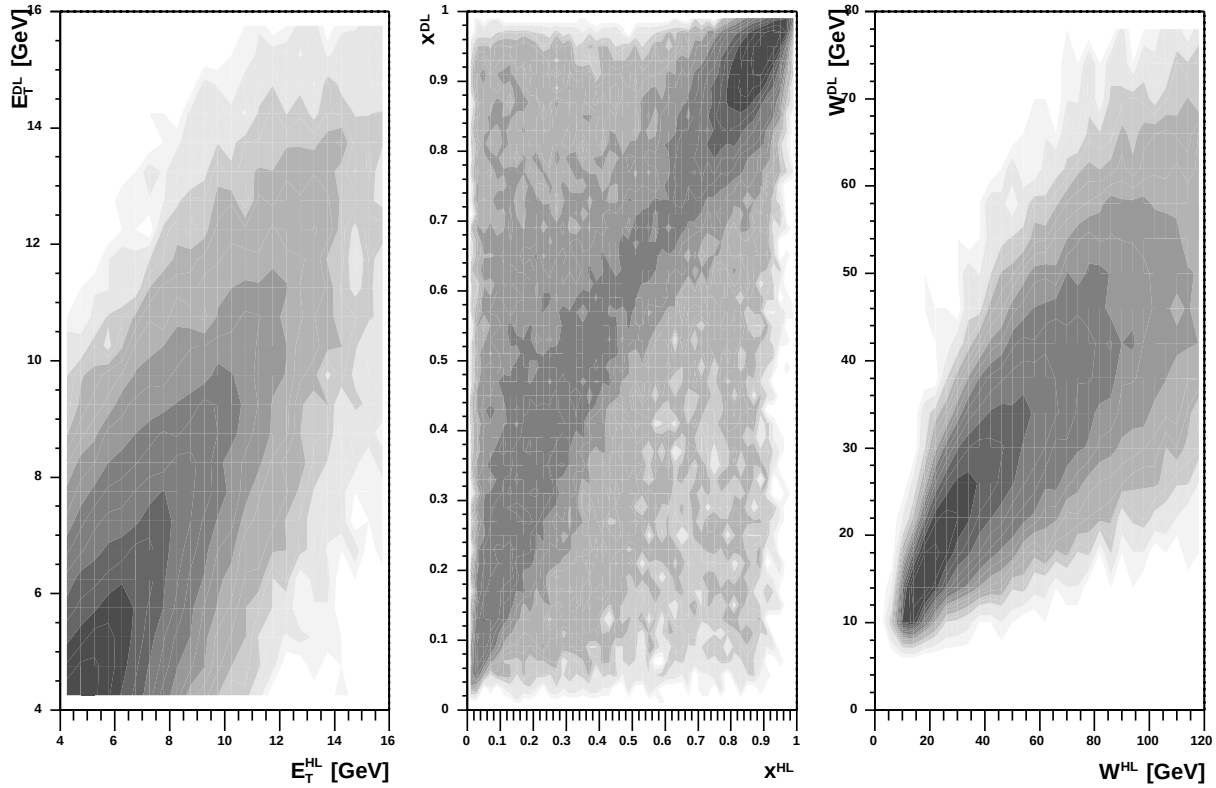


Figure 6.17: The correlations between the detector and hadron level values of the jet transverse energy $E_T$, the fraction of the photon momentum $x_1$ and the invariant mass $W$. The z axis of the plots is in logarithmic scale as the plots are nonuniformly populated.

The unfolding method based on Bayes' theorem was used as a primary tool to correct measured distributions to the hadron level. Simple bin-to-bin correction was used as a complementary method to cross check the behaviour of the unfolding program.

The reason for choosing Bayes' method is that substantial migration of events is expected. It is documented by Fig. 6.17 which shows the level of correlation between event variables on the hadron level and on the detector level. Although the variables are correlated it is evident that the migration between bins of given variables is not negligible. Another fact which is in favour of Bayesian unfolding is that background can be treated on equal footing with other causes. The largest source of background in this unfolding problem is not from another physical process. It comes from two-photon processes with two jets observed on the detector level but which did not originate from two-jet event on the hadron level or the two jets had a lower $E_T$ the threshold above which the hadron level cross sections is to be determined.

The procedure is based on the Bayes' theorem which connects the conditional probability $P(x_{true}|x_{meas})$ that a value measured in a bin of $x_{meas}$ had its origin in some interval of true value $x_{true}$ with the probability $P(x_{meas}|x_{true})$ of value $x_{true}$ to produce an effect of $x_{meas}$. In the following the true values of the variable are referred to as causes and their measured counterparts as effects.

The conditional probability $P(C_i|E_j)$ that the observed effect $E_j$ comes from the cause $C_i$ is calculated as

$$P(C_i|E_j) = \frac{P(E_j|C_i)P(C_i)}{\sum_{l=1}^{n_C} P(E_j|C_l)P(C_l)} \tag{6.7}$$

The probability $P(E_j|C_i)$ expresses our knowledge about distortions which is the measured quantity subject to. It is obtained from the Monte Carlo simulation, often the unfolding is repeated with several simulations and the differences between results are used to estimate the systematic error of the unfolding. The sum runs over all causes from 1 to $n_C$. Number of causes typically corresponds to the number of bins in the histogram of the distribution on the hadron level, however additional causes can be allocated for background.

The distribution of the initial probability of the causes $P(C_i)$ is chosen according to the physical model of the process or can be taken as a uniform distribution if no a-priori information is known. The influence of the choice of the initial probability has to be studied and accounted for in the estimation of the systematic error of the unfolding.

The number of events $n(C_i)$ in the i-th bin of the distribution on the hadron level is given by

$$n(C_i) = \sum_{j=1}^{n_E} n(E_j)P(C_i|E_j) \tag{6.8}$$

as a sum of number of events in the j-th bin on the detector level multiplied by the conditional probability $P(C_i|E_j)$ that the observed effect $E_j$ comes from the cause $C_i$. The number of effects is denoted by $n_E$.

The procedure is iterative

1. The smearing matrix of $P(E_j|C_i)$ is calculated and the initial probabilities $P_0(C_i)$ are chosen.

2. Formula (6.7) is used to calculate $P(C_i|E_j)$ and subsequently Formula (6.8) gives $n(C_i)$.

   - if $n(C_i)$ differs from the previous estimation by less than $\Delta\chi^2$ the unfolding has converged.
   - otherwise $n(C_i)$ is used to update $P(C_i)$ and the algorithm repeats the step 2.

The evaluation of the errors is discussed in Appendix B.1.

The unfolding was applied in the following manner. The number of effects was greater than the number of causes ($n_C = 18$ and $n_E = 50$). One additional cause was allocated for generalised background events. These are events from the two-photon interactions which are

| $E_T^{DL}$[GeV] | MC sample | HL-DL+ | HL+DL- | HL+DL+ |
|---|---|---|---|---|
| 4 | PYTHIA SaS 1D | 37 | 29 | 34 |
| | PYTHIA SaS 2D | 44 | 25 | 30 |
| | HERWIG SUE=0.2 | 29 | 33 | 38 |
| 5 | PYTHIA SaS 1D | 15 | 53 | 32 |
| | PYTHIA SaS 2D | 17 | 53 | 30 |
| | HERWIG SUE=0.2 | 11 | 60 | 29 |
| 6 | PYTHIA SaS 1D | 7 | 71 | 22 |
| | PYTHIA SaS 2D | 8 | 72 | 20 |
| | HERWIG SUE=0.2 | 5 | 77 | 18 |

Table 6.1: Choice of the $E_T^{DL}$ cut for $E_T^{HL} = 5$ GeV. For variable $E_T^{DL}$ cut the percentage of events in different event classes is given. The symbol HL+ (DL+) denotes that there are two or more jets with $E_T$ bigger than the cut found on the hadron (detector) level. Events without two reconstructed jets above the $E_T$ cut are denoted by HL- (DL-).

seen as dijet event in the kinematical range of signal events on the detector level but which are outside the kinematical range on the hadron level or which have less than two jets on the hadron level. The kinematical ranges were chosen

$$5 \text{ GeV} < E_{T_{1,2}}^{HL} < 16 \text{ GeV}, \quad |\eta_{1,2}^{HL}| < 1.8, \quad 0 \leq x_{1,2}^{HL} \leq 1 \quad \text{for the hadron level}$$

$$5 \text{ GeV} < E_{T_{1,2}}^{DL} < 16 \text{ GeV}, \quad |\eta_{1,2}^{DL}| < 2, \quad 0 \leq x_{1,2}^{DL} \leq 1 \quad \text{for the detector level}$$

The range of $E_T$ on the detector level was chosen to be optimal from the point of view of minimum systematic errors of the unfolding. This is illustrated by Table 6.1 which collects fractions of events in three categories denoted by HL-DL+,HL+DL- and HL+DL+. HL+DL+ stands for events which are considered signal events both on the hadron level and on the detector level, i.e. there are two jets in the kinematical range of $\eta$ and above the $E_T^{HL}$ ($E_T^{DL}$) on the hadron level (on the detector level). HL-DL+ are events which have two jets above $E_T^{DL}$ on the detector level but there are less than two jets above $E_T^{HL}$ on the hadron level. Analogously HL+DL- stands for events with two jets on the hadron level and no dijet signal on the detector level. For each Monte Carlo sample the percentage of events falling into these categories is given for three values of $E_T^{DL}$. For $E_T^{DL} = 4$ GeV there is a sizeable difference in the fractions of events which would be reflected in different normalisation of unfolded distributions. The unfolding with $E_T$ cuts $E_T^{DL} > 4$ GeV and $E_T^{HL} > 5$ GeV was carried out for testing purposes and is shown for illustration in Fig. B.6.

The probabilities $P_0(C_i)$ were initialised from the true distribution of given variable in the Monte Carlo sample. The actual code used for data unfolding is available as a general purpose C++ library. It can be downloaded from [44].

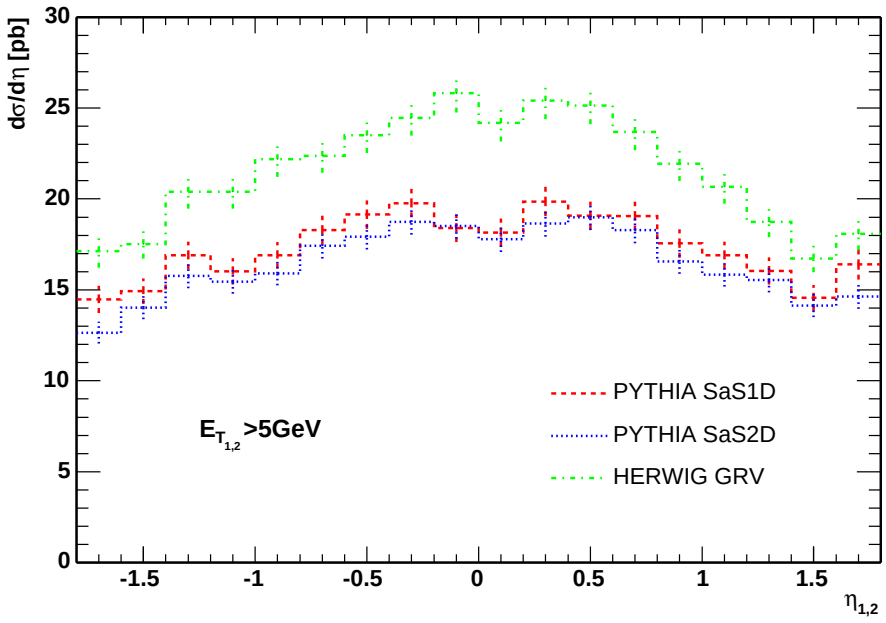


Figure 6.18: The unfolded distributions of $d\sigma/d\eta$. The statistical errors as discussed in Appendix B.1 are shown.

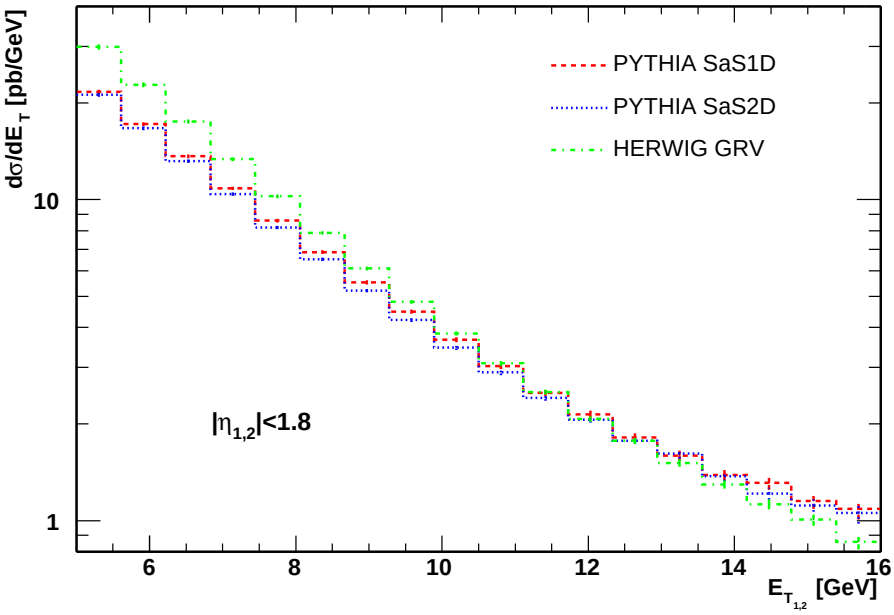


Figure 6.19: The same as Fig. 6.18 but for $d\sigma/dE_T$.

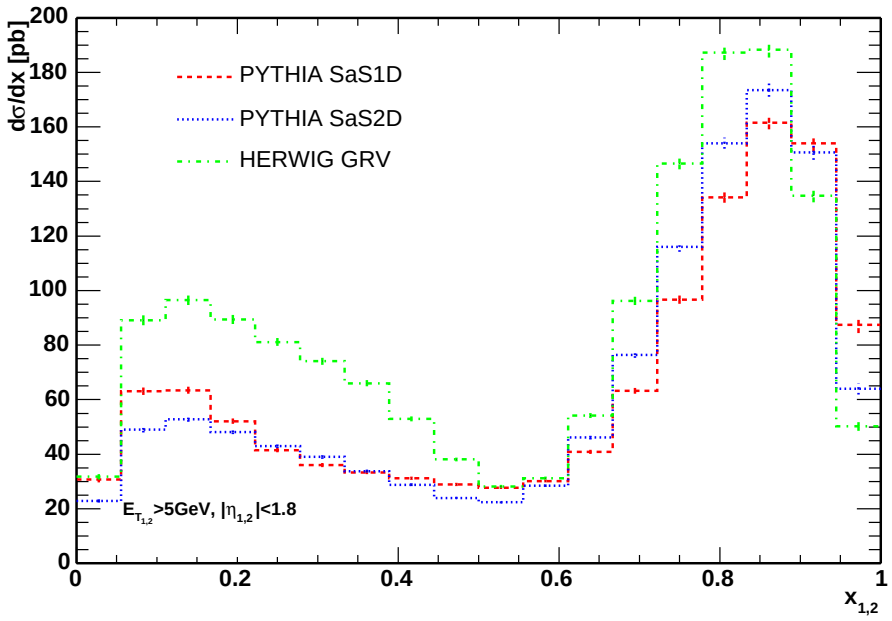


Figure 6.20: The same as Fig. 6.18 but for $d\sigma/dx$.

The unfolded distributions obtained using the three Monte Carlo samples are shown in Fig. 6.18-6.20. The statistical errors of the unfolding were calculated according to Appendix B.1. Control plots related to the unfolding procedure are given in B.2.

# Chapter 7

# Results

The inclusive dijet cross sections in the region $E_{T_{1,2}} > 5$ GeV and $|\eta_{1,2}| < 1.8$ are presented in Fig. 7.1 - Fig. 7.3 and Tables A.1- A.3. The cross sections are fully corrected to the hadron level using the Bayesian unfolding method. The results are averages of the unfolded distributions obtained with PYTHIA SaS 1D and HERWIG GRV. The statistical and systematic errors are shown separately in the plots.

- The statistical errors, shown as error bars, come from those of measured distributions and from the limited statistics of the Monte Carlo samples used for the correction. Correlations between bins are taken into account. The calculation of statistical errors is addressed in Appendix B.1.

- The largest contribution to the systematic errors comes from the difference between Monte Carlo samples used for the unfolding. As the systematic error half of the difference between the results unfolded with PYTHIA SaS 1D and HERWIG GRV was taken. The shadow area in the plots represents statistical and systematic errors added in quadrature. This determination of the systematic errors is perhaps conservative because PYTHIA SaS 1D describes the data better than HERWIG GRV.

  The background from other physical processes discussed in section 6.1 is small with respect to the systematic errors originating from unfolding with different Monte Carlo samples and is therefore neglected.

The measured differential cross sections are confronted with normalised predictions of LO QCD Monte Carlo event generators. The comparison with NLO QCD parton level calculations [45] is left for future work. The following differential cross sections were measured:

- $d\sigma^{2j}/d\eta_{1,2}$

  The result is well described by all three Monte Carlo samples. The statistical errors are less than 10% over all $\eta$ region, the systematic error is largest around $\eta = 0$ where it accounts for 18%.

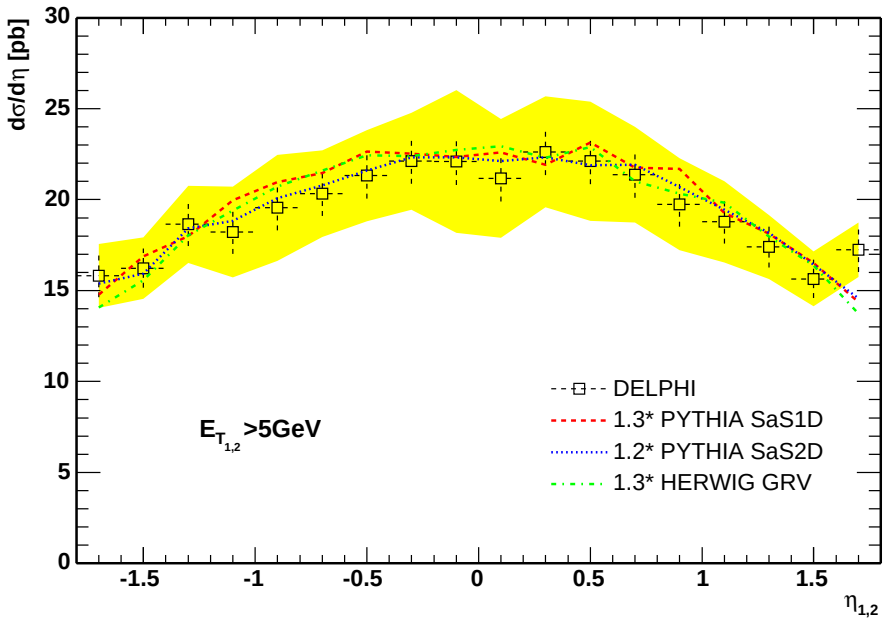


Figure 7.1: The corrected differential cross section $d\sigma/d\eta$ for dijet production. The error bars correspond to the statistical errors. The systematic errors combined with statistical errors are denoted by the shadow area. The result is presented together with the normalised curves of Monte Carlo event generators.

- $d\sigma^{2j}/dE_{T_{1,2}}$

  The distribution is well reproduced by PYTHIA SaS 1D. Both PYTHIA SaS 2D and HERWIG GRV predictions drop faster with increasing $E_T$ than the data. Statistical errors are less than 10% and the maximum systematic error is 16% in the lowest $E_T$ bin.

- $d\sigma^{2j}/dx_{1,2}$

  In contrast with all other observation PYTHIA SaS 1D gives the worst description of data, PYTHIA SaS 2D and HERWIG GRV reproduce the shape of $d\sigma^{2j}/dx_{1,2}$ better for small and large $x$, but neither Monte Carlo sample gives satisfactory description of the data in the whole region $0 < x < 1$. While the statistical errors are below 5%, the systematic errors are large, in particular around $x = 0.3$ where it accounts for 35%.

We observe that the corrected distributions of $d\sigma^{2j}/d\eta_{1,2}$, $d\sigma^{2j}/dE_{T_{1,2}}$ and $d\sigma^{2j}/dx_{1,2}$ have different shapes than their counterparts on the detector level shown in Fig. 6.11-6.13 and that the agreement between the data and Monte Carlo is worse on the hadron level than on the detector level. This comes from the fact that during the unfolding the distributions are corrected also for the events unseen in the detector which makes the comparison on the

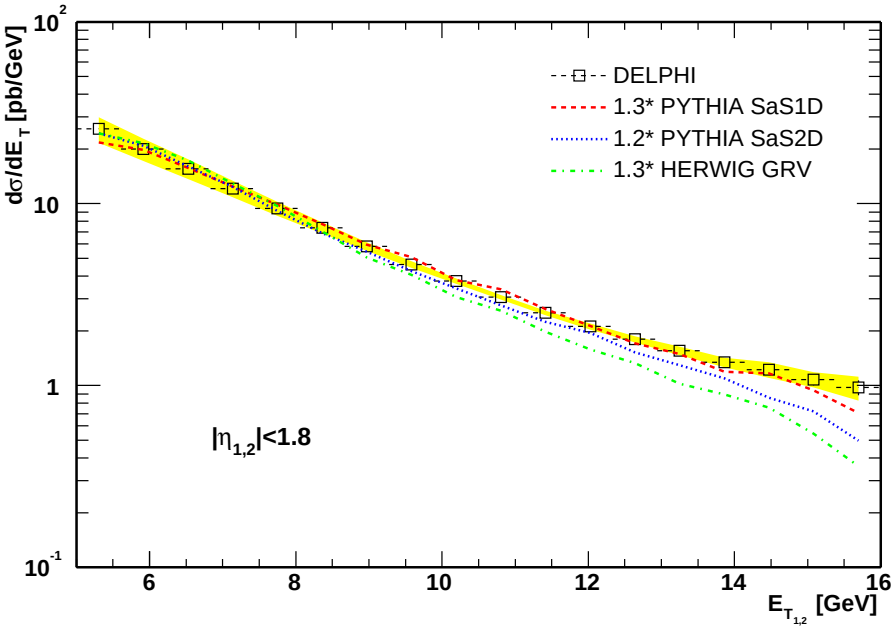


Figure 7.2: The same as Fig. 7.1 but for $d\sigma/dE_T$. Statistical errors are smaller than the symbol size.

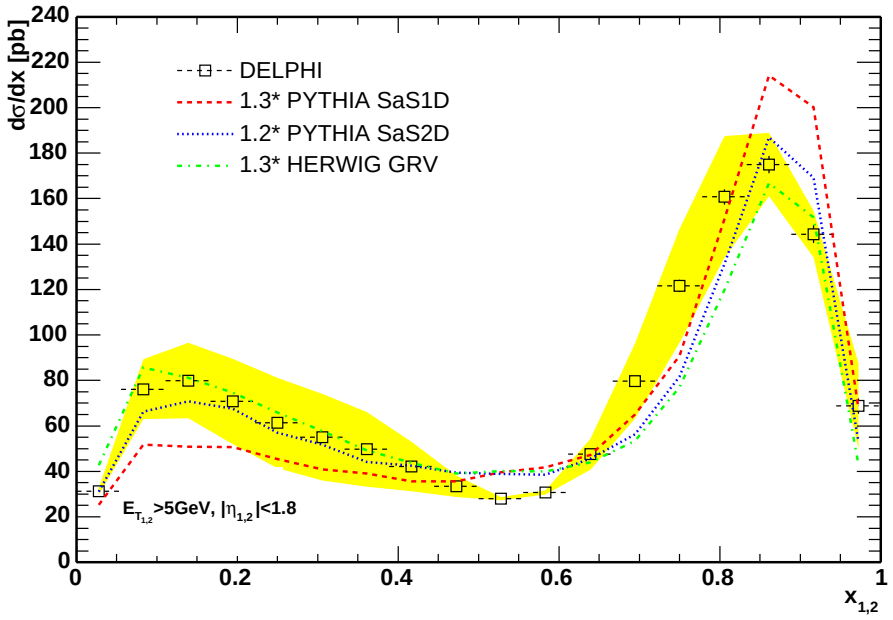


Figure 7.3: The same as Fig. 7.1 but for $d\sigma/dx$. Statistical errors are shown where larger than the symbol size.

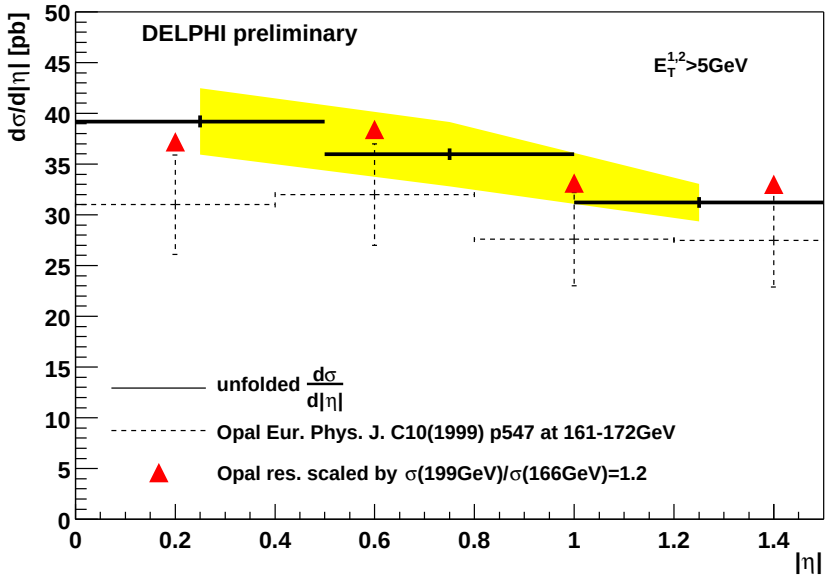


Figure 7.4: Differential cross-section $d\sigma^{2j}/d|\eta|$ for dijets $E_T > 5$GeV. DELPHI measurement with statistical errors is in shadowed area spanning between the results of unfolding obtained with PYTHIA SaS 1D and HERWIG GRV. Dashed crosses are OPAL result at $\sqrt{s_{ee}} = 161-172$ GeV (statistical and systematic errors combined). An extrapolation of OPAL result to higher energy is based on HERWIG simulation. It is shown as triangles without error bars, its relative error is the same as for the OPAL result.

hadron level more demanding. Even the best of the three Monte Carlo samples PYTHIA SaS 1D which has very good agreement with data on the detector level, fails to reproduce the hadron-level distribution of $x_{1,2}$.

Comparison of these results with other experiments can not be done straightforwardly as the measurements were carried out in different kinematical regions and also the choice of other variables and other details of the presentation of results differs. The distribution of $d\sigma^{2j}/d\eta$ in the same region $E_{T_{1,2}} > 5$ GeV has been measured by OPAL [23]. We compared our preliminary measurement with this result in [1] and the corresponding plot is shown in Fig. 7.4. The results were found to be in agreement, however it must be noted that the comparison relies on the rescaling factor $\sigma^{2j}(198\text{ GeV})/\sigma^{2j}(166\text{ GeV})$ obtained from HERWIG Monte Carlo. Our present result is not shown in the plot, it is slightly higher (the maximum difference is 10% at $|\eta| = 0.3$) than the preliminary result due to refined run-quality requirements.

The corrected jet profiles are shown in Fig. 7.5. In this case the jet profiles were corrected using bin-to-bin correction factors obtained from PYTHIA SaS 1D, and HERWIG GRV, one half of the difference between the two results was used to establish systematic error. The

experimental errors coming from the track measurement errors are shown as error bars. The shadow area represents experimental and systematic errors added in quadrature.

The comparison of the corrected jet profiles with Monte Carlo shows good agreement between data and HERWIG GRV for both double-resolved and direct events. PYTHIA SaS 1D describes well the domain of direct events. PYTHIA SaS 1Djet profiles tend to be lower than the data for jets predominantly of double-resolved interactions, this leads to a discrepancy between data and PYTHIA SaS 1D in $\Delta\phi$ which might deserve further investigation.

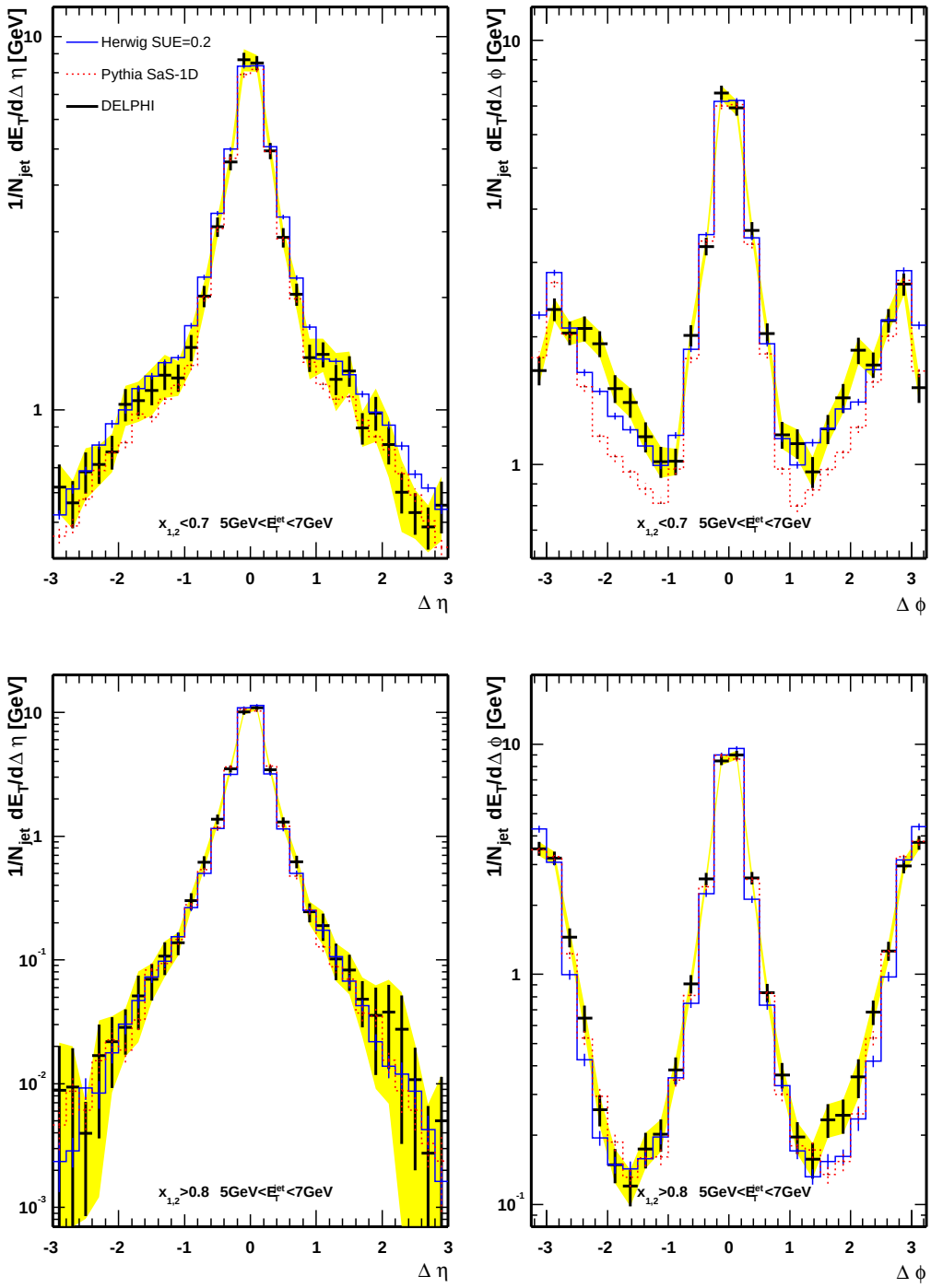


Figure 7.5: Jet profiles in $\Delta\eta$ and $\Delta\phi$ corrected to the hadron level. The shadow band represents combined experimental and systematic errors. Predictions of PYTHIA SaS 1D and HERWIG GRV are shown as histograms. The same selection of $|\eta| < 1$ and $5 < E_T < 7$ was used both for detector and hadron level jets. Upper plots are jet profiles for events with $x_{1,2} < 0.7$ (dominated by double-resolved interactions) and bottom plots are for $x_{1,2} > 0.8$ (dominated by direct photon interactions).

# Chapter 8

# Conclusion

In this thesis the first analysis of the large-$E_T$ dijet production in two photon collisions obtained with the DELPHI detector at LEP2 is presented. The inclusive differential cross sections $d\sigma^{2j}/d\eta$, $d\sigma^{2j}/dE_T$ and $d\sigma^{2j}/dx$ were measured in the kinematic range $E_T \geq 5$ GeV, $|\eta| \leq 1.8$ and the results compared with LO Monte Carlo event generators PYTHIA (using SaS 1D and SaS 2D as parameterisation of the photon PDF) and HERWIG (using GRV-G LO).

The data were fully corrected to the hadron level using the Bayesian unfolding method. The errors are dominated by the systematic error resulting from the dependence of this unfolding procedure on the Monte Carlo used.

The data are somewhat above their predictions in magnitude, which is not surprising for LO Monte Carlo event generators, but also the shapes of the distributions are not reproduced quite satisfactorily. Overall the best description of the data is obtained with PYTHIA Monte Carlo using the SAS 1D PDF of the photon, but even it fails to describe one of the basic distributions, namely that of momentum fraction $x_{1,2}$.

An important part of the analysis concerns the comparison of measured transverse energy activity with Monte Carlo results. Jet profiles as well as the transverse energy flow outside the jets were employed in order to tune in both Monte Carlo generators the parameters governing the soft collision accompanying the hard parton scattering. Good description of these quantities is important because the soft particles provide pedestals under the jets and thus influence their properties. Whereas the default setting of $p_T^{mi}$ in PYTHIA leads to very good agreement with data, the analogous parameter SUE in HERWIG required some tuning and the value SUE=0.2 was found optimal. For the transverse activity outside the jets the overall agreement with data is best for PYTHIA with SAS 1D. Interestingly, but perhaps not surprisingly, PYTHIA with SAS 1D describes very well also the energy flow inside the jets as quantified by the jet shapes.

The differences in the kinematic regions as well as experimental procedures employed in the extraction of measured cross sections prevent a direct comparison with the results of OPAL experiment. Nevertheless, we have made a rough estimate of these differences and

have found our results consistent with those in [23].

# Appendix A

# Tables

| $\eta_{1,2}$ | $d\sigma^{2j}/d\eta_{1,2}$ [pb] | stat. [pb] | syst. [pb] |
|---|---|---|---|
| -1.7 | 15.8 | ±1.2 | ±1.3 |
| -1.5 | 16.2 | ±1.1 | ±1.3 |
| -1.3 | 18.6 | ±1.2 | ±1.7 |
| -1.1 | 18.2 | ±1.2 | ±2.2 |
| -0.9 | 19.5 | ±1.2 | ±2.6 |
| -0.7 | 20.3 | ±1.2 | ±2.0 |
| -0.5 | 21.3 | ±1.2 | ±2.2 |
| -0.3 | 22.1 | ±1.3 | ±2.4 |
| -0.1 | 22.1 | ±1.3 | ±3.7 |
| 0.1 | 21.2 | ±1.3 | ±3.0 |
| 0.3 | 22.6 | ±1.3 | ±2.8 |
| 0.5 | 22.1 | ±1.3 | ±3.0 |
| 0.7 | 21.4 | ±1.3 | ±2.3 |
| 0.9 | 19.7 | ±1.2 | ±2.2 |
| 1.1 | 18.8 | ±1.2 | ±1.9 |
| 1.3 | 17.4 | ±1.1 | ±1.4 |
| 1.5 | 15.6 | ±1.0 | ±1.1 |
| 1.7 | 17.2 | ±1.2 | ±0.8 |

Table A.1: The differential cross section $d\sigma^{2j}/d\eta_{1,2}$

| $E_{T_{1,2}}$ [GeV] | $d\sigma^{2j}/dE_{T_{1,2}}$ [pb/GeV] | stat. [pb/GeV] | syst. [pb/GeV] |
|---|---|---|---|
| 5.31 | 25.7 | ±0.6 | ±4.1 |
| 5.92 | 20.0 | ±0.4 | ±2.8 |
| 6.53 | 15.6 | ±0.3 | ±1.9 |
| 7.14 | 12.1 | ±0.2 | ±1.3 |
| 7.75 | 9.42 | ±0.17 | ±0.8 |
| 8.36 | 7.37 | ±0.14 | ±0.51 |
| 8.97 | 5.81 | ±0.11 | ±0.29 |
| 9.58 | 4.64 | ±0.10 | ±0.16 |
| 10.19 | 3.75 | ±0.09 | ±0.08 |
| 10.81 | 3.06 | ±0.08 | ±0.03 |
| 11.42 | 2.51 | ±0.07 | ±0.01 |
| 12.03 | 2.11 | ±0.07 | ±0.04 |
| 12.64 | 1.80 | ±0.07 | ±0.02 |
| 13.25 | 1.55 | ±0.07 | ±0.04 |
| 13.86 | 1.34 | ±0.07 | ±0.05 |
| 14.47 | 1.22 | ±0.08 | ±0.09 |
| 15.08 | 1.08 | ±0.08 | ±0.07 |
| 15.69 | 0.97 | ±0.09 | ±0.11 |

Table A.2: The differential cross section $d\sigma^{2j}/dE_{T_{1,2}}$

| $x_{1,2}$ [GeV] | $d\sigma^{2j}/d_{1,2}$ [pb] | stat. [pb] | syst. [pb] |
|---|---|---|---|
| 0.027 | 31.2 | ±1.4 | ±0.55 |
| 0.083 | 76.1 | ±2.2 | ±13 |
| 0.138 | 80.0 | ±2.2 | ±17 |
| 0.194 | 70.8 | ±1.9 | ±19 |
| 0.25 | 61.3 | ±1.6 | ±20 |
| 0.305 | 55.1 | ±1.5 | ±19 |
| 0.361 | 49.7 | ±1.3 | ±16 |
| 0.416 | 42.1 | ±1.1 | ±11 |
| 0.472 | 33.5 | ±0.88 | ±4.6 |
| 0.527 | 28.0 | ±0.73 | ±0.25 |
| 0.583 | 30.7 | ±0.78 | ±0.53 |
| 0.638 | 47.5 | ±1.2 | ±6.7 |
| 0.694 | 79.7 | ±1.8 | ±16 |
| 0.75 | 122 | ±2.6 | ±25 |
| 0.805 | 161 | ±3.4 | ±27 |
| 0.861 | 175 | ±3.8 | ±13 |
| 0.916 | 144 | ±3.8 | ±9.6 |
| 0.972 | 68.7 | ±3.3 | ±19 |

Table A.3: The differential cross section $d\sigma/dx_{1,2}$

# Appendix B

# The unfolding procedure

## B.1 Evaluation of the errors

The statistical errors which are presented on the unfolded results were evaluated according to the following approach.

The number of the expected causes in the bin i is expressed

$$n(C_i) = \sum_{j=1}^{n_E} M_{ij} n(E_j) \tag{B.1}$$

The statistical errors come from two sources. First there are the statistical errors of the measured numbers $n(E_j)$ and then the errors coming from the evaluation of the unfolding matrix $M_{ij}$.

$$M_{ij} = \frac{P(E_j|C_i)P(C_i)}{[\sum_{l=1}^{n_E} P(E_l|C_i)]\,[\sum_{l=1}^{n_C} P(E_j|C_l)P(C_l)]} \tag{B.2}$$

$n(E_j)$ is a multinomial distribution where the parameter $n$ is the estimated number of true events $N_{true}$. The unfolding matrix has its uncertainities in the distribution of the initial probabilities. This error is included in the systematic error. Then $P(E_j|C_i)$ have statistical errors as they are determined from the Monte Carlo with limited number of events. The systematic errors of $P(E_j|C_i)$ are estimated by unfolding with several Monte Carlo models. Correlations between $n_(C_i)$ are expected as their values are determined by several $n(E_j)$ and $P(E_j|C_i)$. The covariance matrix $V$ which takes into account both $n(E_j)$ and $M_{ij}$ is

$$V_{kl} = V_{kl}(n(E)) + V_{kl}(M) \tag{B.3}$$

The first term $V_{kl}(n(E))$ can be written

$$V_{kl}(n(E)) = \sum_{j=1}^{n_E} M_{kj} M_{lj} n(E_j) \left(1 - \frac{n(E_j)}{N_{true}}\right) - \sum_{i,j=1, i\neq j}^{n_E} M_{ki} M_{lj} \frac{n(E_i)n(E_j)}{N_{true}} \tag{B.4}$$

while the following holds for $V_{kl}(M)$

$$V_{kl}(M) = \sum_{i,j=1}^{n_E} n(E_i)n(E_j)Cov(M_{ki}, M_{lj}) \tag{B.5}$$

where

$$\begin{aligned}
Cov(M_{ki}, M_{lj}) &= \sum_{ru,su} \frac{\delta M_{ki}}{\delta P(E_r|C_u)} \frac{\delta M_{lj}}{\delta P(E_s|C_u)} \\
&\times \; Cov\left[P(E_r|C_u), P(E_s|C_u)\right] && \text{(B.6a)} \\
\frac{\delta M_{ki}}{\delta P(E_r|C_u)} &= M_{ki}\left[\frac{\delta_{ku}\delta_{ri}}{P(E_r|C_u)} - \frac{\delta_{ku}}{\epsilon_u} - \frac{\delta_{ri}M_{ui}\epsilon u}{P(E_i|C_u)}\right] && \text{(B.6b)} \\
Cov\left[P(E_r|C_u), P(E_s|C_u)\right] &= \\
&= \frac{1}{n_u}P(E_r|C_u)\left[1 - P(E_r|C_u)\right] \qquad (r = s) \\
&= -\frac{1}{n_u}P(E_r|C_u)P(E_s|C_u) \qquad (r \neq s) && \text{(B.6c)}
\end{aligned}$$

where $n_u$ is the number of events generated in the cell $C_u$ for evaluation of the smearing function.

## B.2 Tests of the unfolding problem

In this section we present several plots to show that the unfolding procedure is stable and its results are understood. The unfolding was investigated from a number of views:

1. All the unfolded distributions were convoluted with the smearing matrix and the folded distributions agreed with the measured ones.

2. Mutual unfolding of one Monte Carlo sample with another was carried out. The unfolding of the detector level distribution of PYTHIA SaS 1D with PYTHIA SaS 2D and HERWIG GRV is given in Fig. B.1-B.3. The results agree with the true distributions of $\eta$, $E_T$ and $x$.

3. The unfolding with Bayes' approach was cross-checked with bin-to-bin corrections (Fig. B.4). The normalization of results is close for both methods. Bin-to-bin corrections exhibit less smooth results than the unfolding.

4. The influence of the binning is studied in Fig. B.5. The unfolding with larger bins is consistent with the present results.

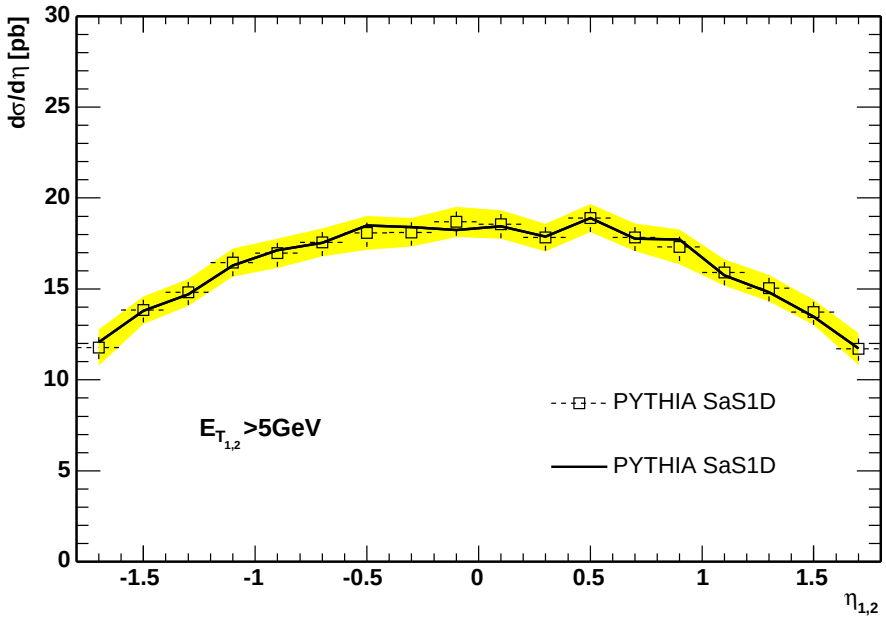


Figure B.1: $d\sigma^{2j}/d\eta$ of PYTHIA SaS 1D unfolded with PYTHIA SaS 2D and HERWIG GRV. The statistical errors are shown as error bars, the shadow area is the combination of statistical errors and of the systematic errors as described in Chapter 7.

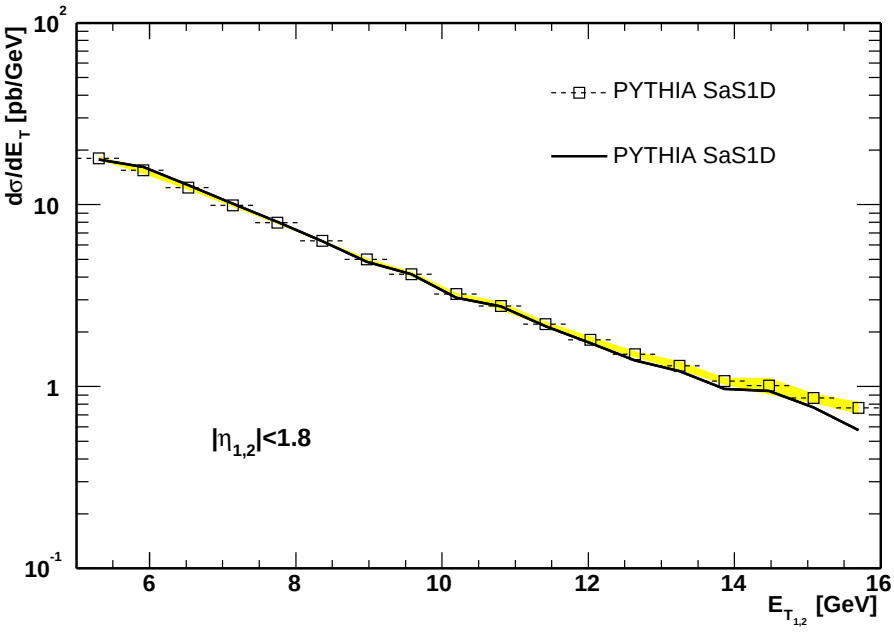


Figure B.2: The same as Fig. B.1 but for $d\sigma^{2j}/dE_T$.

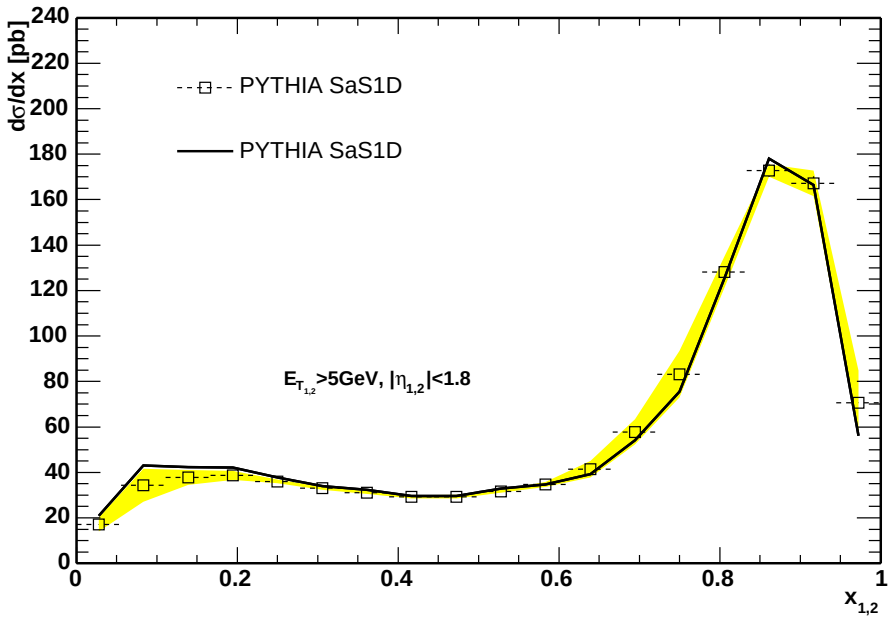


Figure B.3: The same as Fig. B.1 but for $d\sigma^{2j}/dx$.

5. The demonstration of larger systematic effects in case of $E_T^{DL}$ cut lower than 5 GeV is in Fig. B.6. It is a complementary plot to the Table 6.1 and its discussion.

6. The convergence of the unfolding is studied in Fig. B.7. The unfolded distribution are shown after 3 steps, after 5 steps and after a convergence is reached when $\Delta\chi^2$ between two subsequent steps changes less than a certain limit $\Delta\chi^2_{lim} = n_C/100$. The procedure converges quickly, typical number of steps is below 10.

7. The one-dimensional unfolding was also compared with projections of two-dimensional unfolding in $E_T - x$ and $E_T - \eta$. The results of both approaches agree.

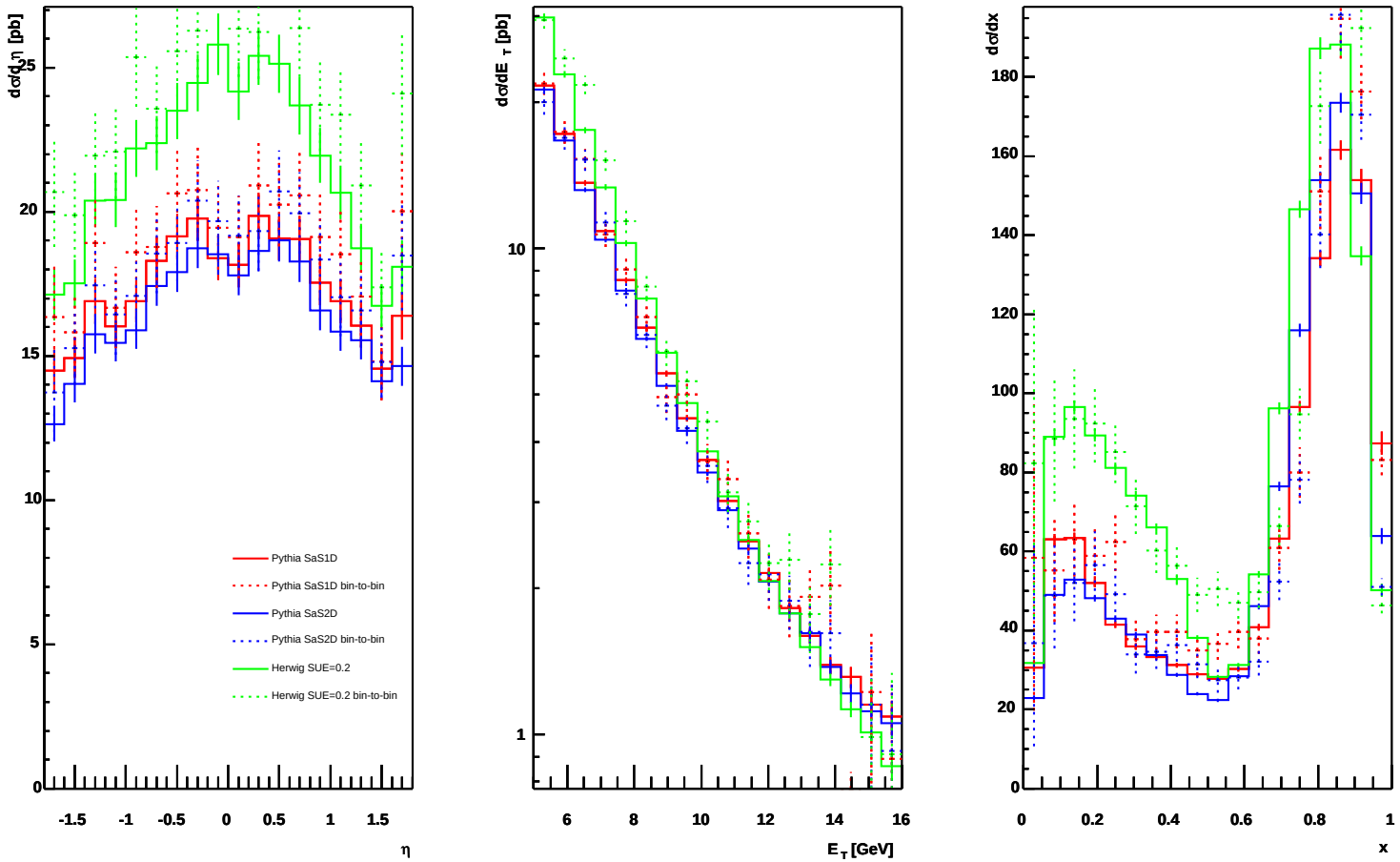


Figure B.4: Unfolded distributions of $\eta$, $E_T$ and $x$ (solid line histograms) are presented with results of bin-to-bin correction (dashed histograms). The histograms of the same colour belong to one Monte Carlo sample.

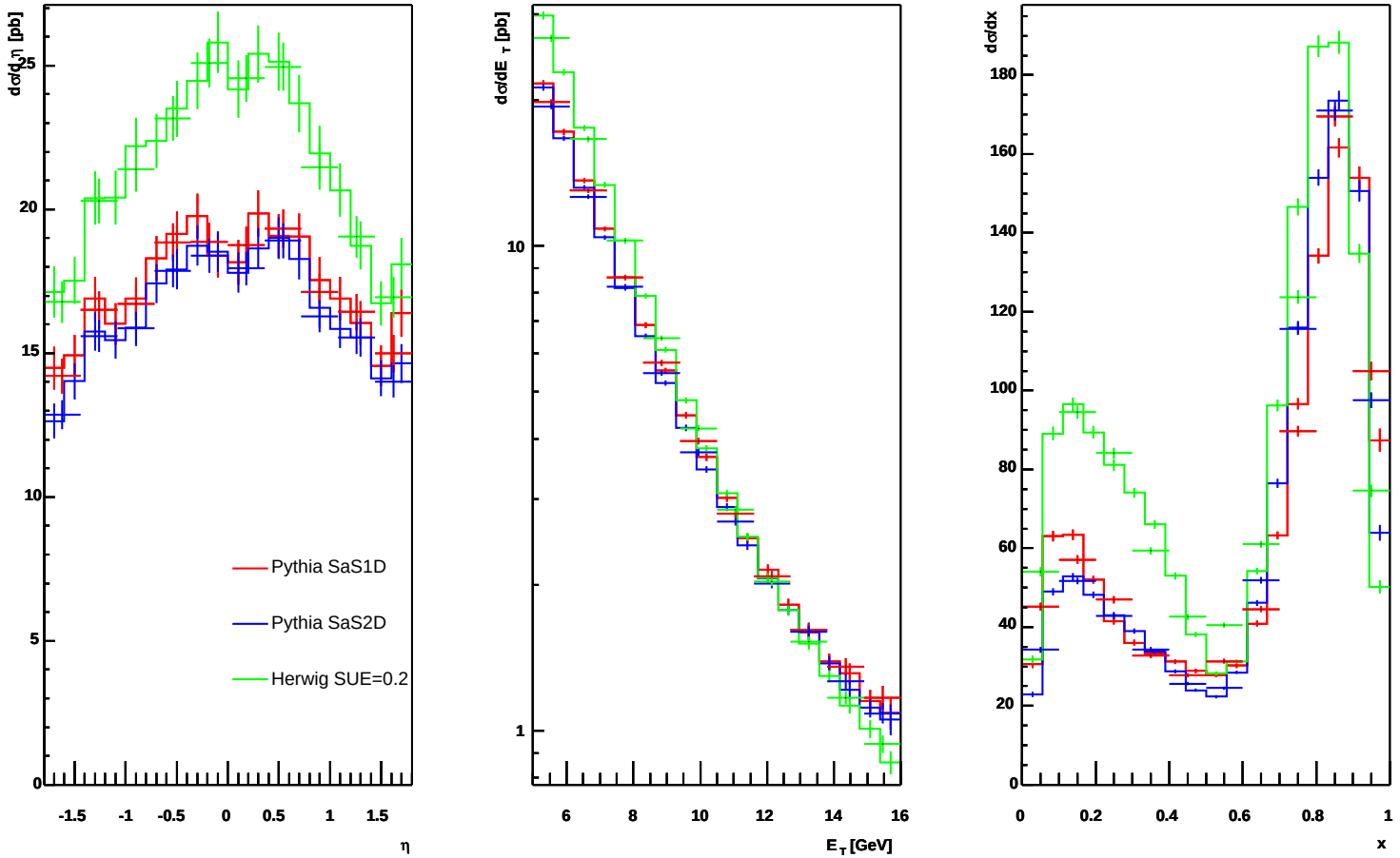


Figure B.5: Control plots for the unfolding procedure. The unfolded distributions of $\eta$, $E_T$ and $x$ (solid line histograms) are shown together with the results of the unfolding procedure carried out with the same Monte Carlo models but with larger binning (shown as crosses).

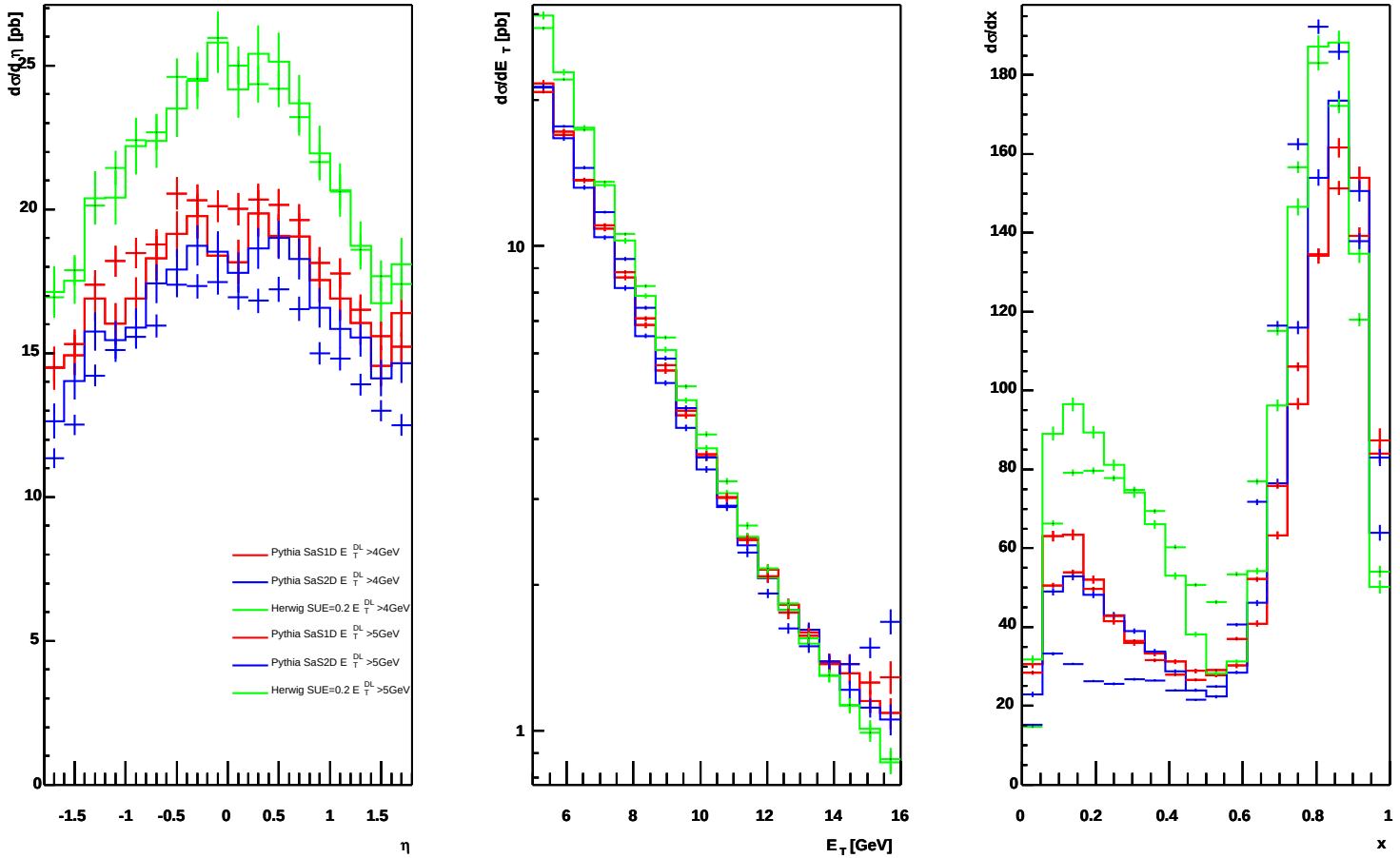


Figure B.6: The unfolding with $E_T^{DL} > 5$ GeV (histograms) is shown together with the unfolding with lower $E_T^{DL}$ cut ($E_T^{DL} > 4$ GeV, crosses).

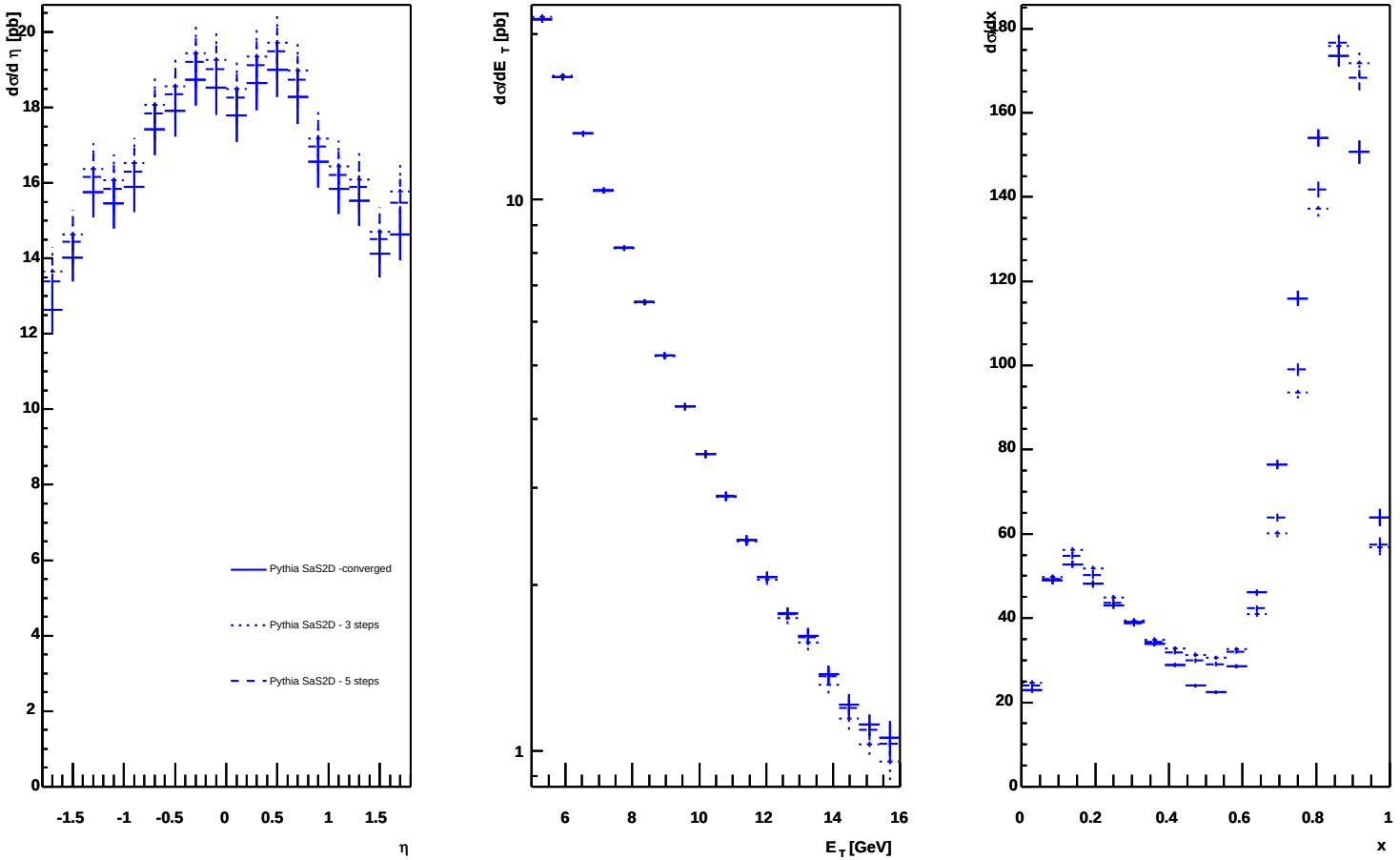


Figure B.7: Convergence of the unfolding procedure. The results of the unfolding after 3, 5 and converged

# Bibliography


[1] J. Mašík, A Measurement of the Dijet Cross Section in Two-Photon Collisions at LEP2
ISBN 981-238-053-1, *Proceedings of the International Conference on the Structure and Interactions of the Photon Including the 14th International Workshop on Photon-Photon Collisions, Photon 2001, Ascona.*

[2] P. Kessler, Sur une méthode simplifiée de calcul por les processus relativistes en électrodynamique quantique.
Il Nuovo Cimento 17 (1960) 809-828.

[3] C. F. von Weizsäcker, Ausstrahlung bei Stößen sehr schneller Elektronen.
Z. Phys. 88 (1934) 612-625.

[4] E. J. Williams, Nature of the high energy particles of penetrating radiation and status of ionization and radiation formulae.
Phys. Rev. 45 (1934) 729-730.

[5] B. L. Combridge and C. J. Maxwell,
Nucl. Phys. B239 (1984) 429.

[6] M. Glück, E. Reya, A. Vogt, Parton structure of the photon beyond the leading order.
Phys. Rev. D45, 3986.

[7] G. A. Schuler, T. Sjöstrand, Low- and high-mass components of the photon distribution functions.
Z. Phys. C 68 (1995) 607.

[8] G. A. Schuler, T. Sjöstrand, Parton distributions of the virtual photon.
Phys. Lett. 376B (1996) 193

[9] M. Glück, E. Reya, I. Schienbein, Radiatively generated distributions of real and virtual photons.
Phys. Rev. D60, 054019.

[10] The Opal Collaboration, QCD Studies using a Cone-based Jet Finding Algorithm for $e^+e^-$ Collisions at LEP,

Z.Phys.C63:197-212,1994.
Jet finding code pxcone.f provided by M. H. Seymour.

[11] M. Krawczyk, A. Zembrzuski, M. Stazsel, Survey of present data on photon structure functions and resolved photon processes.

Phys. Rep. Vol. 345, Nos. 5-6 (2001) pp. 265-452

[12] R. Nisius, The photon structure from deep inelastic electron-photon scattering.

Phys. Rep. 332 (2000) 165.

[13] PLUTO Collaboration, Ch. Berger et al., Phys. Lett.**B142** (1984) 111;
PLUTO Collaboration, Ch. Berger et al., Phys. Lett.**B142** (1984) 119;
PLUTO Collaboration, Ch. Berger et al., Phys. Lett. **B281** (1987) 365;
PLUTO Collaboration, Ch. Berger et al., Phys. Lett. **B107** (1981) 168;
JADE Collaboration, W. Bartel et al., Z. Phys. **C24** (1984) 231;
CELLO Collaboration, H.-J. Behrend et al., contributed to the XXVth Int. Con. on HEP, Singapore 1990, unpublished;
TASSO Collaboration, M. Althoff et al., Z. Phys. **C31** (1986) 527.

[14] AMY Collaboration, T. Sasaki et al., Phys. Lett. **B252** (1990) 491;
AMY Collaboration, B. J. Kim et al., Phys. Lett. **B325** (1994) 248;
TOPAZ Collaboration, H. Hayashii et al., Phys. Lett. **B314** (1993) 149.

[15] F. Cornet, P. Jankowski, M., Krawczyk, A. Lorca, A New 5-Flavour LO Analysis and Parametrization of Parton Distributions in the Real Photon.

CERN-TH/2002-362, arXiv:hep-ph/0212160.

[16] arXiv:hep-ex/0111052.

[17] TPC/2$\gamma$ Collaboration, H. Aihara et al., Phys. Rev. Lett. **58** (1987) 97;
TPC/2$\gamma$ Collaboration, H. Aihara et al., Z. Phys. **C34** (1987) 1.

[18] ALEPH Collaboration, D. Buskulic et al., Phys. Lett. **B313** (1993) 509;
ALEPH Collaboration, R. Barate et al., Phys. Lett.**B458** (1999) 152;
DELPHI Collaboration, P. Abreu et al., Phys. Lett **B342** (1995) 402;
L3 Collaboration, M. Acciarri et al., Phys.Lett. **B436** (1998) 403 ;
L3 Collaboration, M. Acciarri et al., Phys.Lett. **B438** (1998) 363 ;
L3 Collaboration, M. Acciarri et al., Phys.Lett. **B447** (1999) 147 ;
L3 Collaboration, M. Acciarri et al., Phys.Lett. **B483** (2000) 373 ;
L3 Collaboration, M. Achard et al., Phys.Lett. **B531** (2002) 39 ;

OPAL Collaboration, R. Ackers et al., Z. Phys. **C61** (1994) 199;
OPAL Collaboration, G. Abbiendi et al., Eur.Phys.J.**C10** (1999) 547;
OPAL Collaboration, G. Abbiendi et al., Eur.Phys.J.**C11** (1999) 409;
OPAL Collaboration, G. Abbiendi et al., Eur.Phys.J.**C18** (2000) 15;
OPAL Collaboration, G. Abbiendi et al., Phys. Lett.**B533** (2002) 207.

[19] BCDMS Collab., Benvenuti et al., Phys. Lett. **B223**(1989) 485.

[20] H1 Collaboration, C. Adloff et al., Z. Phys. **C74** (1997) 191.
ZEUS Collaboration, J. Breitweg et al., Z. Phys.**B74**(1997) 207.

[21] A. D. Martin, R. G. Roberts, W. J. Stirling, R. S. Thorne, Eur. Phys. J. **C23** 73-87 (2002)

[22] H1 Collaboration, T. Ahmed et al., Nucl. Phys. **B445** (1995) 195;
H1 Collaboration, S. Aid et al., Z. Phys. **C70** (1996) 17;
H1 Collaboration, C. Adloff et al., Eur. Phys. J. **C1** (1998) 97;
H1 Collaboration, C. Adloff et al., Eur. Phys. J. **C13** (2000) 397;
H1 Collaboration, C. Adloff et al., Phys. Lett. **B483** (2000) 36;
ZEUS Collaboration, M. Derrick et al., Phys. Lett. **B322** (1994) 287;
ZEUS Collaboration, M. Derrick et al., Phys. Lett. **B348** (1995) 665;
ZEUS Collaboration, M. Derrick et al., Phys. Lett **B384** (1996) 401;
ZEUS Collaboration, J. Breitweg et al., Eur. Phys. J. **C1** (1998) 109;
ZEUS Collaboration, J. Breitweg et al., Eur. Phys.J. **C23** (2002) 615.
ZEUS Collaboration, J. Breitweg et al., Phys. Lett.**B472**(2000) 175.

[23] The Opal Collaboration, Di-jet Production in Photon-Photon Collisions at $\sqrt{s_{ee}}$= 161 and 172 GeV.

CERN-EP/98-113, Eur. Phys. J. C10 (1999) 547-561.

[24] The OPAL Collaboration, Di-Jet Production in Photon-Photon collisions at $\sqrt{s_{ee}}$ from 189 to 209 GeV.

CERN-EP-2002-093, hep-ex/030113, Submitted to Eur. Phys. J.

[25] H1 Collaboration, C. Adloff et al., Phys. Lett. **B467** (1999) 156, erratum ibid. **B518** (2001) 331.
ZEUS Collaboration, J. Breitweg et al., Eur. Phys.J. **C18** (2001) 625.

[26] LEP heavy quarks OPAL Collaboration, G. Abbiendi et al., Phys. Lett.**B359** (2002)13.
OPAL Collaboration, G. Abbiendi et al., Eur. Phys.J. **C16** (2000) 579.
L3 Collaboration, M. Acciarri et al., Phys.Lett. **B503** (2001) 10.
L3 Collaboration, M. Acciarri et al., Phys.Lett. **B514** (2001) 19.
F. Kapusta, talk at Photon 2003, `http://www.lnf.infn.it/conference/photon03/`

[27] Delphi collaboration, Final results fro DELPHI on the searches for SM and MSSM Neutral Higgs bosons.

CERN-EP 2003/008

[28] P. Arnio et al. (DELPHI Collaboration), The DELPHI Detector At LEP.

Nucl. Instr. and Meth. A303 (1991) 233-276, North-Holland.

[29] Delphi Collaboration, Performance of the DELPHI Detector.

Nucl. Instr. and Meth. A378 (1996) 57. CERN-PPE/95-194.

[30] G. Marchesini, B.R. Webber, G. Abbiendi, I.G. Knowles, M.H. Seymour and L. Stanco, HERWIG 6.1.

Computer Phys. Commun. 67 (1992) 465, hep-ph/9912396.

[31] H. Plothow-Besch, PDFLIB : a library of all available parton density functions of the nucleon, the pion and the photon and the corresponding $\alpha_s$ calculations.

Comput. Phys. Commun. : 75 (1993) , pp.396-416.

[32] T. Sjöstrand, P. Edén, Ch. Friberg, L. Lönnblad, G. Miu, S. Mrenna, E. Norrbin, High-Energy-Physics Event Generation with PYTHIA 6.1.

LU-TP 00-30, hep-ph/0010017.

[33] DELSIM User's Guide, DELPHI-87-96 PROG-99, CERN, July 1989.
DELSIM Reference Manual, DELPHI 87-98 PROG-100, CERN, July 1989.

[34] DELANA User's Guide. DELPHI 89-44 PROG 137.

[35] J. Chýla, J. Cvach, Virtual photon structure from jet production.

World Scientific (1998). Photon'97 - Proceedings of the XIth International Workshop.

[36] V. Canale et al., The DELPHI Trigger System at LEP200.

DELPHI-99-7 DAS-188, CERN, February 1999.

[37] ZEUS Collaboration, J. Breitweg et al., Eur. Phys.J. **C2** (1998) 61.
H1 Collaboration, C. Adloff et al., Nucl. Phys. **B545** (1999) 3.

[38] T. Wengler, talk at Photon 2003, `http://www.lnf.infn.it/conference/photon03/`

[39] Ch. Mesropian, talk at CINANP conference, May 2003.

[40] V. Blobel, Unfolding methods in high-energy physics experiments.

DESY84-118, 1984.

[41] V. Blobel, The RUN manual. Regularized Unfolding for High-Energy Physics Experiments.

Opal note 361, 1996.

[42] G. D'Agostini, A multidimensional unfolding method based on Bayes' Theorem.

Nucl. Instr. and Meth. in Phys. Res. A362 (1995) 487

[43] bayes.f `http://zeus.roma1.infn.it/~agostini/prob+stat.html`

[44] UnfBayesAlg `http://darbujan.fzu.cz/~masik/unfolding/`

[45] M. Klasen, T. Kleinwort, G. Kramer, Inclusive Jet Production in $\gamma p$ and $\gamma\gamma$ Processes: Direct and Resolved Photon Cross-Sections in Next-To-Leading Order QCD.

Eur.Phys.J.direct C1:1,1998 hep-ph/9712256